ORNL/HTSPC-13

# ORNL Superconducting Technology Program for Electric Power Systems

# Annual Report for FY 2001

**February 2002**

SUPERCONDUCTIVITY FOR ELECTRIC SYSTEMS

**ORNL/HTSPC-13**

# ORNL SUPERCONDUCTING TECHNOLOGY PROGRAM FOR ELECTRIC POWER SYSTEMS

## ANNUAL REPORT FOR FY 2001

Compiled by
R. A. Hawsey
A. W. Murphy

Edited by
W. S. Koncinski

Manuscript Completed: December 2001
Date Published: February 2002

Prepared for the
Office of Power Technologies
Office of Energy Efficiency and Renewable Energy
U.S. DEPARTMENT OF ENERGY
(EB 50 01 00 0)

Prepared by
OAK RIDGE NATIONAL LABORATORY
P.O. Box 2008
Oak Ridge, TN 37831-6285
Managed by
UT-Battelle, LLC
for the
U.S. DEPARTMENT OF ENERGY
under contract DE-AC05-00OR22725

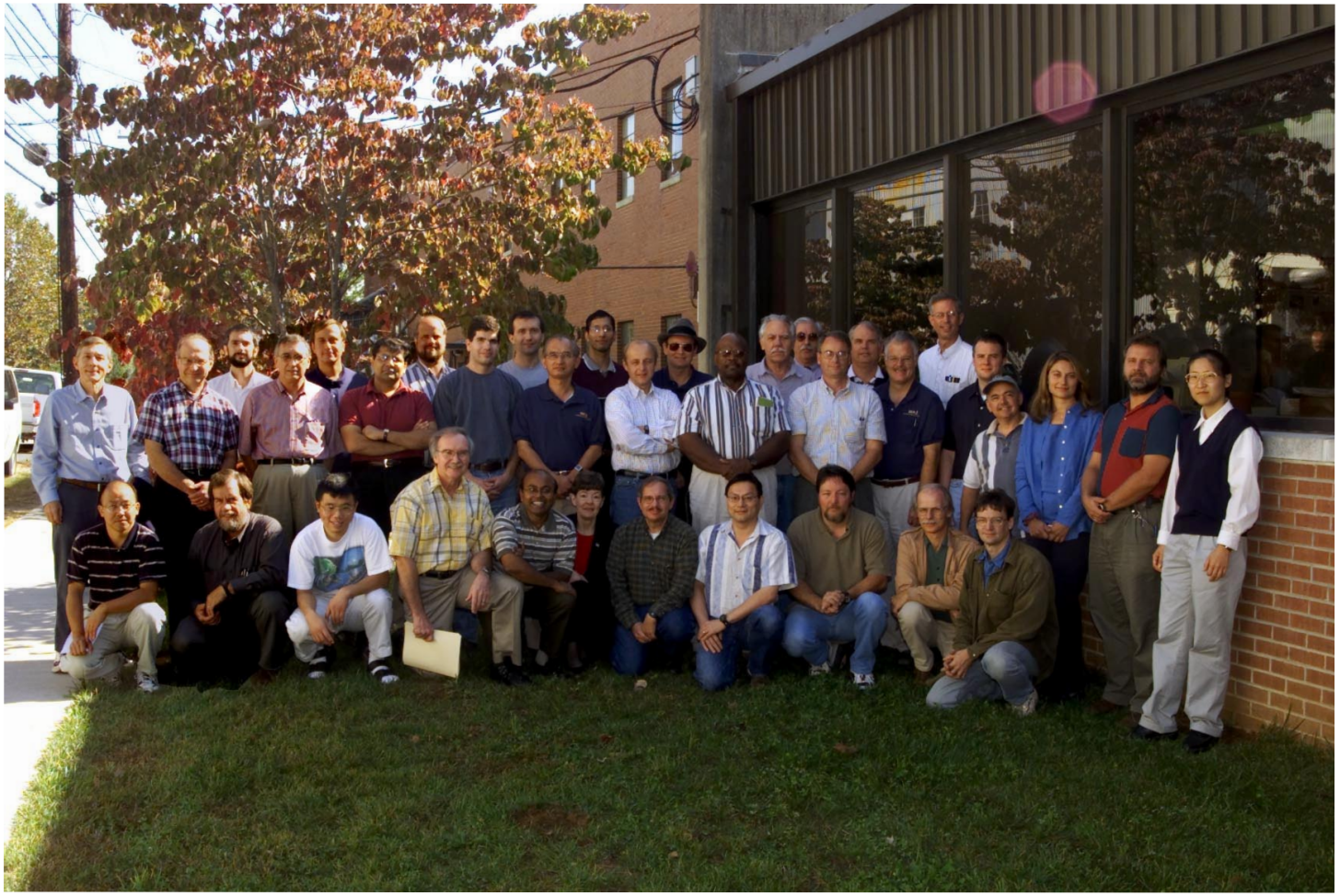

Front row: (left to right) Yifei Zhang, Lee Heatherly, Hong-Ying Zhai, David K. Christen, M. Parans Paranthaman, Cookie Murphy, Isidor Sauers, Dominic F. Lee, Alvin R. Ellis, S. William Schwenterly, and Fred A. List III.

Second row: James R. Thompson, H. Richard Kerchner, Ben W. McConnell, Amit Goyal, Tolga Aytug, J. Winston Lue, Ron Feenstra, Sylvester W. Cook, John P. Stovall, Michael J. Gouge, Keith J. Leonard, Patrick M. Martin, Claudia Cantoni, M. Matthew Kowalewski, and Jaeun Yoo.

Back row: Eliot D. Specht, Jonathan A. Demko, David B. Beach, Robert Grabovickic, Srivatsan Sathyamurthy, D. Randy James, Donald M. Kroeger, Joseph A. Marasco, Larry M. Dickens, and Robert A. Hawsey.

Not available for photo: Noel Rutter, John D. Budai, Hans M. Christen, Robert C. Duckworth, Paul F. Fisher, Albert Gapud, and Sukill Kang.

# Contents

# List of Figures

# List of Tables

# Abbreviated Terms

## NOMENCLATURE

| | |
|---|---|
| $B_{irr}$ | irreversibility field |
| $I_c$ | critical current |
| $I_p$ | peak current |
| $I_{mp}$ | propagation current |
| $I_{rms}$ | root mean square cable current |
| $J_c$ | critical current density |
| $J_e$ | engineering critical current density |
| $K_c$ | critical current per unit width of conductor (Ic/w) |
| $P_{base}$ | base pressure |
| $T_c$ | critical temperature/transition temperature |

## ACRONYMS AND INITIALISMS

| | |
|---|---|
| ac | alternating current |
| ACCI | Accelerated Coated Conductor Initiative |
| AES | Auger electron spectroscopy |
| ANL | Argonne National Laboratory |
| ASC | American Superconductor Corporation |
| BIL | basic impulse level |
| BSCCO | Bi-Sr-Ca-Cu-O |
| CRADA | cooperative research and development agreement |
| dc | direct current |
| DOE | U.S. Department of Energy |
| DOE-HQ | DOE Headquarters |
| e-beam | electron beam |
| EDS | energy-dispersive spectroscopy |
| EDX | energy-dispersive X-ray diffractometer |
| FLC | Federal Laboratory Consortium for Technology Transfer |
| FWHM | full width at half maximum |
| HRSEM | high-resolution scanning electron microscope |
| HTS | high-temperature superconductivity/superconductor/superconducting |
| HV | high vacuum |
| IBAD | ion-beam-assisted deposition |
| ICP | inductively coupled plasma |
| LANL | Los Alamos National Laboratory |
| $LN_2$ | liquid nitrogen |

| | |
|---|---|
| LSMO | $La_{0.7}Sr_{0.3}MnO_3$ |
| LTR | Laboratory Technology Research (DOE program) |
| LTS | low-temperature superconductor |
| LZO | lanthanum zirconium oxide ($La_2Zr_2O_7$) |
| MBE | molecular beam epitaxy |
| MOCVD | metal-oxide chemical vapor deposition |
| MOD | metal organic decomposition |
| ORNL | Oak Ridge National Laboratory |
| PLD | pulsed-laser deposition |
| R&D | research and development |
| RABiTS™ | Rolling-Assisted Biaxially Textured Substrates |
| RBS | Rutherford Backscattering Spectroscopy/Spectrum |
| rf | radio frequency |
| RGA | residual gas analyzer |
| RHEED | reflection high-energy electron diffraction |
| rms | root mean square |
| SAIC | Science Applications International Corporation |
| SEM | scanning electron microscopy |
| SIMS | secondary ion mass spectrometry |
| SPI | Superconductivity Partnership Initiative |
| SQUID | superconducting quantum interference device |
| WES | Waukesha Electric Systems |
| XRD | X-ray diffraction |
| YBCO | yttrium barium copper oxide ($YBa_2Cu_3O_{7-\delta}$) |
| YSZ | yttria-stabilized zirconia |

# Executive Summary

The Oak Ridge National laboratory (ORNL) Superconducting Technology Program is conducted as part of a national effort by the U.S. Department of Energy's Office of Energy Efficiency and Renewable Energy to develop the science and technology base needed by U.S. industry for development of electric power applications of high-temperature superconductivity. The two major elements of this program are wire development and applications development. A new part of the wire research effort was the Accelerated Coated Conductor Initiative.

This document describes the major research and development activities for this program together with related accomplishments. The technical progress reported was summarized from recent open literature publications, presentations, and information prepared for the FY 2001 Annual Program Review held August 1–3, 2001. Aspects of ORNL's work that were presented at the International Cryogenic Materials Conference/Cryogenic Engineering Conference (July 2001) are included in this report as well.

This ORNL program is highly leveraged by the staff and other resources of U.S. industry and universities. Interlaboratory teams are also in place on a number of industry-driven projects. Working group meetings, staff exchanges, and joint publications and presentations ensure that there *is* technology transfer with U.S. industry. Working together, the collaborative teams are making rapid progress in solving the scientific and technical issues necessary for the commercialization of long lengths of practical high-temperature superconductor wire and wire-using systems.

# Highlights

## WIRE DEVELOPMENT

- Two major new laboratories were renovated and equipped as part of the Accelerated Coated Conductor Initiative (ACCI). One laboratory houses conductor-processing facilities, and the other houses conductor-characterization facilities. Office space for two industrial partners and three postdoctoral fellows has been included in the laboratory design. To support the ACCI research activities at ORNL, two new staff members and three new postdoctoral fellows have been hired. Over $1M in new equipment was purchased for these laboratories. Industry has been involved through secure web-based exchange of long-length texture data, joint experiments, and equipment specifications. On-site industry assignments are anticipated in FY 2002.

- A reel-to-reel tape handler mounted on a four-circle diffractometer was used to provide a characterization by X-ray diffraction (XRD) of the entire 1-m length of a $YBa_2Cu_3O_{7-\delta}$ (YBCO)/$CeO_2$/yttria stabilized zirconia (YSZ)/$CeO_2$/Pd/Ni tape. The YBCO was converted ex situ from Y, $BaF_2$, and Cu codeposited by electron-beam (e-beam) deposition. Rocking curve full width at half maximums (FWHMs) (mean ± standard deviation) for 95 segments of 1-cm length are as follows: YBCO(005) = 6.2 ± 0.5°, YSZ(002) = 10.4 ± 0.4°, and Ni(002) = 7.6 ± 0.3°. Phi scan FWHMs are as follows: YBCO(113) = 9.6 ± 0.4°, YSZ(111) = 13.0 ± 0.4°, and Ni(111) = 10.6 ± 0.4°. More than 95% of the tape at each point is cube-textured from Ni to YBCO. The critical current density ($J_c$) is 0.40 ± 0.04 MA/cm$^2$ and is inversely correlated with the rocking curve FWHM. Calculations suggest that $J_c$ might be increased by a factor of 3.7 by producing a sharper texture and that the uniformity of the texture will support scaling to kilometer lengths.

- Coated conductor applications in power technologies require stabilization of the high-temperature superconducting (HTS) layers against thermal runaway. Conductive $La_{0.7}Sr_{0.3}MnO_3$ (LSMO) has been epitaxially grown on biaxially textured Ni substrates as a single buffer layer. The subsequent epitaxial growth of YBCO coatings by pulsed-laser deposition (PLD) yielded self-field $J_c$s of $0.5 \times 10^6$ A/cm$^2$ at 77 K and provided good electrical connectivity over the entire structure (HTS + conductive-buffer + metal substrate). Property characterizations of YBCO/LSMO/Ni architecture revealed excellent crystallographic and morphological properties. These results have demonstrated that LSMO, used as a single, *conductive* buffer layer, may offer potential for fully stabilized YBCO coated conductors.

- We have fabricated superconducting $MgB_2$ films with a sharp critical temperature ($T_c$) of 39 K on $Al_2O_3$ single-crystal substrates by using e-beam–evaporated B films followed by post-annealing. Detailed XRD studies indicate that the film is polycrystalline with some degree of *c*-axis texture. A transport $J_c$ of more than $4 \times 10^6$ A/cm$^2$ was obtained on $MgB_2$ films at 25 K. The irreversibility field ($B_{irr}$) obtained from the transport measurements on $MgB_2$ films indicates that there may be some improvement in flux pinning at lower temperatures.

- High-current-density YBCO films were fabricated on rolling-assisted biaxially textured substrates (RABiTS™) with a layer sequence of $CeO_2$/YSZ/(dip-coated or e-beam seed)/Ni-W (3 at. %). E-beam evaporation was used to deposit $Y_2O_3$ seed layers. A reel-to-reel continuous dip-coating unit was used to deposit $Gd_2O_3$ and $La_2Zr_2O_7$ (LZO) seed layers. Highly aligned, continuous, and crack-free $Y_2O_3$, $Gd_2O_3$, and LZO seed layers were obtained. Radio-frequency (rf)-magnetron sputtering was used to deposit both YSZ and $CeO_2$ cap layers on all of the seed layers. The YBCO films were then grown on these buffered Ni-W substrates by either PLD or an ex situ $BaF_2$ precursor process. A high

$J_c$ of 1.9 MA/cm$^2$ at 77 K and self-field was obtained on both $Y_2O_3$ and LZO seed layers. The performance of solution seed layers approached that of the vacuum seed layers.

- A new critical-current measurement system for tapes as long as 8 m has been developed and tested. If appropriate probes are used, critical currents can be measured for segments as small as 2 cm on these tapes.

- A series of biaxially textured $Ni_{1-x}Cr_x$ materials with compositions $x$ = 0, 7, 9, 11, and 13 at. % Cr have been studied for use as substrate materials for coated conductors in HTS applications. The magnetic properties were investigated, including the hysteretic loss in an Ni-7 at. % Cr sample that was controllably deformed. Complementary XRD studies show that thermomechanical processing produces nearly complete {100}<100> cube texturing, as desired for applications.

- The epitaxial deposition of the first oxide buffer layer (seed layer) on biaxially textured Ni tape for coated conductors is a critical step that is dependent on the atomistic surface condition of the metal. We present a study of the RABiTS™ Ni (001) surface and seed-layer growth in which in situ reflection high-energy electron diffraction and auger electron spectroscopy are used. Our observations are consistent with the formation of a c(2 × 2) two-dimensional superstructure caused by surface segregation of sulfur contained in the metal. We show that this superstructure can have a dramatic effect on the heteroepitaxial growth of oxide seed layers. In particular, the surface superstructure promotes the (200) epitaxial oxide growth of YSZ, which is necessary for the development of high-$J_c$ superconducting films for coated conductors.

- First results are reported of a study directed at raising the critical current ($I_c$) by increasing the YBCO thickness of YBCO coated conductors processed ex situ. The substrates are RABiTS™, produced by laboratory- and industrial-scale processes and by laboratory-scale ion-beam-assisted deposition (IBAD) of YSZ. Starting from an initial thickness of 0.3 μm, significant improvements (by a factor of 3 to 4) in $I_c$ were obtained for 1.5- to 3-μm-thick YBCO on the industrial-scale RABiTS™. The enhancements for ex situ YBCO were similar to those obtained for thick YBCO produced by an in situ PLD process. A maximum current of 200 A/cm width (77 K) was measured for a 1-μm-thick YBCO coating on IBAD YSZ. The relative contributions of the effects of thickness and texture to a high $I_c$ are discussed.

- High-current-density YBCO films with a layer sequence of $CeO_2$/YSZ/$Y_2O_3$/Ni-alloy were fabricated on RABiTS™ by using an ex situ $BaF_2$ precursor process. Biaxially textured Ni-W (3 at. %) substrates, which are stronger than nickel but have reduced magnetism, were chosen for this study. The $Y_2O_3$ seed layers were successfully grown by reactive e-beam evaporation directly onto the Ni-W (3 at. %) substrates. Highly aligned, continuous, and crack-free $Y_2O_3$ layers were obtained. Both YSZ and $CeO_2$ layers were deposited by rf-magnetron sputtering. The YBCO films were grown by applying e-beam-evaporated Y-$BaF_2$-Cu precursors and post-annealing. A high $J_c$ of 1.9 MA/cm$^2$ at 77 K and self-field was obtained on the substrates.

## APPLICATIONS DEVELOPMENT

- A distinctive normal-zone propagation was measured for a research sample of YBCO/RABiTS™. Propagation velocities between 1.4 and 8.3 mm/s were measured for currents up to 30 A. Away from a tape hot spot, the propagation velocity is insensitive to the initial energy introduced into the tape.

- A prototype triaxial HTS cable, ~1.5 m long, has been fabricated by Southwire Company and tested at Oak Ridge National Laboratory (ORNL). Each phase consists of two layers of Bi-Sr-Ca-Cu-O (BSCCO)-2223 HTS tapes. Electrical tests of the cable included direct-current V-I curves and alternating-currrent (ac) loss measurements. The ac losses were measured both electrically and calorimetrically. Finite-element thermal modeling was performed to check the calorimetric calibration. Individual phase ac losses indicate good agreement with the monoblock theory. The total three-phase ac loss is close to that of the sum of the three individual phases. The concentricity of the phases was not responsible for significant ac loss. A total three-phase ac loss of 1 W/m was measured at the design operating current of 1250 A.

- An HTS transmission cable splice with a cold dielectric construction rated at 1250-A phase-to-ground voltage has been fabricated by Southwire Company and has been tested at ORNL. The 5-m cable passed all of the high-voltage tests and demonstrated the feasibility of splicing cold dielectric HTS cables.

- AC loss testing at variable frequencies was completed at 24 K on IGC-SuperPower sample coils No. 3 and No. 4. The No. 4 coil used the actual conductor selected for the 5/10-MVA Superconductivity Partnership Initiative transformer. The cooling system for the transformer, an ORNL responsibility, was analyzed and incorporated into detailed design drawings. An outside shop was awarded the fabrication contract. High-voltage ac, impulse, partial-discharge, and dielectric-loss measurements continued.

- Termination design No. 2 for the Southwire cable system has successfully passed all ac withstand and impulse testing.

- A 20-cm long YBCO/RABiTS™ tape was used to conduct normal zone propagation experiments in liquid nitrogen. No propagation was observed for the conditions tested. A silver coating, used to protect the YBCO film from environmental degradation, also appears necessary to ensure a good current path during high-current upset conditions.

- The over-current short-circuit fault-simulation tests were performed on the first 5-m spliced HTS cable built by Southwire. In the first series, pulse currents of up to 11 kA were applied to the cable for 2 s and up to 14 kA were applied for 1 s. In the second series, repeated shots with a pulse current of 11.7 kA were applied to the cable for 0.5 to 2 s. Because of the alloy sheath used for the present HTS tape, higher voltage and temperature rise were observed in these tests than in previous tests on the 5-m cable No. 2. This difference was also evidenced by a rise in coolant temperature after the shots. No damage to the cable or to the splice was observed.

## PROGRAMMATIC

- Three new documents were completed and posted on the ORNL HTS web site, http://www.ornl.gov/HTSC/htsc.html. The *Cryogenics Roadmap* and the *Cryogenic Implementation Plan* were assembled and posted. In addition, an extensively revised and updated version of *An Analysis of Future Prices and Markets for High Temperature Superconductors* (the "Mulholland Report") was completed. The report contains a detailed identification of the analysis pathways in the original Mulholland spreadsheet, identification of assumptions, examination of the specific device models, extension of the analysis period to 2025, and recalculations to reflect these changes.

# 1. Technical Progress in Wire Development

## 1.1 ORNL ACCELERATED COATED CONDUCTOR INITIATIVE (ACCI)

*F. A. List, D. F. Lee, L. Heatherly, J. Yoo, and D. M. Kroeger*

The purpose of the Oak Ridge National Laboratory (ORNL) Accelerated Coated Conductor Initiative (ACCI) is to accelerate the development, commercialization, and application of high-temperature superconductors (HTSs) through joint efforts among U.S. Department of Energy (DOE) laboratories, American industry, and universities so that future challenges of the electric power industry can be met. Our primary objectives for FY 2001 were

1. to identify and prepare suitable high-quality laboratory space for use by DOE laboratories and partners, and
2. to develop new equipment needed for more rapid preparation and characterization of coated conductors.

For FY 2001, we identified and renovated ~2200 ft$^2$ of laboratory space to accommodate the facilities. Two adjacent laboratories have been created—one housing conductor processing facilities and the other housing conductor characterization facilities (Figs. 1.1 and 1.2). Office space for two industrial partners and three postdoctoral associates has been included in the laboratory design. To support the ACCI research activities at ORNL, two new staff members and three new postdoctoral fellows have been hired.

New equipment added to the ACCI laboratory space can be divided into three general categories: characterization equipment, deposition equipment, and precursor conversion equipment. A discussion of this new equipment follows.

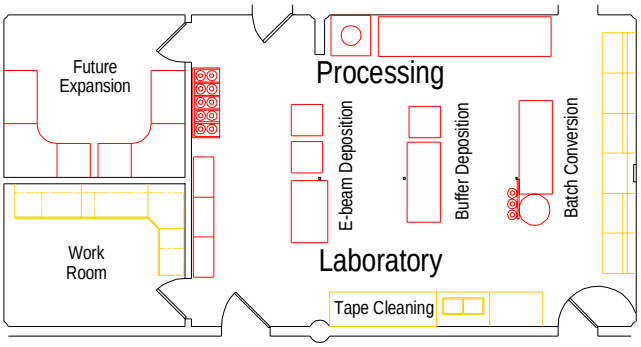


**Fig. 1.1. Floor plan of the ACCI Processing Laboratory (~1000 ft$^2$).**

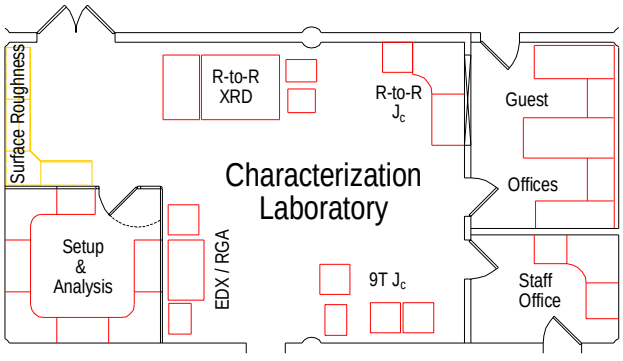


**Fig. 1.2. Floor plan of the ACCI Characterization Laboratory (~1000 ft$^2$).**

### 1.1.1 Characterization Equipment

Fabrication of coated HTS conductors involves sequential deposition of several epitaxial layers. The quality of any layer depends on both the conditions during the growth of that layer and the quality of the underlying layer(s). Characterization of the quality of each layer is important in order to develop a successful fabrication process. Equipment we have developed recently for the ACCI to characterize conductors includes a new X-ray diffraction (XRD) system, a surface roughness measurement system, and an optical examination system.

#### 1.1.1.1 New X-Ray Diffraction System

XRD has been the principal tool for feedback in development of the coated conductor process. Both the crystalline phase content and the epitaxy of deposited films can be obtained rapidly. Thus far, a single X-ray diffractometer equipped with a reel-to-reel tape handler has provided characterization of as much as 60 m of tape per week. Several research programs share the present system. To satisfy the increasing demands for X-ray characterization of coated conductors, a new dedicated reel-to-reel X-ray diffractometer is being assembled (Fig. 1.3). The new system uses a sealed-tube X-ray source that is collimated and monochromated using a meridionally bent, variable-period multilayer film. Throughput of the new dedicated system is expected to be higher than that of the present shared system.

**Fig. 1.3. New reel-to-reel X-ray diffractometer.**

#### 1.1.1.2 Surface Roughness Measurement System

Knowledge of the microscopic roughness of the surface of a substrate at all stages during conductor fabrication may help to identify process deficiencies. Roughness data are particularly useful when they can be obtained continuously for a length of tape and be correlated to similar data (e.g., X-ray, optical, and Auger) obtained for the same length. A reel-to-reel surface roughness measurement system has been developed to acquire surface roughness data for tapes as long as 40 m (see Fig. 1.4). Central to the system is a commercially available surface roughness measurement gage (from Optical Dimensions, LLC). Optical roughness is determined from measurements of the reflectance and scattering of a helium laser. The average roughness of an area 1 × 5 mm can be sampled at a rate of ~13 readings/s. At this rate, the roughness of ~50 m of tape can be measured in 1 h. Figure 1.5 shows roughness data obtained for ~11 m of fully buffered RABiTS™ tape. The average roughness for this buffered tape is ~41 nm—about 2.5 times that measured for the bare nickel substrate. The three indentations provided for reference are clearly visible at position ~9.925 m (see the inset in Fig. 1.5).


**Fig. 1.4. Reel-to-reel surface roughness measurement system.**

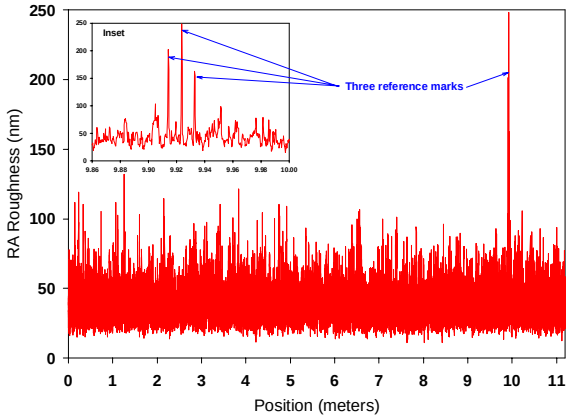


**Fig. 1.5. Roughness data obtained for an 11-m length of buffered tape.**

#### 1.1.1.3 Optical Examination System

To provide position-referenced optical images of tape, an optical microscope has been equipped with a reel-to-reel tape handler (see Fig. 1.6). Optical images of tape for specific positions of interest can be obtained with this equipment. Figure 1.7 shows a low-magnification optical image of the same tape as that of Fig. 1.5 at position 9.9250 m. The three reference indentations are visible. A higher-magnification image at 9.9250 m (Fig. 1.8) shows individual nickel grains (50–100 mm in diameter) around a single indentation.

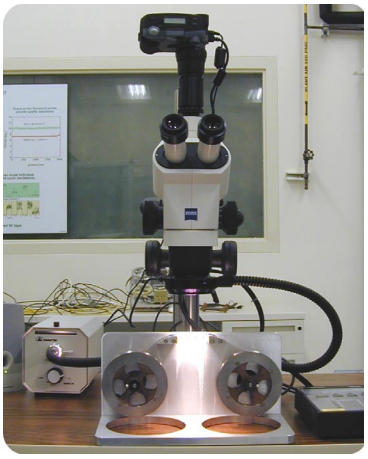

**Fig. 1.6. Reel-to-reel optical examination system.**

### 1.1.2 Deposition Equipment for Higher-Rate Sputtering

Two layers of the coated conductor are deposited by radio frequency (rf) sputtering of oxides targets—a yttria-stabilized zirconia (YSZ) layer and a $CeO_2$ cap layer. The tape speed required to deposit a suitably thick layer using an existing 2-in.-diam sputter target is 6 cm/h for the YSZ layer and 30 cm/h for the $CeO_2$ cap layers. With 2-in. targets, ~200 h (~8.3 days) are needed to deposit these two layers sequentially on a 10-m length of substrate. A new sputter system has been constructed to increase the production rate of coated conductor (Fig. 1.9).

The new system includes three 24-in.-long linear sputter sources. Each source can be operated at up to 3 kW rf power. Initial tests of deposition rates indicate that tape speeds of 1 m/h are achievable even for operation at 500 W rf power.

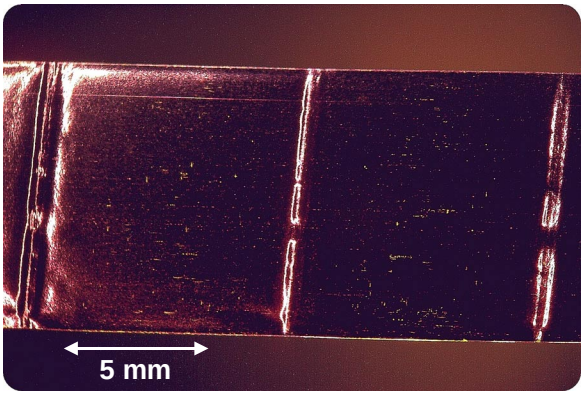


**Fig. 1.7. Low-magnification optical image of buffered tape at position 9.9250 m showing three reference marks.**

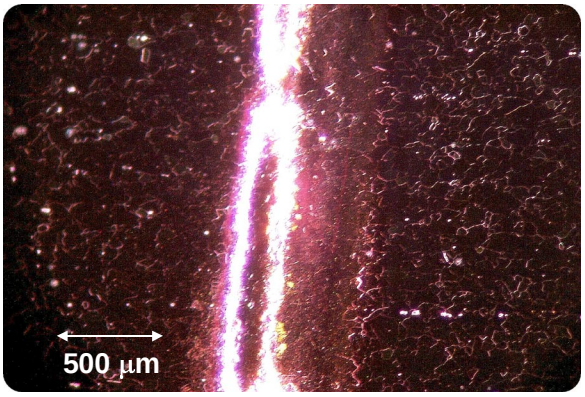


**Fig. 1.8. Higher-magnification optical image of buffered tape at position 9.9250 m showing a single reference mark and nickel grains.**

### 1.1.3 Precursor Conversion Equipment

In the course of investigating continuous ex situ $BaF_2$ precursor conversion using our reel-to-reel reaction furnace, we have encountered various issues that can affect both the conversion rate and the performance of the yttrium barium copper oxide (YBCO)–coated conductor. Among these are incomplete conversion caused by sample tilting, gas-flow characteristics associated with nozzle design, and efficiency of HF removal. To a certain extent, all these issues are related to the $HF/H_2O$ ratio at the surface of the sample during the precursor decomposition and YBCO formation process. In order to clarify these issues, we have built three new conversion systems: a variable gas-injection conversion chamber, a low-pressure conversion system, and a batch conversion system. The first two of these systems are described subsequently. The batch conversion system is discussed at a later date.

#### 1.1.3.1 Variable Gas-Injection Conversion Chamber

The variable gas-injection conversion chamber has three main features:

1. variable angles between the sample and both gas inlet and outlet ports,
2. variable nozzle designs for both gas inlet and outlet ports, and
3. the capability of reduced chamber pressure during conversion by pumping.

A photograph of the conversion chamber is shown in Fig. 1.10. This Inconel 601 chamber, consisting of a single reaction zone, sits in the cradle of a single-zone tube furnace. One end of the chamber is equipped with a multiport flange that can accommodate gas inlet and outlet tubes. The sample holder, shown in Fig. 1.11, is located at the center of the chamber and is capable of both transverse- and longitudinal-flow sample-gas geometry. By inserting the gas inlet and outlet at various ports, a wide variety of sample-gas injection-exhaust orientations can be investigated. This capability is desirable because during our continuous conversion study, sample tilting away from the gas inlets has resulted in incomplete reaction and hence reduced $J_c$ performance. A better understanding of the effect of gas impinging angle on conversion will enable us to modify our large-scale systems to ensure that the precursor will always be exposed to the gas while avoiding the creation of unwanted stagnant regions on the sample surface.

In addition to the variable-angle capability, the gas inlet and outlet nozzle design can also be altered. Various inlet and outlet tubes with different-diameter holes, as well as slots, have been fabricated. By use of these tubes, a multitude of nozzle combinations can be introduced. Additional nozzle designs can easily be incorporated simply by fabricating new tubes. This capability will enable us to study the possible existence of jetting as well as gas-flow homogeneity. In addition, larger exhaust ports may enable us to reduce chamber pressure buildup during processing and provide a better refreshing rate of HF within the chamber—issues that have been encountered in our continuous conversion work.

Finally, the chamber is capable of operation at reduced chamber pressure by pumping at the exhaust. A pressure controller, an actuation valve, and a high-capacity mechanical pump are integrated into the chamber to provide constant chamber pressure during the entire conversion cycle. In addition, gas flow rate can be controlled independent of the chamber pressure with mass flow controllers. This capability will allow us to

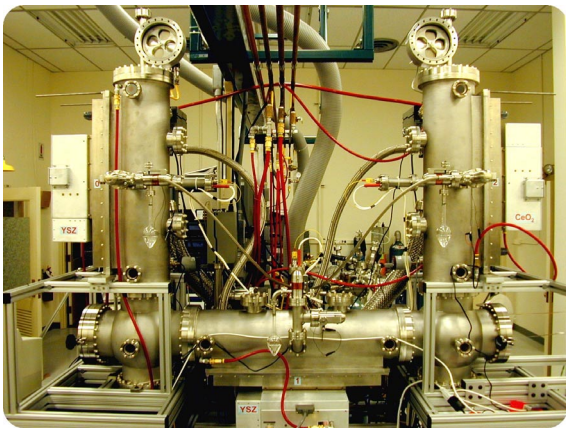

**Fig. 1.9. Higher-rate buffer layer deposition system.** The three 24-in.-long linear sputter sources form a U shape.

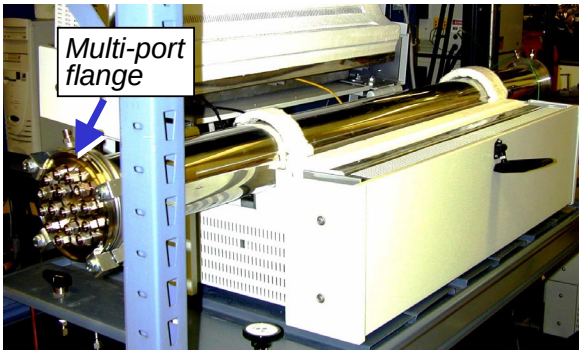


**Fig. 1.10. The variable gas-injection conversion chamber.** One end of the chamber is equipped with a multiport flange to accommodate a variety of sample-gas orientations.

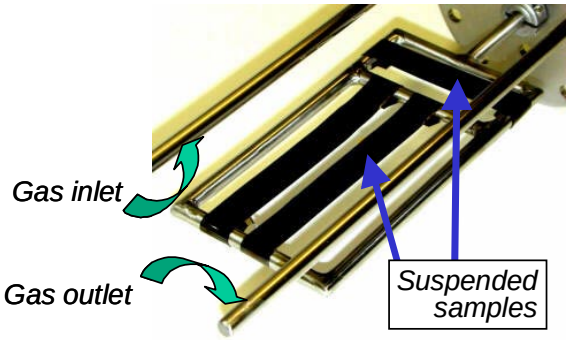


**Fig. 1.11. The sample holder together with the gas inlet and outlet tubes.** Samples can be suspended in both transverse and longitudinal orientations with respect to the direction of gas flow.

investigate whether pumping can alleviate the problem of HF removal that we encountered in the long-length work. Also, we may gain additional information on whether an anticipated decrease in surface boundary layer thickness will bring about more homogeneous conversion in larger areas. Results from these investigations should be directly applicable to the design of our next-generation long-length conversion chamber.

Once the chamber was set up, we conducted initial experiments to familiarize ourselves with the furnace operation and to calibrate the oxygen partial pressure at various flow rates by mixing $N_2$ and Ar-2% $O_2$ gases. For these initial tests, we used gas inlet and outlet tubes with 25-μm holes. During calibration, oxygen partial pressure was continuously monitored while the gases were introduced and controlled by mass flow controllers. Figure 1.12 provides an example of how oxygen partial pressure varies with time for the present chamber at a nitrogen flow rate of 3.3 L/min and an Ar-$O_2$ flow rate of 28 $cm^3$/min. As this figure indicates, even with evacuation and nitrogen back-filling, roughly 20 min was needed for the oxygen to be completely purged from the chamber. In addition, approximately 40 min was necessary for the oxygen partial pressure to stabilize to the desire value. This and similar results at other flow rates indicate that a waiting time of roughly 1 h is needed before commencing heat-up and conversion in this chamber.

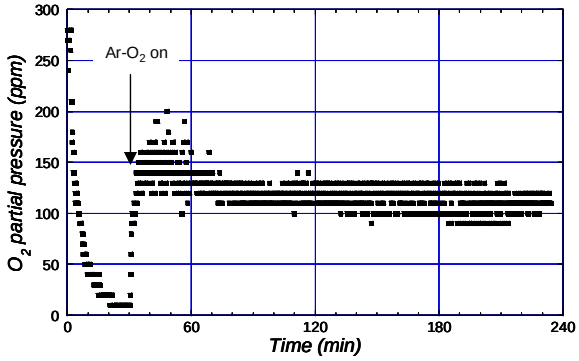


**Fig. 1.12. Variation in oxygen partial pressure with time in the variable gas-injection chamber at an $N_2$ flow rate of 3.3 L/min and an Ar-$O_2$ flow rate of 28 $cm^3$/min.**

Beside oxygen partial pressure, variation in chamber pressure during heat-up also needs to be considered. Figure 1.13 shows the chamber pressure as a function of temperature for a nitrogen flow rate of 3.3 L/min and an Ar-$O_2$ flow rate of 28 $cm^3$/min. Note that chamber pressure increases with temperature because of increased gas viscosity and the small size of the exhaust nozzle. Knowing the actual pressure is important in our system to maintain a prescribed oxygen partial pressure within the chamber. Of course, the pressure will vary a case-by-case basis, depending on the specific flow rate and the nozzle design. Following these preliminary experiments, work is now under way to study the effects of the gas impinging angle.

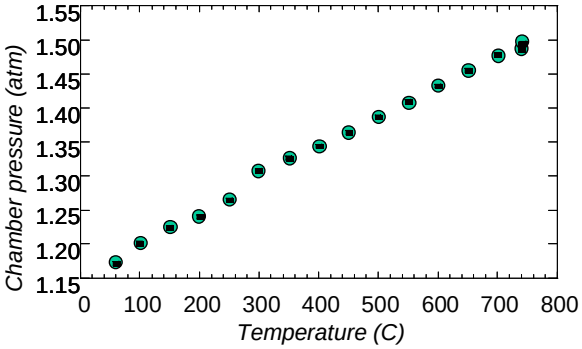


**Fig. 1.13. Chamber pressure as a function of temperature in the variable gas-injection chamber at an $N_2$ flow rate of 3.3 L/min and an Ar-$O_2$ flow rate of 28 $cm^3$/min.**

### 1.1.3.2 Low-Pressure Conversion System

The conversion of the $BaF_2$ precursor to YBCO involves a gas phase exchange of $H_2O$ and HF. For a conversion performed at 1 atm total pressure, the viscosity of the gas phase affects the rates of exchange of $H_2O$ and HF, and consequently the rate and efficiency of the conversion. To reduce some of the complexities associated with conversion at 1 atm (e.g., boundary layers and turbulence), and perhaps to facilitate more rapid conversion and more efficient gas utilization, we constructed a new low-pressure

$BaF_2$ precursor conversion system (see Fig. 1.14). A vacuum system capable of $2 \times 10^{-7}$ Torr base pressure houses a tape heater, a residual gas analyzer (RGA), and an energy-dispersive X-ray diffractometer (EDX). The tape heater, shown in Fig. 1.15, allows precursor tapes up to 3 cm long to be resistively heated at rates up to 10°C/s. During heating, the temperature of the tape is monitored and controlled with a thermocouple spot-welded to the tape's back side. Also during heating, the composition of the gas phase and the crystalline phase content of the precursor can be monitored with the RGA and the EDX, respectively. Figure 1.16 shows the gas phase evolution of HF that accompanies the conversion of precursor.

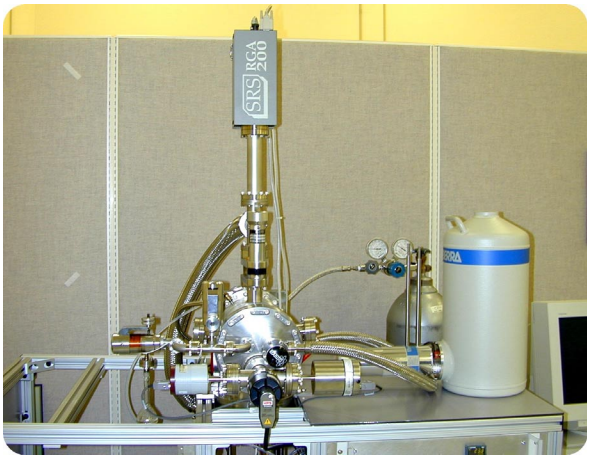


**Fig. 1.14. Low-pressure $BaF_2$ conversion system.**

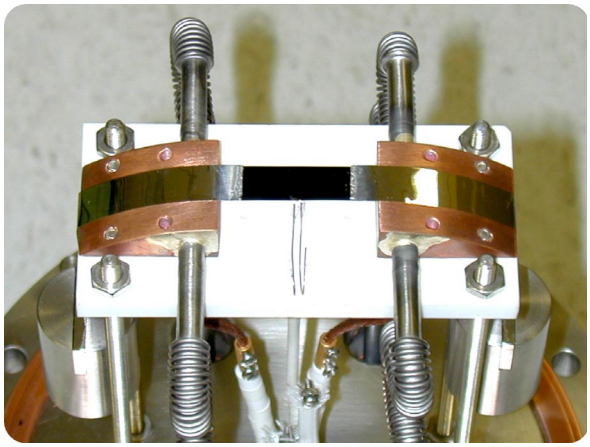

**Fig. 1.15. Tape heater for the low-pressure $BaF_2$ conversion system.** Precursor tape (black) lies between two copper current electrodes.

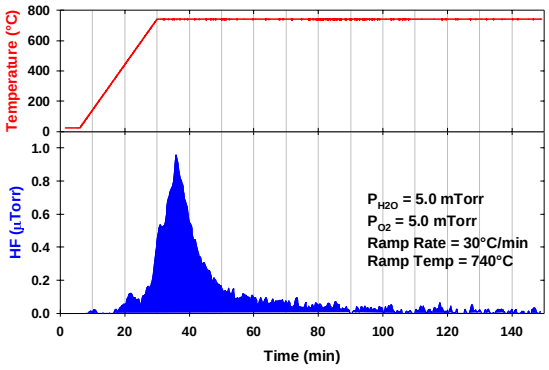


**Fig. 1.16. HF evolution from a precursor during a thermal ramp.**

## 1.2 EFFECT OF SULFUR SURFACE STRUCTURE ON NUCLEATION OF OXIDE SEED LAYERS ON TEXTURED METALS FOR COATED CONDUCTOR APPLICATIONS

*C. Cantoni, D. K. Christen, A. Goyal, L. Heatherly, F. A. List III, G. W. Ownby, D. M. Zehner, and H. M. Christen (Oak Ridge National Laboratory), and D. P. Norton (University of Florida, Gainesville)*

### 1.2.1 Introduction

The rolling-assisted biaxially textured substrates (RABiTS™) technology is based on the epitaxial growth of oxide buffer layers on a textured metal. This process is intrinsically complex because of the different chemical and electronic natures of the two surfaces involved. Changes in the atomistic structure and free energy of the metal surface determined by chemisorbed species can have a dramatic influence on the nucleation of the seed layer and ultimately determine the crystallographic orientation of the film. Although several groups have conducted accurate studies of the atomistic surfaces of d-band metals like nickel since 1960, these studies were not oriented towards understanding the heteroepitaxial nucleation of different oxide buffer layers on the metal. We were motivated to investigate the influence of surface physical and chemical properties on oxide film nucleation by inconsistencies in the seed layer texture of long lengths of RABiTS™. In fact, continuous processing of meter-long tapes is much more sensitive to local imperfections than short-sample fabrication processes, in which poor-quality samples can be individually discarded.

Although several different seed layer oxides have been successfully grown on textured Ni over the past few years by different techniques, the previous work was based on an incomplete understanding of Ni surface properties. In particular, the seed layer was assumed to nucleate on a clean and pure Ni surface that was obtained by annealing in forming gas before deposition.

Therefore, we conducted a study of seed layer growth on {100}<100> Ni using a laser ablation molecular beam epitaxy (MBE) chamber equipped with a reflection high-energy electron diffraction (RHEED) system, a mass spectrometer, and a pulsed KrF excimer laser ($\lambda = 248$ nm). In situ RHEED allowed continuous monitoring of surface structural changes during Ni substrate annealing and oxide deposition. A chemical analysis of the textured Ni surface was conducted using Auger electron spectroscopy (AES) in a separate ultrahigh-vacuum chamber. Our study shows that the structure and chemical composition of the textured Ni surface has a profound effect on the heteroepitaxial growth of the oxide seed layer.

### 1.2.2 Characteristics of the c(2 × 2)-S Superstructure

After cold rolling and recrystallization annealing, cube-textured Ni substrates typically have grain sizes and surface roughnesses of 50 to 100 μm and 5 to 10 nm, respectively. The degree of grain alignment is expressed by a full width at half maximum (FWHM) of 6 to 10° for the in-plane and out-of-plane grain-boundary misorientation distributions. Previous inductively coupled plasma (ICP) analyses on similar samples of Ni tape indicated the presence of C and S as major impurities in the bulk, with concentrations of less than 100 and 30 wt ppm, respectively. The samples were heated to 550°C in high vacuum ($P_{base} = 1 \times 10^{-8}$ Torr) for 1 h to remove weakly bound species that had adsorbed on the surface after air exposure. This step was sufficient to remove any trace of hydrocarbons and oxygen on the sample surface, as revealed by AES.

The RHEED patterns obtained after the heat treatment are shown in Fig. 1.17 for two different orientations: with the incident electron beam parallel to <100> [Fig. 1.17(a)] and with the beam parallel to <110> [Fig. 1.17(b)]. Although the diffraction patterns are broadened because of the orientation distribution of the grains (the electron beam samples a few hundred grains), the RHEED streaks are well defined and distinct. The pattern in Fig. 1.17(a) shows two extra streaks (indicated by arrows) in addition to the reflections observed for a clean Ni (001) surface pattern. The extra streaks are positioned halfway between the Ni streaks and are not observed in the <110> pattern. This situation is consistent with the presence of a c(2 × 2) superstructure on the {100}<100> Ni surface. Such a superstructure was observed on all the samples examined and could not be removed by annealing in vacuum, or in Ar mixed to 4% H2 up to temperatures of 850°C. A superstructure-free Ni RHEED pattern was obtained by depositing a Ni overlayer in situ by pulsed-laser deposition (PLD) from a 99.99% pure Ni target.

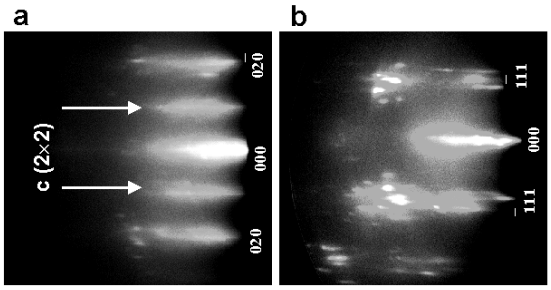


**Fig. 1.17. RHEED patterns obtained from the {100}<100> Ni surface after 1-h anneal at 500°C with the incident electron beam along <100> (a) and along <110> (b).** The Ni reflections are indexed; arrows indicate the superstructure streaks.

AES was performed on several {100}<100> Ni substrates that had been produced in different batches. All the samples investigated showed a distinct sulfur peak in the spectrum under conditions at which the superstructure was clearly visible by RHEED. The results from a typical AES experiment are shown in Fig. 1.18. Oxygen and carbon were detected on the sample surface at room temperature, but they completely desorbed after a 10-min anneal at 550°C. At this temperature, a S signal was detected. The intensity of the S signal was nearly constant across the sample and up to temperatures of 900°C. The percentage of S indicated in Fig. 1.18 was determined by the ratio between the S peak at 152 eV and the Ni peak at 61 eV corrected by the appropriate sensitivity factors. Since AES is sensitive to layers of about 5 Å, these values can differ substantially from the real atomistic concentration at the surface.

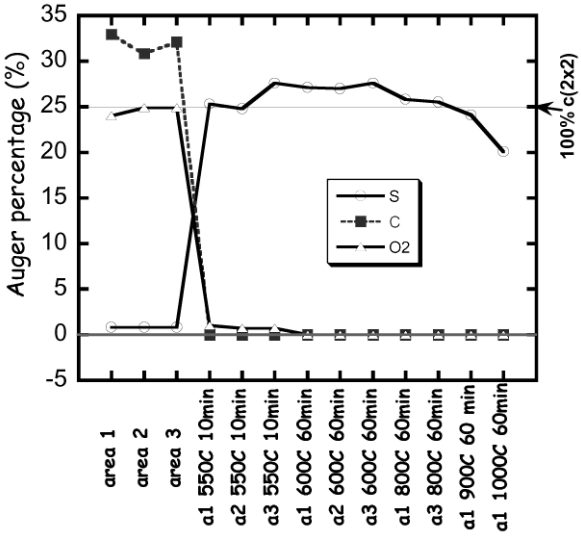


**Fig. 1.18. Percentages of the elements detected by Auger spectroscopy on {100}<100> Ni as a function of annealing temperatures.** The arrow on the right indicates an S surface concentration of approximately 0.5 ML, corresponding to complete coverage of the c(2 × 2) layer.

Subsequent studies showed that the percentage value of S measured in this temperature range corresponded approximately to a single c(2 × 2) layer covering the entire Ni surface. A reduction in the intensity of the S peak compared with the Ni signal took place at temperatures above 900°C, presumably because of S evaporation. Ion-sputtering the Ni surface for 10 min using $Ar^+$ ions with an energy of 200 eV was sufficient to eliminate the S signal.

A small C signal was always detected after ion bombardment, even after repeated treatments, indicating the presence of this contaminant element throughout a near-surface layer. Although the spectra

acquired after ion bombardment showed traces of C, the S signal was progressively recovered after anneals in vacuum at a temperature of 430°C or higher. After a 1-h anneal at 800°C, the S surface coverage returned to the previous value of ~0.5 ML, corresponding to one complete monolayer of c(2 × 2). [In the c(2 × 2) layer, the ratio between S atoms ($N_S$) and Ni atoms ($N_{Ni}$) is 0.5. If one monolayer is defined as the number of Ni atoms per unit area, a complete c(2 × 2) superstructure has a coverage of $\theta = N_S/N_{Ni} = 0.5$.monolayer.] The observation of S after annealing was associated with the decrease and ultimate disappearance of the C peak.

Collectively, the AES and RHEED experiments indicate that the c(2 × 2) superstructure forms after diffusion and surface segregation of S atoms originating from substitutional sites in the Ni lattice. Sulfur is relatively immobile below 400°C but can readily diffuse and segregate to the free surface during the initial Ni fabrication (e.g., during the high-temperature recrystallization anneal). By contrast, C atoms, which occupy Ni-lattice interstitial positions, are very mobile and desorb at much lower temperatures.

AES and RHEED analysis of laser-deposited Ni overlayers indicated that these films did not contain any detectable amount of S superstructure. In these samples, the segregation of S to the surface and the consequent formation of the c(2 × 2) superstructure occurred only after the S atoms had diffused through the entire Ni overlayer. Formation of the S superstructure on a 500-Å-thick Ni film, monitored by RHEED during vacuum annealing at 750°C, turned out to be a very slow process, with a time constant on the order of 1 h or more. This justified the use of the samples with Ni overlayers as clean Ni surfaces in the seed layer deposition experiments.

### 1.2.3 Seed Layer Deposition

YSZ and $CeO_2$ seed layers were deposited by laser ablation of stoichiometric ceramic targets on the c(2 × 2)/{100}<100> Ni surface and on the superstructure-free Ni overlayers that had been previously deposited in situ. The films were grown under the same conditions and with the same procedure on both surface structures, while the process was monitored with RHEED. The deposition temperature was 800°C for YSZ and 750°C for $CeO_2$. In the case of YSZ, after an initial ~100-Å-thick layer was deposited in vacuum ($P_{base} = 5 \times 10^{-8}$ Torr), the $O_2$ partial pressure was increased to the value $1 \times 10^{-5}$ Torr, and a final 1200-Å-thick film was grown.

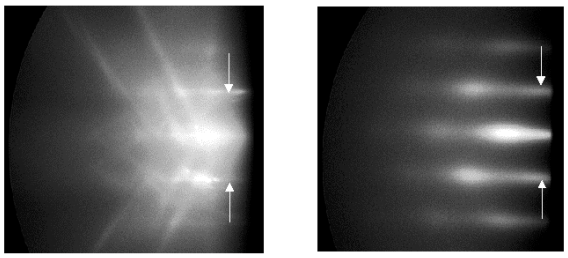

**Fig. 1.19. Comparison of RHEED patterns from a (001) YSZ crystal along <110> (a) and a YSZ film on {100}<100> Ni along the Ni <100> (b).**

The YSZ films grown on the c(2 × 2) surface showed single (002) orientation, with a (111) pole figure indicating the same degree of grain alignment as the substrate. Figure 1.19 shows a comparison between the RHEED pattern of an (001) YSZ single crystal with the electron beam directed along the <110> and the RHEED pattern of a ~ 600-Å-thick YSZ film on Ni with the beam along the Ni <100>. The equal spacing of the RHEED streaks in the two patterns indicates that the YSZ film on Ni is (002)-oriented with a 45° in-plane rotation with respect to the substrate. By contrast, the YSZ films grown on the superstructure-free Ni overlayer showed (111) orientation. The $CeO_2$ seed layers (~200 Å thick) were grown in a background $H_2O$ pressure of $2.5 \times 10^{-5}$ Torr with a ratio $P[H_2O]/P[H_2] = 10^2$. Similarly to the YSZ case, the c(2 × 2) superstructure promoted (200) nucleation, while deposition on the Ni surface with no superstructure resulted in (111) orientation for the $CeO_2$ film.

The quality of the YSZ seed layers on c(2 × 2)/Ni was tested by growing a 0.3-μm-thick YBCO film by the ex situ $BaF_2$ method on some of the samples. A 20-nm-thick $CeO_2$ cap layer enabled compatibility of the precursor layer with the YSZ. The resulting YBCO critical current density was 1.15 MA/cm$^2$ in self-field at 77 K, indicating that a 120-nm-thick YSZ film is a good Ni diffusion barrier and a good buffer layer for coated conductors

Although most of the Ni samples investigated showed levels of S on the surface very comparable to the values reported in Fig. 1.18, in some cases the ratio between the S peak and the Ni peak gave rise to an Auger percentage considerably lower than 25%. For example, long texturing heat treatments at elevated temperatures caused partial evaporation of the surface S, resulting in much weaker c(2 × 2) streaks in RHEED. Figure 1.20 shows a comparison between the (111) ϕ-scans of two $CeO_2$ seed layers deposited on Ni substrates cut from the same tape and annealed at 1100°C for 2 and 15 h, respectively. Both $CeO_2$ films were cube-textured and showed single (002) orientation. However, while the $CeO_2$ film grown on the sample annealed for 2 h replicated the substrate texture (FWHM = 8.2°), the film grown on the sample with weaker superstructure showed a broader grain alignment, with a FWHM of 10.6°.

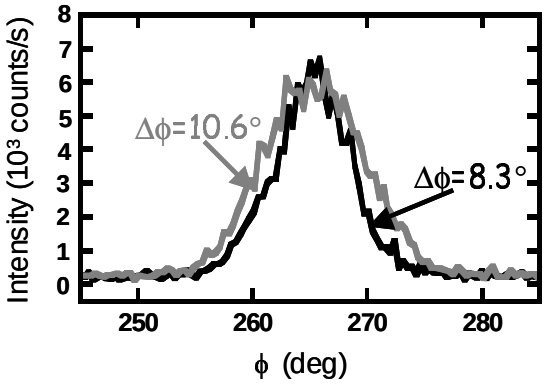


**Fig. 1.20. Phi scans of the (111) reflection of two $CeO_2$ seed layers, one grown on a Ni substrate annealed for 2 h (black line) and the other on a Ni substrate annealed for 15 h (gray line).** The substrates showed a FWHM for the (111) peak of 8.2°.

### 1.2.4 Discussion

We believe that the role played by the S superstructure can be partially explained on the basis of structural and chemical considerations. The structure of chemisorbed layers of O and S on (001) Ni has been largely investigated in the past few decades by many groups. Sulfur and oxygen are known to be bound in the fourfold Ni hollow and to reside about 1 Å above the outer Ni plane. Figure 1.21 shows a schematic of a c(2 × 2) surface structure on (001) Ni and a $CeO_2$ unit cell. The S layer behaves like a template that well matches and mimics the arrangement of the O atoms-in particular, (001) oxygen sublattice planes of YSZ or $CeO_2$. Sulfur belongs to the VI group and is chemically very similar to oxygen, often exhibiting the same electronic valence. Therefore, it is plausible that during the deposition of the seed layer the cations easily bond to the S atoms already present on the substrate surface. We propose that during deposition, the unoccupied Ni hollows of the c(2 × 2)-S structure are filled with O, and the nucleation of $CeO_2$ (or YSZ) takes place starting from the S+O overlayer and continues in the sequence Ce-plane (Y+Zr-plane), O-plane, and so on, giving rise to the (001) epitaxial growth of the film, which otherwise would not take place.

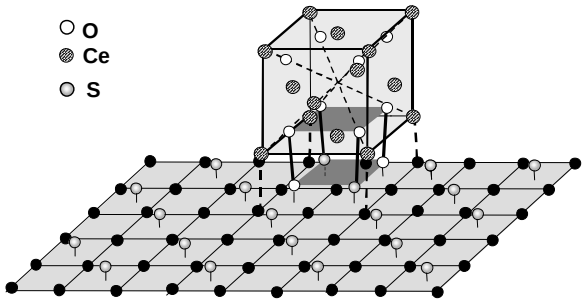


**Fig. 1.21. Proposed c(2 × 2) mediated epitaxial growth of $CeO_2$ on (001) Ni surface.** The superstructure adatoms become constituents of the basal oxygen sublattice of $CeO_2$.

This study indicates that the growth of other oxide seed layers on biaxially textured Ni is likely to involve nucleation on surfaces characterized by stable c(2 × 2) sulfur superstructures. Remaining issues of importance for coated conductor development include the reproducibility and control of the superstructure on {100}<100> Ni and its generality with respect to other deposition methods (including solution-based approaches). Another important aspect involves the study of chemisorption-induced surface reconstruction of other metals or alloys that are potentially advantageous and more suitable for a coated conductor technology. Research to address these issues is ongoing.

## 1.3 A SULFUR TEMPLATE FOR BUFFER LAYERS ON LENGTHS OF TEXTURED Ni TAPES

*M. Kowalewski, F. A. List, L. Heatherly, B. Kang, N. Rutter, D. F. Lee, and D. M. Kroeger*

Growth of high-quality epitaxial oxide buffer layers on biaxially textured Ni or Ni-base alloy substrates is necessary to obtain high-critical-current coated conductors. Although procedures have been developed to grow high-quality epitaxial $CeO_2$ layers on lengths of biaxially textured Ni tape, results have proven difficult to reproduce. The process conditions for obtaining good $CeO_2$ appear to vary with the Ni source and the Ni annealing conditions. The goal of this effort is to develop a more robust process for growing buffer layers on tape lengths, using an understanding of the role S can play for epitaxial growth of $CeO_2$ on Ni.

The role of sulfur—specifically, an ordered c(2 × 2) sulfur overlayer—in the growth of epitaxial $CeO_2$ on short lengths of biaxially textured Ni has been recently studied and is presented in Sect. 1.2 of this report. To test whether these results can be used to reliably grow $CeO_2$ on long moving lengths of Ni, a reel-to-reel vacuum chamber used to anneal lengths of Ni tape and deposit $CeO_2$ was equipped with an in-line Auger electron energy analyzer. AES provides a means of monitoring the chemical composition of the first few atomic layers of the free surface of the tape.

Figure 1.22 shows the vacuum chamber modification schematically. Sulfur was introduced into the vacuum chamber in the form of either pure $H_2S$ or mixtures of $H_2/H_2S$ via a precision variable leak valve. The AES results were calibrated using the Auger S (152 eV) and Ni (848 eV) peak intensities obtained for a biaxially textured Ni(001) surface with a c(2 × 2) sulfur overlayer.

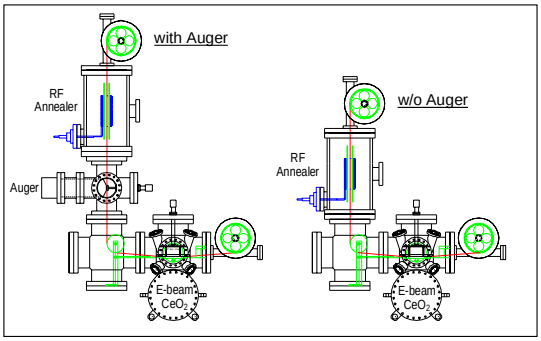


**Fig. 1.22. Schematic of vacuum chamber modification.**

An ~6-m length of unannealed Ni tape was first cleaned ultrasonically and loaded into the vacuum chamber. During the run, the tape traveled through the vacuum system at a speed of 1 m/h, first passing through the rf annealer, then by the Auger analyzer, and finally over the $CeO_2$ deposition source (see Fig. 1.22). The composition of the surface sulfur was continuously monitored with AES. The $H_2S$ partial pressure was continuously monitored with a mass spectrometer and was varied several times during the course of the run to achieve different levels of surface sulfur. Following the run, the tape was removed from the vacuum chamber and was characterized with XRD over its entire length.

Figure 1.23 shows AES and XRD data obtained as a function of position for the first ~4.5 m of the tape. Correlation is apparent between surface sulfur concentration and both out-of-plane and in-plane $CeO_2$ X-ray intensities; higher S concentrations result in better $CeO_2$ epitaxy.

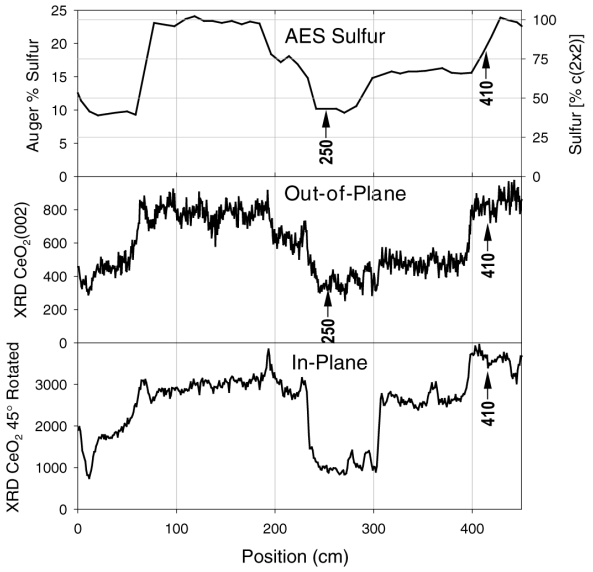


**Fig. 1.23. AES and XRD data obtained as a function of position for the first ~4.5 m of the tape.**

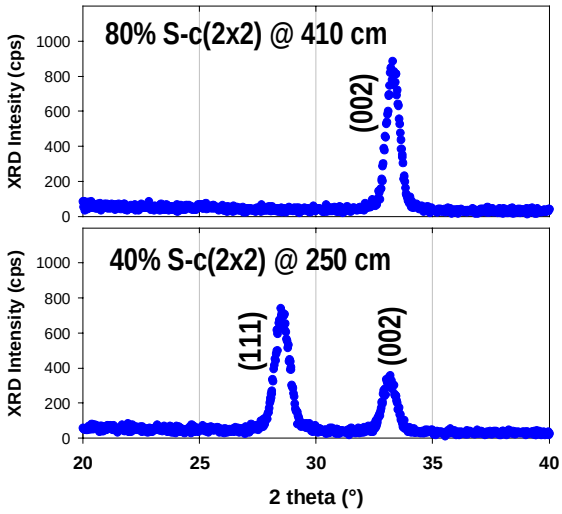


**Fig. 1.24. X-ray θ-2θ scans for tape positions with different S coverage.**

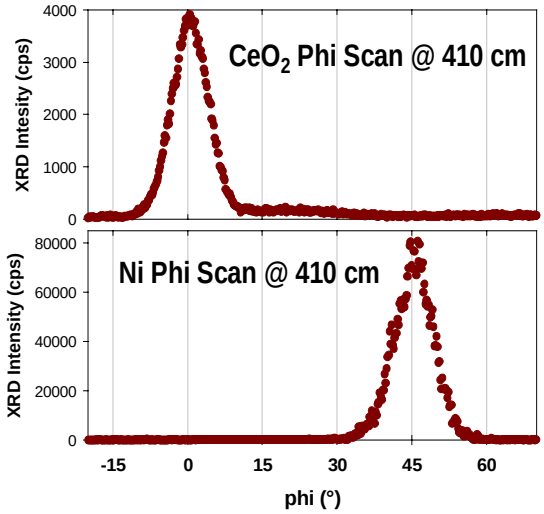


**Fig. 1.25. X-ray $CeO_2$(111) and Ni(111) ϕ-scans for a tape position with 80% c(2 × 2) S.**

Figure 1.24 compares the out-of-plane θ-2θ X-ray scans obtained for a position on the tape with 80% c(2 × 2) S coverage to that for a position on the tape with only 40% c(2 × 2) S coverage. A single $CeO_2$(002) out-of-plane orientation is observed for 80% c(2 × 2) S, whereas both a $CeO_2$(002) and $CeO_2$(111) out-of-plane orientation are obtained for 40% c(2 × 2) S. X-ray ϕ-scans for the tape with 80% c(2 × 2) S show a single in-plane orientation for the $CeO_2$, which is rotated 45° with respect to the underlying Ni (Fig. 1.25).

The quality of epitaxy of the $CeO_2$ on Ni can be judged from X-ray determinations of Δω and Δϕ. Figure 1.26 shows Δω and Δϕ for $CeO_2$ and Ni as a function of position. Lower values of Δω and Δϕ indicate smaller distributions of crystalline orientation and, thus, better epitaxial quality. Better $CeO_2$ epitaxy is found for tape positions with higher S coverage.

To determine whether a correlation exits between S coverage and the $J_c$ of the complete coated conductor, four 3-cm sections were cut from the ~4.5-m tape. For each section, the buffer layer structure was completed using standard rf sputtering techniques, and YBCO was deposited by PLD to a thickness of 2000 Å. The $J_c$ results for the four sections are shown in Fig. 1.27. For the range of sulfur spanned [~40 to 80% c(2 × 2)], $J_c$ appears to increase linearly with S coverage.

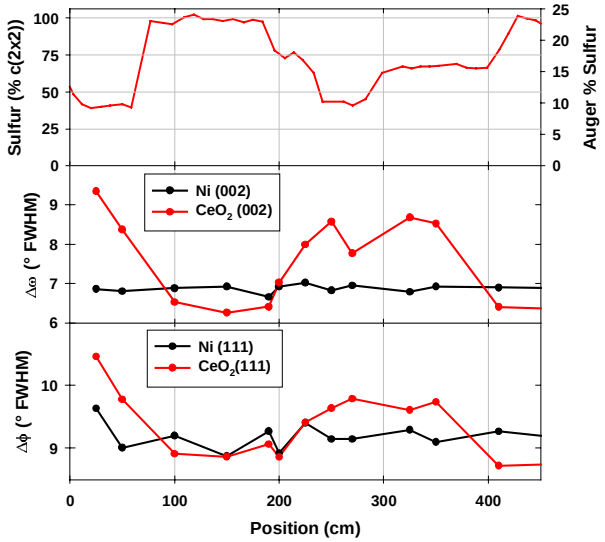


**Fig. 1.26. X-ray $\Delta\omega$ and $\Delta\phi$ for $CeO_2$ and Ni as a function of position.**

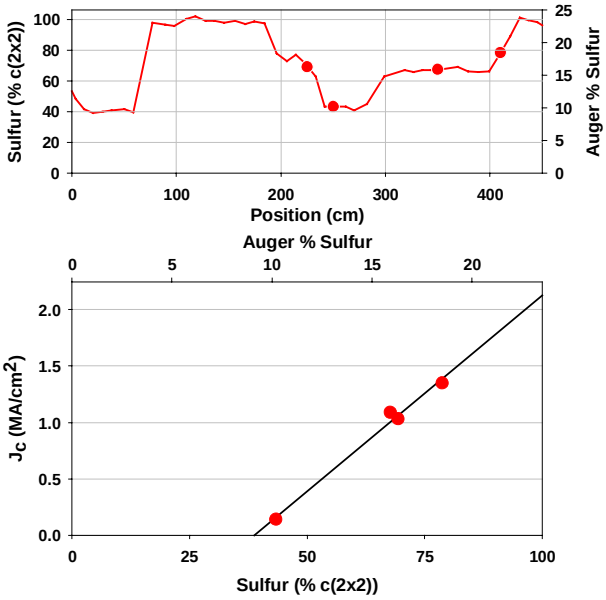


**Fig. 1.27. $J_c$ for PLD YBCO on four sections of tape.**

To demonstrate that high-quality $CeO_2$ can be prepared on lengths of sulfurized Ni, a 10-m length of Ni tape was annealed, sulfurized with 100% c(2 × 2) S, and deposited with $CeO_2$ in a single pass through the vacuum system. Figure 1.28 shows the out-of-plane and in-plane $CeO_2$ X-ray intensities as a function of position. The $CeO_2$ epitaxy appears to be excellent—greater than 99% (002) out-of-plane and greater than 99% rotated 45° in-plane. Whether this tape can support high $J_c$ remains to be determined. Such a determination requires completion of the buffer layer structure and deposition of YBCO over the entire 10-m length.

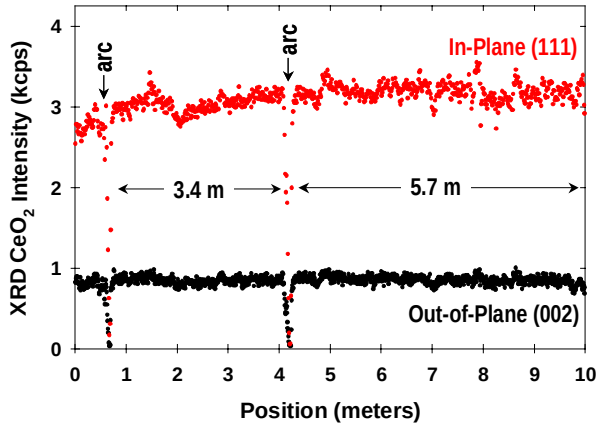


**Fig. 1.28. Out-of-plane and in-plane $CeO_2$ X-ray intensities as a function of position for a 10-m Ni tape.** Arcing observed during $CeO_2$ deposition is indicated by arrows.

In summary, an Auger electron analyzer has been added to an existing reel-to-reel vacuum system used for tape annealing and $CeO_2$ deposition. Sulfur, adsorbed on an annealed Ni tape surface, appears to improve the epitaxial quality of subsequently deposited $CeO_2$. Both the quality of $CeO_2$ epitaxy and the $J_c$ of PLD YBCO seem to increase with increasing S coverage. Good-quality $CeO_2$ has been grown on a 10-m length of sulfurized Ni tape.

## 1.4 PROGRESS IN REEL-TO-REEL EX SITU $BaF_2$ CONVERSION OF LONG-LENGTH YBCO COATED CONDUCTORS

*D. F. Lee, K. J. Leonard, M. M. Kowalewski, T. Aytug, M. Paranthaman, S. Sathyamurthy, J. Yoo, E. D. Specht, D. M. Kroeger, P. M. Martin, A. Goyal, C. Cantoni, and D. K. Christen (ORNL); D. O'Neill and W. B. Robbins (3M Company)*

### 1.4.1 Introduction

Unlike traditional in situ techniques such as PLD, the ex situ conversion of YBCO separates the precursor deposition step (i.e., compositional control) from the YBCO epitaxial growth process. This separation may enable further simplification in processing procedures, such as nonvacuum deposition of precursor film or batch conversion of YBCO, and makes ex situ processing an attractive alternative. In order to study the feasibility of this method, we have engaged in the continuous conversion of $BaF_2$ precursor on RABiTS™ using our reel-to-reel conversion chamber. As previously reported, our initial results on 1-m-long samples showed sectional $J_c$s as high as 750 kA/cm$^2$. Unfortunately, various flaws along the samples combined to limit the overall $J_c$ level and led to high $J_c$ nonuniformity.

Careful examination of the samples throughout the fabrication steps has revealed several factors that contributed to the low $J_c$s. Among these are

- RABiTS™ texture, which mostly limits the overall $J_c$ value;
- precursor nonstoichiometry, which affects both the end-to-end $J_c$ and $J_c$ uniformity;
- sample-gas orientation, which contributes to $J_c$ nonuniformity; and
- dimensional flaws (i.e., kinks), which also contribute to $J_c$ nonuniformity.

We are currently implementing improvements and modifications to circumvent these issues.

### 1.4.2 $J_c$-Limiting Flaws

#### 1.4.2.1 RABiTS™ Texture

Since the attainment of quasi-single-crystal-like YBCO coated conductors largely depends on the texture and quality of the RABiTS™, uniform and consistent texture in both the metallic substrate and the deposited buffer layers is exceedingly important. It has long been known that the degree of texture in the metallic substrate depends on the rolling schedule as well as on the annealing condition of the metal itself. In order to optimize these parameters, we have recently acquired a rolling mill so that systematic study can be performed on specific metal stocks supplied by various vendors.

Once a highly textured metallic substrate is obtained, buffer layers have to be epitaxially deposited onto the metal. We have recently found that a c(2 × 2) structure exists on the surface of the metal as a consequence of S diffusion during metal annealing. Experimental evidence suggests that it is this c(2 × 2) structure that facilitates the epitaxial deposition of seed buffer onto the substrate. Thus, the annealing parameters employed during metal annealing will not only determine the degree of texture but will also influence the extent and amount of coverage of this important c(2 × 2) structure. Since S content in various metal stocks will differ, it will be advantageous to achieve this c(2 × 2) surface structure by means other than S diffusion. Thus, we have begun experiments with metal annealing in the presence of $H_2S$. Results so far have indicated that a complete c(2 × 2) structure can be achieved through this modification, which may provide a way to obtain uniform and consistent buffer epitaxy in lengths.

### 1.4.2.2 Precursor Stoichiometry

Another factor that limits the sectional $J_c$, and therefore $J_c$ uniformity and end-to-end value in lengths, is precursor stoichiometry during deposition. At ORNL, $BaF_2$ precursor deposition is performed in a three-gun reel-to-reel e-beam evaporation system. This system consists of a CVS-15 15-kW electron-beam power supply with three electron-beam guns operating at a voltage of 8 kV. Source materials in the form of Y metal, Cu metal, and $BaF_2$ crystals are situated in three separate pockets. Precursor deposition is carried out in an $H_2O$ partial pressure of $1 \times 10^{-5}$ Torr with a total pressure of less than $6 \times 10^{-5}$ Torr, with monitoring performed by an SRS 100RGA mass spectrometer. It is critical to keep the $H_2O$ partial pressure constant since variations will affect the deposition rates of Y and Cu and the oxygen content of the precursor film. At a tape traveling speed of 0.8 m/h, the precursor film was continuously deposited at a rate of 10 Å/s, with the deposition rates of Y, $BaF_2$, and Cu individually controlled by quartz crystal monitors.

Precursor film deposited in such a fashion typically has a mean thickness of approximately 3000 Å, with a standard deviation of ±2.5% over the entire meter length. Rutherford Backscattering Spectroscopy (RBS) measurements at 10-cm increments showed that the "long-range" stoichiometry of the precursor is quite uniform, with a typical Y/Ba/Cu composition of roughly 1.05/2.1/3.0 and a standard deviation of less than ±2%. While the overall chemical composition of the precursor is excellent, occasional fluctuations and/or discharges in an individual electron gun have resulted in localized off-stoichiometry regions a few millimeters wide. These "short-range" off-stoichiometry regions are clearly visible in fully converted conductors as line features that extend transversely across the width of the tape (see Fig. 1.29). Transport current density measurements performed for these regions showed a one-to-one correspondence between these line defects and low $J_c$ (Figs. 1.29 and 1.30). Clearly, occurrence of these off-stoichiometry regions has to be eliminated if the YBCO conductor is to carry high $J_c$ across long lengths.

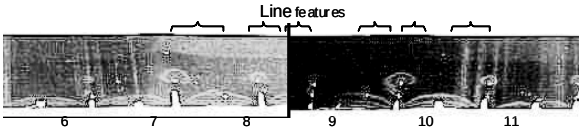


**Fig. 1.29. Optical image of the YBCO tape containing low-$J_c$ sections.** Linear features can be seen running across the entire width of the tape.

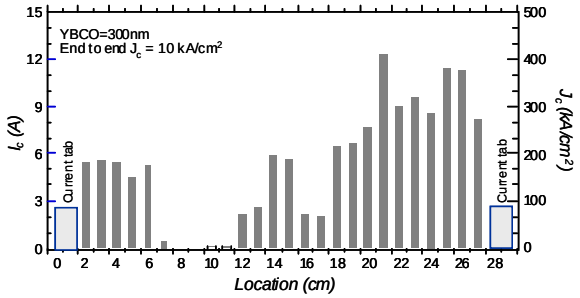


**Fig. 1.30. Sectional $J_c$s of a 30-cm-long YBCO (e-beam precursor) / $CeO_2$ (rf sputtered) / YSZ (rf sputtered) / $CeO_2$ (reactive sputtered) / Pd (reactive sputtered) / Ni sample at 77 K and self-field.** Low $J_c$ values are located between 7- and 11-cm sections in the YBCO film shown in Fig. 1.29.

Careful examination has shown that these off-stoichiometric line defects originated during precursor deposition and can be attributed to two types of events that cause sudden changes in flux rates: arcing events in the high-voltage supply of the guns or non-arcing events related to the thermal transfer through the crucible liner.

In the case of high-voltage arcing, particles built up in the deposition chamber can detach and fall within certain sensitive areas of the voltage supply to the guns. A critical area in the configuration of our system is the high-tension feed-through across the chamber wall. Loose particles that fall either during deposition or during chamber cleaning can bridge the distance over the ceramic insulation, thereby shorting the high-tension lead to the chamber wall. When this happens, high-voltage arcing will occur.

Moreover, arcing of one gun will generally interrupt the functioning of the other guns because, in our system, all of them are connected to the same power supply. This interruption, in turn, produces variations in deposition rates; the amount of variation depends on the material being deposited. For example, deposition of $BaF_2$ is accomplished by radiant heating of the target crystal by a tungsten cap over the crucible, which is heated by the e-gun. An instantaneous drop in voltage of the e-gun heating the tungsten cap has little effect because of its thermal mass. On the other hand, the Y-metal target of our system is only melted in the path of the e-beam. Therefore, a sudden change in the gun's performance will create noticeable changes in the flux rate. In some cases, short-circuiting of a high-tension lead is continuous and requires system shutdown to enable removal of the short.

The second type of fluctuation originates from nonuniformities in the conductive heat transfer away from the crucible liner. Flaws such as scratches and pits on the surface of the crucible liner can produce variations in heat transfer from the target, especially when dealing with melted targets. For example, a sharp spike in the deposition rate of Cu, either as an increased flux rate to a value far above the set rate or as a decreased flux to near zero, has been observed when using older crucible liners of poor surface quality. While a spike in deposition rate may recover within a couple of seconds on its own, the response of the deposition controller to compensate may further exacerbate the problem. This occurs because on registering a large change in flux rate, the controllers respond immediately by either cutting or increasing the power to compensate for the initial rate change. This further compounds the problem of stabilizing the flux rate to the set value over time, thereby creating variations in precursor composition and thickness over as much as a few centimeters of the tape. In addition, variations in flux rate arising from Cu can induce instabilities in the rates of both Y and $BaF_2$ by causing changes in the effective vapor pressures within the chamber. The adverse influence of precursor nonstoichiometry and nonuniformity on $J_c$ points toward the need to improve the operational stability of our precursor deposition unit. Work is under way to relocate the high-tension feed-through and to prevent shorting in our system. In addition, replacement of selected e-guns with more stable effusion cells is also being evaluated.

### 1.4.2.3 Sample-gas orientation

Another factor that is believed to affect the extent of ex situ YBCO conversion and hence, $J_c$, is the orientation relationship between sample surface and direction of gas flow. In fully converted YBCO tapes, a grayish region is frequently found at the gas outlet edge of the conductor, a typical example of which is shown in Fig. 1.31. When present, this feature is typically seen along the entire length of the tape, although its width varies from location to location. XRD analyses revealed that the grayish region is richer in $BaF_2$ than the gas inlet edge or the center of the tape. This variation in $BaF_2$ content indicates the occurrence of nonuniform oxifluoride decomposition. A possible contributing factor to the decomposition inhomogeneity even across this reduced-length scale may arise from the upward curvature of the sample. Since a typical one-sided coated conductor is an antisymmetric composite, sample curvature across the tape width will result, owing to the different thermal expansions and stress states of the YBCO, the buffer(s), and the metallic substrate. The sample curvature can be quite pronounced, especially when a soft substrate such as annealed Ni is used.

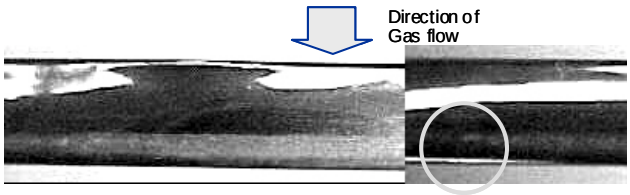


**Fig. 1.31. A grayish region is frequently found at the gas outlet edge of fully converted samples.** The width of this $BaF_2$-rich region varied from location to location but can be seen along the entire length of the tape.

The influence of sample curvature on gas flow profile was investigated by computational fluid dynamics simulations. Simulated results revealed that gas velocities at the leading and trailing edges of a curved tape are lower than that of the middle portion, owing to the increased local clearance between sample surface and chamber wall. The $HF/H_2O$ concentration ratio at the trailing edge of such a curved sample will likely be higher, thereby resulting in slower oxifluoride decomposition/YBCO conversion, such as that seen in Fig. 1.31. The situation worsens when the sample is tilted away from the gas inlet, which may happen during actual reel-to-reel conversion. In this case, calculated gas velocity at the trailing edge of the tape is further decreased, leading to greater tendency toward incomplete decomposition/conversion. This can account for the varying width of the incompletely converted region along the length of the tape. An effort is under way to redesign the flow-modules such that (1) gas injection is set at a slight angle with respect to the sample surface and (2) gas injection directions alternate from module to module. These modifications should ensure that part of the tape will always be in correct orientation with the gas flow regardless of sample tilting.

#### 1.4.2.4 Dimensional flaws

Apart from the incompletely reacted region seen at the downstream edge of the entire tape, there are other more striking examples of sample-gas orientational effects. These regions contain incompletely converted precursor and are typically found at locations with dimensional flaws (i.e., kinks at the edge of the tape.) Figure 1.32 shows a section of a meter-long tape containing an upward kink. The origin of kinks such as this has been traced to the tight tolerance of our reels being used in the fabrication of RABiTS™. We have found that if the reel alignment is not perfect, the Ni substrate is not straight, or there is variation in the width of the substrate, the substrate will be in contact with the reel wall during sample windup. During payout, the sample will remain in contact with the reel wall at those points until sufficient force is applied to overcome the frictional force and the sample breaks free from the reel. It is this action that results in kinks in the soft Ni substrate. This type of flaw not only tilts the sample away from the gas inlet but also acts as an obstacle where the gas is channeled to either side, resulting in incompletely reacted material that fans out from the flaw. Incompletely converted regions such as that shown in Fig. 1.32 have been found to be significant contributors to $J_c$ nonuniformity in continuously converted YBCO tapes.

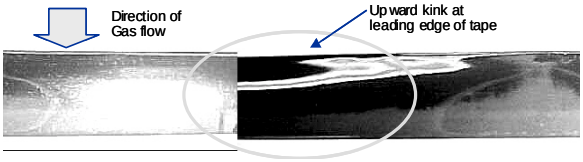


**Fig. 1.32. Section of a meter-long tape that contains an upward kink at the leading edge of the sample.** Flowing gas was channeled around such a flaw, leading to incompletely converted material that fans out behind the obstacle.

### 1.4.3 Progress in Long-Length Reel-to-Reel Ex Situ Conversion of YBCO on RABiTS™

While considerable lead time is necessary to implement solutions to the majority of the aforementioned $J_c$-limiting factors, it is a relatively straightforward task to eliminate the dimensional flaws in RABiTS™. By using wider reels and modifying the tape-transfer procedure, it is now possible to routinely obtain RABiTS™ without kinks. Although these flaws may seem trivial at first glance, their effect on $J_c$ uniformity has proven to be dramatic. Before the removal of kinks, the standard deviation in sectional $J_c$ was about 23 to 25%. As soon as the kinks were eliminated, the standard deviation dropped to a much lower value, about 10 to 13%.

An example of such an improvement is shown in Fig. 1.33, where a 1-cm-wide, 60-cm-long precursor / $CeO_2$ (rf sputtered) / YSZ (rf sputtered) / $CeO_2$ (e-beam) / Ni sample was continuously converted in our seven-module reel-to-reel chamber at a tape traveling speed of 0.65 m/h, conversion temperature of 740°C, oxygen partial pressure of 130 mTorr, $H_2O$ partial pressure of 70 Torr, and gas flow rate of 5.5 L/min. With no significant discharge or fluctuation during precursor deposition, the end-to-end $J_c$ of the tape was found to be a respectable 400 kA/cm$^2$. In addition, sectional $J_c$ measurements were performed and showed that $J_c$ uniformity has improved because of the elimination of kinks, leading to an averaged $J_c$ of 600 kA/cm$^2$ and a reduced standard deviation of 12.5%. These improvements can be compared with those obtained in our previous attempt at long length conversion (end-to-end $J_c$ of 100 kA/cm$^2$ and a standard deviation of 25%).

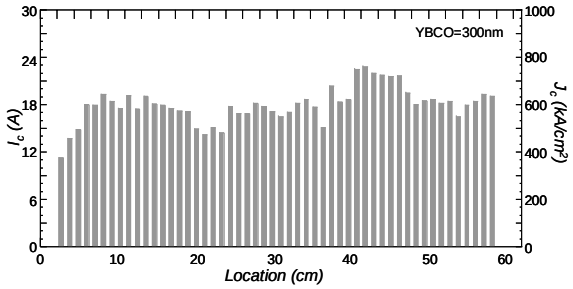


**Fig. 1.33. Sectional $J_c$s of a 60-cm-long YBCO / $CeO_2$ (rf sputtered) / YSZ (rf sputtered) / $CeO_2$ (e-beam) / Ni sample at 77 K and self-field.**

We then proceeded to examine the influences of various processing parameters on precursor conversion. Based on the results from our single-module transverse-flow chamber, effects of flow rate and wet conversion time were investigated. A 1-cm-wide, 5-m-long precursor / $CeO_2$ (rf sputtered) / YSZ (rf sputtered) / $CeO_2$ (e-beam) / Ni sample was prepared in an all-moving manner. Individual samples, 0.6 to 1 m in length, were cut from this stock to ensure sample-to-sample uniformity. Traveling speed of the tapes was varied to provide a targeted wet conversion time between 60 and 180 min. Gas flow rate was set at 5.5 L/min, except for one sample, which was converted at a gas flow rate of 5 L/min. The remaining parameters were fixed as follows: conversion temperature of 740°C, oxygen partial pressure of 130 mTorr and $H_2O$ partial pressure of 70 Torr. Sectional transport $J_c$ measurements were performed, and the averaged $J_c$ with associated standard deviation are shown in Fig. 1.34 as a function of wet conversion time. Also included in the figure is the short-sample $J_c$ of PLD YBCO on the same RABiTS™, which represents the upper limit of current capacity in this material. It can be seen from the figure that as conversion time increases, the $J_c$ reaches a maximum and then decreases on further processing. Thus, the performance-based optimal conversion time appears to be roughly 120 min for this precursor under the prescribed set of parameters. Moreover, the maximum $J_c$ is slightly below that of the PLD YBCO, indicating that there is still headroom for improvement. Also, $J_c$ is found to increase with gas flow within the range of flow rates tested. This behavior suggests that the HF:$H_2O$ ratio is still significant even at this high flow rate and that the efficiency of HF removal may be an issue.

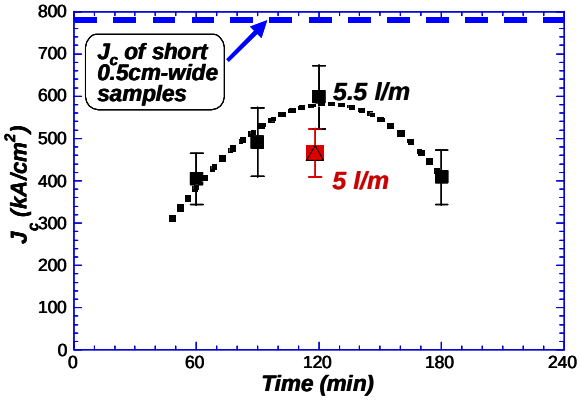


**Fig. 1.34. Averaged $J_c$s of YBCO / $CeO_2$ (rf sputtered) / YSZ (rf sputtered) / $CeO_2$ (e-beam) / Ni sample at 77 K and self-field.** The tapes were converted in various lengths of time and at two flow rates.

In order to explore possible variations in conversion behavior of samples from different sources, we obtained a 1.27-cm-wide, 5-m-long precursor / $CeO_2$ (reactive sputtered) / YSZ (reactive sputtered) /

$CeO_2$ (reactive sputtered) / Pd (reactive sputtered) / Ni sample prepared solely by 3M company in an all-moving manner. Again, individual samples measuring 0.6 m to 1 m in length were cut from this stock to ensure sample-to-sample uniformity. Traveling speed of the tapes was varied to provide targeted wet conversion times between 90 and 150 min, and gas flow rate was varied between 4.2 and 5.5 L/min. All the remaining parameters were fixed and identical to that of the all-ORNL sample shown in Fig. 1.34. Figure 1.35 shows the sectional $J_c$s of one such meter-long tape converted for 120 min at a flow rate of 5.5 L/min. The end-to-end $J_c$ of this tape is 380 kA/cm$^2$, with an averaged $J_c$ of 395 kA/cm$^2$ and a standard deviation of 10%. Variation in averaged $J_c$ and associated standard deviation of all the 3M tapes and wet conversion time is shown in Fig. 1.36. It can be seen from this figure that the general characteristic of $J_c$s increasing with conversion time reaching a maximum, and then decreasing, remains valid for this set of samples. However, at a flow rate of 5.5 L/min, the performance-based optimum conversion time appears to be 90 min or less for the 3M tapes instead of the value of 120 min for the all-ORNL tapes. In addition, although $J_c$ initially increases with flow-rate for the all-3M tapes, the enhancement appears to level off between 5 and 5.5 L/min, suggesting that a further increase in flow rate may no longer affect the HF:$H_2O$ ratio. The lower overall $J_c$s of the all-3M tapes may be explained by the slightly broader in-plane and out-of-plane textures of the substrate; however, the different optimum conversion conditions suggest that there are some subtle differences in the precursor and/or the substrate, which may be exploited to improve the conversion efficiency of YBCO.

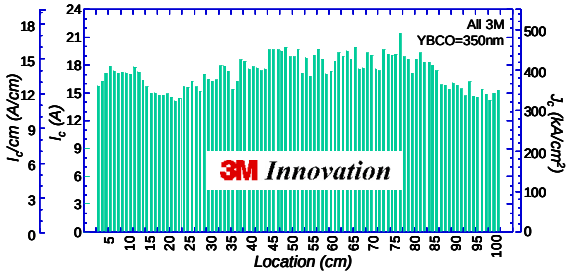


**Fig. 1.35. Sectional $J_c$s of a 1-m-long all-3M YBCO / $CeO_2$ (reactive sputtered) / YSZ (reactive sputtered) / $CeO_2$ (reactive sputtered) / Pd (reactive sputtered) / Ni sample at 77 K and self-field.**

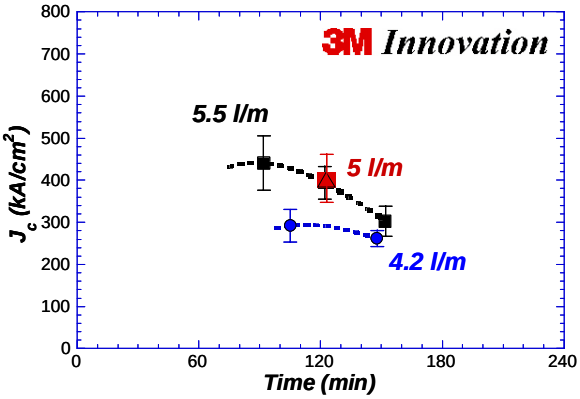


**Fig. 1.36. Averaged $J_c$s of all-3M YBCO / $CeO_2$ (reactive sputtered) / YSZ (reactive sputtered) / $CeO_2$ (reactive sputtered) / Pd (reactive sputtered) / Ni sample at 77 K and self-field.** The tapes were converted in various lengths of time and flow rates.

Further improvement in overall sample performance is also being investigated by utilizing a dip-coated $Gd_2O_3$ seed layer instead of the e-beamed $CeO_2$ material. By annealing the Ni substrate and recrystalizing the sol-gel $Gd_2O_3$ seed layer at higher temperatures, both the out-of-plane and in-plane textures of a 1-m-long RABiTS™ have been improved to FWHM of 11.2 and 9.4°, respectively. Unfortunately, moderate to severe discharges occurred during precursor deposition, forcing the precursor deposition run to be terminated after 80 cm. This 80-cm-long precursor / $CeO_2$ (rf sputtered) / YSZ (rf sputtered) / $Gd_2O_3$ (dip-coated) / Ni sample was continuously converted in the reel-to-reel chamber at a tape traveling speed of 0.65 m/h, a conversion temperature of 740°C, oxygen partial pressure of 130 mTorr, $H_2O$ partial pressure of 70 Torr, and a gas flow rate of 5.5 L/min. Even with areas of nonstoichiometry associated with the discharges, the end-to-end $J_c$ of this sample was found to be 625 kA/cm$^2$. Sectional $J_c$ measurements are shown in Fig. 1.37, where the asterisks represent locations of precursor discharges with associated visible line features. It can be seen from Fig. 1.37 that despite the

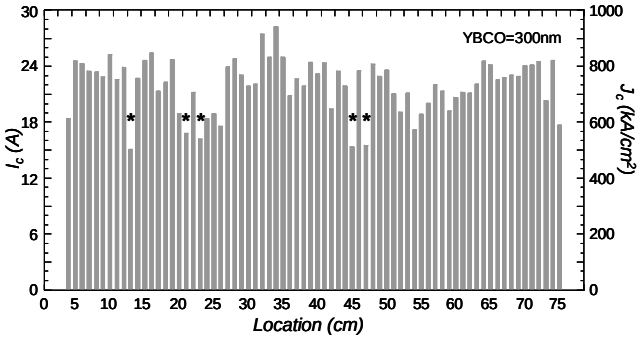


**Fig. 1.37. Sectional $J_c$s of the 80-cm-long YBCO / $CeO_2$ (rf sputtered) / YSZ (rf sputtered) / $Gd_2O_3$ (dip-coated) / Ni sample at 77 K and self-field.** The asterisks (*) denote locations where moderate discharges and faint line-features are visible.

nonstoichiometric sections, a $J_c$ value as high as 950 kA/cm$^2$ has been obtained on this sample owing to the improved RABiTS™ texture. Also, the tape possesses a high averaged $J_c$ of 750 kA/cm$^2$ with a low standard deviation of 10.5%. Results obtained in this work have provided valuable insights into the ex situ conversion process. Efforts are now under way to investigate the conversion of micron-thick YBCO precursors and to improve the conversion process through parameter optimization and equipment modification.

## 1.5 Ni-Cr TEXTURED SUBSTRATES WITH REDUCED FERROMAGNETISM FOR COATED CONDUCTOR APPLICATIONS

*J. R. Thompson, A. Goyal, D. K. Christen, and D. M. Kroeger*

### 1.5.1 Experimental Aspects

A series of alloys was prepared by vacuum melting methods, using 99.99% purity starting elements. We investigated $Ni_{1-x}Cr_x$ materials with nominal compositions of $x$ = 0, 7, 9, 11, and 13 at. % Cr. Details of composition, obtained by ICP analysis, are given in Table 1.1. The materials were biaxially textured by rolling deformation followed by annealing at 1050°C for 2 h in vacuum with an oxygen partial pressure $<10^{-7}$ Torr. For magnetization measurements, the sheets of thickness 0.13 mm were cut into 5 × 5 mm pieces. Generally, a stack of three to five pieces was mounted in a thin plastic tube for magnetic measurements with the magnetic field $H$ applied parallel to the plane of the sheets, to minimize demagnetizing effects. In an additional experiment to assess the magnitude of energy loss caused by ferromagnetic hysteresis after a representative amount of work-hardening, a foil of $Ni_{93}Cr_7$ was controllably deformed. The foil was wrapped around a 9-mm mandrel, flattened, reverse-wrapped, and again flattened. It was studied with field $H$ applied either parallel to or perpendicular to the plane of the foil.

**Table 1.1. Magnetic properties of Ni-Cr Alloys**

| Nominal composition (%) | Cr $x$ (at. %) | $(d[M/H]/dT)_{max}$ | $T_c$ (K) | $\theta_p$ (K) | $M_{sat}$ (G-cm$^3$/g) |
|---|---|---|---|---|---|
| Pure Ni | 0 | | 627 | | 57.5 |
| Cr-7 | 7.2 | 245 | 248 | ~260 | 23.1 |
| Cr-9 | 9.2 | 120 | 115 | 155 | 12.6 |
| Cr-11 | 11.1 | 17 | 20 | 37 | 4 |
| Cr-13 | 13.2 | — | <10 | — | 0.4 |

The magnetic studies were conducted in a superconducting quantum interference device (SQUID)-based magnetometer at temperatures $T$ = 5 to 300 K, in fields $H$ up to 65 kOe. We measured both the isothermal mass magnetization $M(H)$ at various temperatures and the "susceptibility" $M/H$ vs $T$ in fixed field, normally with $H$ = 1 kOe. Dimensionally, the mass magnetization $M$ = (magnetic moment)/(mass of alloy) has units of emu/gram = G-cm$^3$/g. A Philips model XRG3100 diffractometer with Cu $K_\alpha$ radiation was used to record powder diffraction patterns. A Picker four-circle diffractometer was used to determine the texture of the films by omega and phi scans. Pole figures were collected to determine the percentage of cube texture.

### 1.5.2 Magnetic Properties of Textured NiCr Alloys

Figure 1.38 provides an overview of the magnetic properties of the $Ni_{1-x}Cr_x$ alloys. It shows the temperature dependence of the mass magnetization $M(T)$, measured in an applied magnetic field $H$ = 1 kOe. Qualitatively, it is evident that $M$ decreases quickly with the addition of Cr. Also, the Curie temperature, $T_c$, noted on the figure, steadily diminishes. The $T_c$ values were obtained using the relation that the spontaneous magnetization $M \propto (T_c - T)^\beta$ with $\beta = 1/3$.

Figure 1.39 illustrates this dependence by plotting $M^3$ vs $T$, wherein a linear extrapolation to $M^3 = 0$ yields values for $T_c$. In this process, we ignore data very close to $T_c$, where $M$ is influenced by the presence of the applied field. The power law dependence describes the data rather well for a substantial temperature range below $T_c$. Results for the Curie temperature are shown in Fig. 1.38 and are listed in Table 1.1 for all alloys.

For coated-conductor applications, one anticipates that the materials will be employed in the presence of large magnetic fields and for generating such fields. Thus it is useful to examine the field-dependent magnetization, which is shown in Fig. 1.40 at representative temperatures of 40 and 77 K. At these temperatures, it is evident from the "square" response of the 9 and 11 at. % Cr alloys that they are ferromagnetic. In contrast, the alloys with higher Cr content are paramagnetic and have significantly lower magnetization. From similar studies at 5 K, we obtained the saturation magnetization ($M_{sat}$) values listed in Table 1.1. Included in Fig. 1.40 are data for annealed Type 304 stainless steel, a common construction material in cryogenic applications; a comparison shows that the magnetization of the Ni-11 at. % Cr alloy is comparable with that of 304 SS; the 13 at. % Cr alloy is even lower.

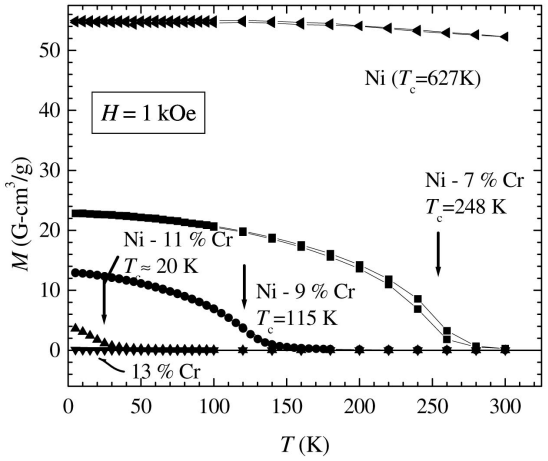


**Fig. 1.38. The mass magnetization of $Ni_{1-x}Cr_x$ alloys vs temperature, measured in an applied field $H$ = 1 kOe applied parallel to the plane of the foils.** Nominal Cr concentration $x$ is given in atomic percent.

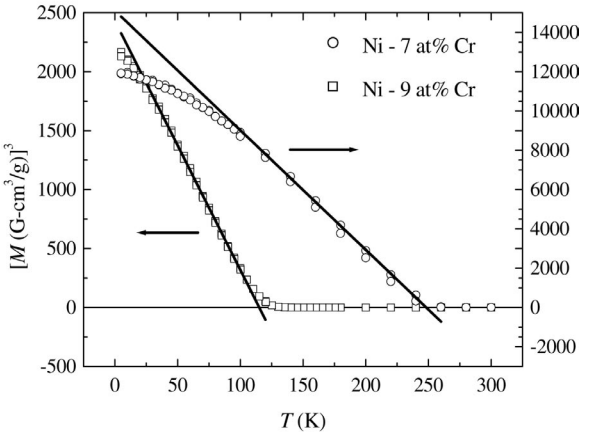


**Fig. 1.39. A plot of $M^3$ vs temperature $T$.** Straight lines show the extrapolation to $M$ = 0 used to define the Curie temperature $T_c$.

Let us now consider the paramagnetic state above $T_c$. For an applied field that is not too large (here $H$ = 1 kOe), the $M/H$ ratio closely approximates the initial differential susceptibility $\chi_{mass} = dM/dH$. Thus we analyze the data using a Curie-Weiss dependence

$$M / H = C / (T - \theta_\rho) \ , \qquad (1.1)$$

where $C = N_A \mu_B^2 p_{eff}^2 / 3k_B$ is the Curie constant and $\theta_\rho$ is the paramagnetic Weiss temperature. Then we plot the reciprocal $H/M$ vs $T$ in Fig. 1.41, which shows a reasonable description of the data. The resulting values for the Weiss temperatures are shown in Table 1.1. At higher temperatures, some samples deviate from the simple Curie-Weiss relationship; this may be caused by deviations from the overly simple temperature dependence of Eq. (1.1) or the presence of additional paramagnetic contributions; (e.g., the nominally temperature-independent orbital terms not included in this expression). As is frequently the case for ferromagnetic materials, the values for $\theta_\rho$ lie near their respective Curie temperatures but rarely coincide exactly. In Table 1.1, along with the paramagnetic Weiss temperatures ($\theta_\rho$), are values of the temperature at which $d(M/H)/dT$ is largest; these values provide a rough estimate of the Curie temperature, provided that the applied field (here 1 kOe) is not too large.

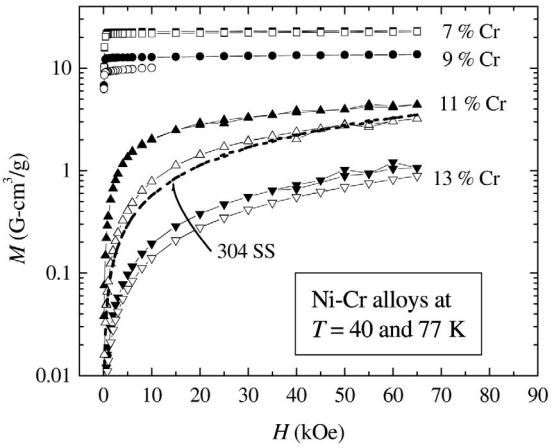


**Fig. 1.40. The field dependence of the magnetization of $Ni_{1-x}Cr_x$ materials at 40 K (closed symbols) and at 77 K (open symbols).** For comparison, the magnetization of Type 304 stainless steel at 77 K is shown as a dotted line.

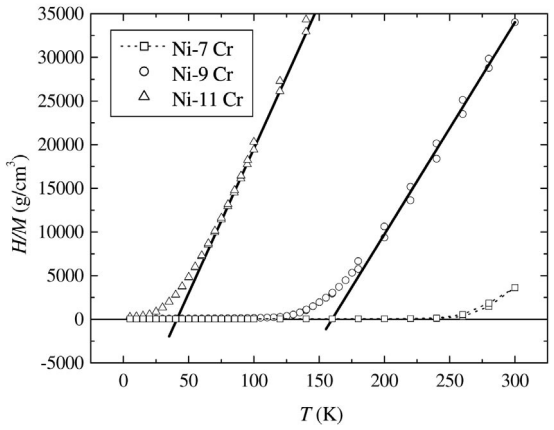


**Fig. 1.41. The inverse "susceptibility" *H/M* vs temperature *T* for three ferromagnetic NiCr alloys.** The straight lines show a simple Curie-Weiss dependence [Eq. (1.1)] for alloys with 9 and 11 at. % Cr.

Some qualitative dependencies on Cr content $x$ are already apparent. More quantitative features are presented in Fig. 1.42. In Fig. 1.42(a) is the Curie temperature $T_c$ that decreases quite linearly with $x$, as shown by the solid line fitted to the present data. A simple linear extrapolation to the axis at $T_c = 0$ intersects at the critical Cr concentration of 11.5 ± 0.4 at. %. This value lies slightly below the critical concentration $x_c$ = 13 at. % Cr deduced previously by Besnus et al.[1] These authors, whose results are included in Fig. 1.42, observed a "tail" in the $T_c(x)$ dependence near $x_c$. Also included are earlier results from the compendium of Bozorth,[2] in which many values were obtained by extrapolating from higher temperatures. The present results for our biaxially textured substrate materials lie close to those from some earlier studies, but significantly below the values reported in Bozorth. Figure 1.42(b) presents the saturation magnetization $M_{sat}$ at $T$ = 5 K. Again a linear decrease with Cr content is observed, as illustrated by the solid line, with an intersection at a Cr concentration of 12.0 ± 0.2 at. %. As in Fig. 1.42(a), the present results lie below the earlier data from Bozorth and agree within experimental error with the data of Besnus et al.

Next we consider the hysteretic energy loss in a deformed ferromagnetic alloy of Ni-7 at. % Cr. For this work, a foil was wrapped around a 9-mm mandrel, flattened, reverse wrapped, then again flattened to

simulate the work hardening that might be encountered in fabricating a superconducting component. The magnetization of the material is shown in Fig. 1.43 with the field applied either parallel to the plane of the foil (steep curves related to a small demagnetizing factor) or parallel to a normal (**n**) to the surface (flatter curve with much stronger demagnetizing effects). In either case, the material is relatively reversible, qualitatively indicating a modest energy loss from magnetic hysteresis. Numerical integration of the loop area gives a hysteretic energy loss per cycle of 160 erg/g with $H \parallel \mathbf{n}$ and 230 erg/g with $H \perp \mathbf{n}$.

This loss is rather slight, compared with other power losses encountered in ac applications. Consider a common figure-of-merit for a coated conductor, the power loss per kiloampere-meter of composite material. The quantity of useful conductor, in units of kA-m, is the product of current $I$ and length $L$, or equivalently $JV_{sc}$ (where $J$ is the operating current density in the superconductor and $V_{sc}$ is its volume). For example, YBaCuO might be expected in power-line applications to conduct currents with $J = 0.5 \times 10^6$ A/cm$^2$ < $J_c$, which requires $V_{sc} = 0.2$ cm$^3$ of superconductor per kiloamp-meter of conductor. In a present tape architecture containing a 3-μm-thick HTS coating deposited on a 50-μm-thick substrate, one has 3.3 cm$^3$ of metal in a kiloamp-meter of conductor. With a measured hysteretic loss of ~$200 \times 10^{-7}$ J/g per cycle at an operating frequency of 60 Hz, the resulting rate of energy dissipation is ~0.025 W/(kA-m). This is small compared with the losses expected from hysteresis in the superconductor per se when operated at a practical fraction of $I_c$. For substrates with still weaker ferromagnetism, the associated hysteretic loss should be even lower. Finally we note that the Ni-based substrate alloys can be expected to have an increased electrical resistivity that will reduce eddy current losses as well. Hence it appears that 7 t. % Cr material should be entirely satisfactory for many applications, obviating the need for higher Cr contents, for which the biaxial texturing is more difficult.

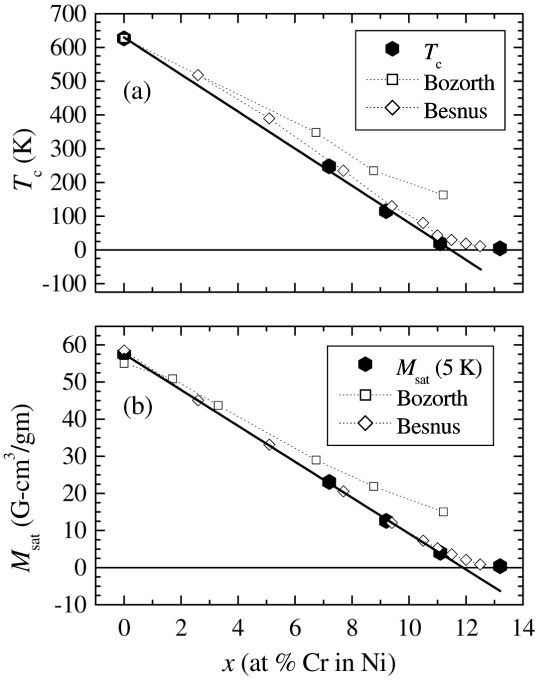


**Fig. 1.42. Variation of magnetic properties of $Ni_{1-x}Cr_x$ alloys with Cr content *x*.** (a) The Curie $T_c$ obtained here and those reported by Bozorth and by Besnus et al. The line is a linear dependence fitted to the present $T_c(x)$ data. (b) The saturation magnetization at $T$ = 5 K vs $x$.

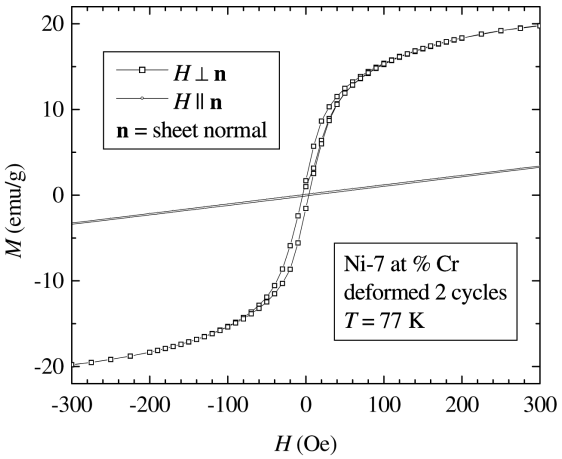


**Fig. 1.43. Magnetization loops (expanded scale) for a deformed $Ni_{93}Cr_7$ foil at 77 K, with magnetic field applied parallel or perpendicular to the plane of the foil.** The magnetization is relatively reversible, with limited hysteretic energy loss per cycle.

### 1.5.3 Texture in Ni-Cr Alloys

All alloy compositions studied were successfully textured to obtain ~100% cube texture. In Fig. 1.44, this is illustrated by the background-corrected (111)

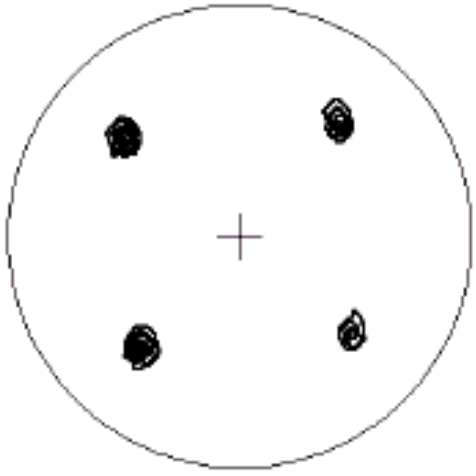

**Fig. 1.44. A (111) pole figure for a Ni-13 at. % Cr substrate that was annealed at 1050°C for 3 h.**

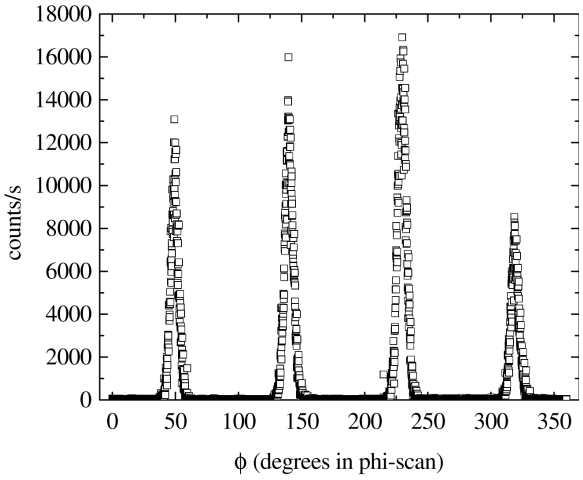


**Fig. 1.45. A ϕ-scan showing the in-plane texturing in the substrate (same as Fig. 1.44).** The FWHM is 7.8°.

pole figure for a Ni-13 at. % Cr substrate annealed at 1050°C for 2 h. Only four crystallographically equivalent peaks, corresponding to the {100}<100> cube orientation, are present in the pole figure. Quantification of the pole figure suggests ~100% cube texture in the sample. Figure 1.45 shows a ϕ-scan revealing the degree of in-plane texturing in the substrate. The FWHM as determined from the ϕ-scan is 7.8°. Figure 1.46 shows omega scans to demonstrate the degree of out-of-plane texturing in the substrate. Figure 1.46(a) was obtained with the sample rotated in the rolling direction. The FWHM of the texture is 5.7°. In Fig. 1.46(b) is an omega scan with the sample rotated about the rolling direction, for which the FWHM of the texture is 8.9°. Clearly, these results demonstrate that Ni-Cr alloys with Cr contents as high as 13 at. % Cr can be thermomechanically processed to form substrates with very sharp and fully formed cube texture.

## 1.5.4 Conclusions

This work shows that Ni-Cr alloys with much-reduced or nonexistent ferromagnetism can be fabricated and successfully processed to have biaxial cube texturing. The hysteretic loss in a deformed sample of alloy was measured; the results suggest that the loss in a coated conductor application should be small compared with that in first generation Bi-cuprate tapes.

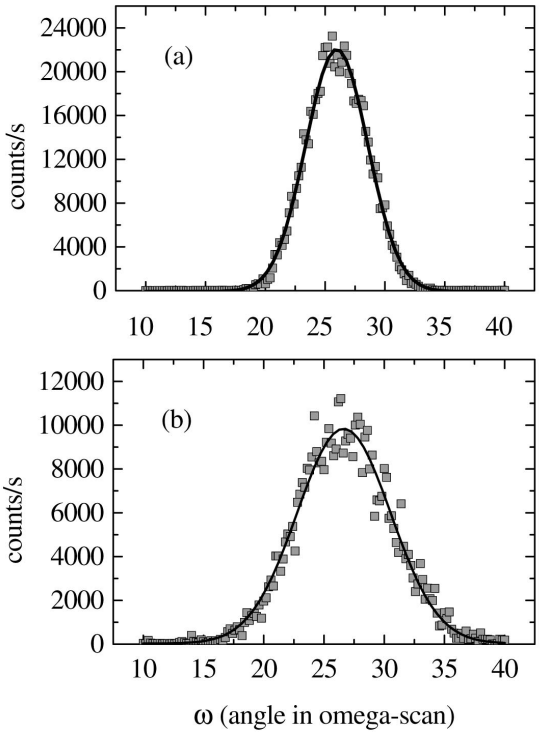


**Fig. 1.46. Angular ω-scans showing the degree of out-of-plane texturing (same substrate as Fig. 1.44).** (a) Sample rotated in the rolling direction, giving a FWHM of the texture of 5.7°; (b) sample rotated about the rolling direction, with FWHM of 8.9°.

### 1.5.5 Acknowledgments

We gratefully acknowledge 3M Company (R. E. Ericson and C. D. Hamilton) for ICP analyses of the alloys.

### 1.5.6 References

1. M. J. Besnus, Y. Gottehrer, and G. Munshy, *Phys. Stat. Sol. B* **49**, 597 (1972).
2. R. P. Bozorth, *Ferromagnetism*, IEEE Press, Piscataway, N.J., 1978, pp. 307–8.

## 1.6 REEL-TO-REEL CONTINUOUS CHEMICAL SOLUTION DEPOSITION OF EPITAXIAL $Gd_2O_3$ BUFFER LAYERS ON BIAXIALLY TEXTURED METAL TAPES FOR THE FABRICATION OF $YBa_2Cu_3O_{7-\delta}$ COATED CONDUCTORS

*T. Aytug, M. Paranthaman, S. Sathyamurthy, B. W. Kang, D. B. Beach, E. D. Specht, D. F. Lee, R. Feenstra, A. Goyal, D. M. Kroeger, K. J. Leonard, P. M. Martin, and D. K. Christen*

### 1.6.1 Introduction

For the commercial development of a practical superconducting wire technology, more adaptive and easily scalable processing techniques are required. Nonvacuum chemical-solution-based processes, such as sol-gel and metal organic decomposition (MOD), offer many desirable aspects, such as precise control of metal-oxide precursor stoichiometry and composition, mechanical simplicity, and low cost. Integration of these processes into HTS wire technology offers promise for the fabrication of both the epitaxial oxide buffer layers and the YBCO superconductors. Recently, it has been reported that various $RE_2O_3$ (rare-earth; RE = Gd, Yb, and Eu) and $RE_2Zr_2O_7$ (RE = La and Nd) oxide films can be grown epitaxially on textured Ni substrates by using solution-based methods. While short segments of sol-gel seeded Ni substrates with sputtered $CeO_2$/YSZ overlayers have yielded YBCO with $J_c$s in the range of 0.4 to $1.1 \times 10^6$ A/cm$^2$ at 77 K, long lengths of high-$J_c$ YBCO coatings on solution seed buffer layers have not yet been produced.

Much of the work reported using the RABiTS™ technique has utilized high-purity Ni (99.99%) as the texture material. However, the low mechanical strength and ferromagnetism of pure Ni present significant challenges in long-length manufacturing and hinder its usage in applications where ac losses are an issue. Therefore, it is desirable to work with textured alloy substrates that are much stronger and nonmagnetic, or that have reduced magnetism. Recently, the successful texturing of Ni strengthened with small additions of W (3–5 at. %) and Fe (1.7 at. %) have been reported. These substrates, typically 50-mm thick, accommodate similar annealing conditions and show comparable grain sizes to those of pure Ni. After recrystallization, however, they exhibit yield strengths (YSs) of 143 MPa and 154 MPa at 0.02% and 0.2% strain, respectively, which are much higher than those of pure Ni (YS = 40 MPa and 58 MPA, respectively). In addition, the saturation magnetization, M, of a Ni-(3 at. % W-1.7 at. % Fe), [Ni-alloy], (M = 40 G-cm$^3$/g) was found to be significantly lower than that of pure Ni (M = 57.5 G-cm$^3$/g at T = 0 K). Development of oxide buffer layers and HTS coatings both by vacuum and nonvacuum processes on these alloys has just begun. Recently, high-quality YBCO films with $J_c$ values (self-field, 77 K) of $1.9 \times 10^6$ A/cm$^2$ have been demonstrated on such substrates where the oxide buffer layers have been grown by all-vacuum processes. In addition to vacuum-based techniques, oxide buffer layers have also been grown directly on Ni-alloy tapes by nonvacuum solution-based methods. However, despite a good crystalline structure, to date there have been no reports on the growth of high-$J_c$ YBCO films on these sol-gel buffered alloy tapes.

Here we report the epitaxial growth and property characterizations of sol-gel processed, reel-to-reel dip-coated $Gd_2O_3$ seed buffer layers on textured Ni-alloy substrates. Second, we present the growth of high-quality YBCO coatings on short segments of $Gd_2O_3$/Ni-(3 at. % W-1.7 at. % Fe) with sputtered $CeO_2$/YSZ overlayers. Third, we demonstrate for the first time the continuous fabrication of high-$J_c$ HTS coatings in long lengths on solution-seeded pure Ni tapes. The electrical transport properties, measured over 100-cm lengths of YBCO films grown using the ex situ $BaF_2$ precursor process, are also reported.

## 1.6.2 Experimental Procedure

### 1.6.2.1 Preparation of Biaxially Textured Ni and Ni-Alloy Substrates

Biaxially textured Ni (99.99%) and Ni-(3 at. % W-1.7 at. % Fe) substrates were obtained by progressive cold rolling of polycrystalline, randomly oriented Ni and Ni-alloy bars to about a 95 to 98% deformation. After mechanical deformation, 50-μm-thick, 1-cm-wide substrates were first cleaned with isoproponal in a reel-to-reel ultrasonic cleaning unit and were then annealed at 1100°C (for pure Ni) or 1250°C (for Ni-alloy) for 1 h in a reducing forming-gas atmosphere (96% Ar + 4% $H_2$). The procedure yields the desired {100}<100> cube texture to typical levels of 6 to 8° FWHM.

### 1.6.2.2 Preparation of $Gd_2O_3$ Solution and Coating Procedure

A 2-methoxyethanol solution of gadolinium methoxyethoxide/acetate, prepared by an alkoxide sol-gel synthesis route, was used to coat the Ni and Ni-alloy tapes. The solution preparation was carried out under an Ar gas atmosphere using a Schlenck-type apparatus. In order to avoid premature hydrolysis, which can induce precipitation, the as-received gadolinium acetate powder was first purified by dissolving it in a mixture of water and acetic acid at a ratio of 3:1, filtering, and then evaporating to dryness in an oven maintained at 150°C overnight to remove absorbed moisture. Then the purified gadolinium acetate (about 3.34 g) was dissolved in 40 mL of 2-methoxyethanol in a 250-ml round-bottom flask. The flask was refluxed for 1 h with an excess of 2-methoxyethanol to exchange the acetic acid ligand with the methoxyethoxide ligand. The final volume was adjusted to 40 mL to produce a 0.5 M $Gd_2O_3$ precursor solution.

In a reel-to-reel dip-coating unit, as shown schematically in Fig. 1.47, tapes with dimensions of 10 cm in length and 1 cm in width were coated to determine the optimum processing parameters of $Gd_2O_3$ seed layers on Ni-alloy. The take-up reel was driven continuously by a stepper motor, and the pay-out reel was tensioned by a variable-torque motor. The textured tapes from the pay-out reel were continuously pulled through the $Gd_2O_3$ precursor solution at a constant speed in the range of 20 to 300 cm/h. These double-sided, dip-coated tapes were then transported through a preheated furnace at various temperatures ($T_{an}$) and speeds ($S_{an}$), ranging from 1050 to 1250°C and 5 to 30 cm/h in flowing forming-gas atmosphere. After the growth conditions of $Gd_2O_3$ were optimized on Ni-alloys, the same parameters were used for the growth on Ni tapes.

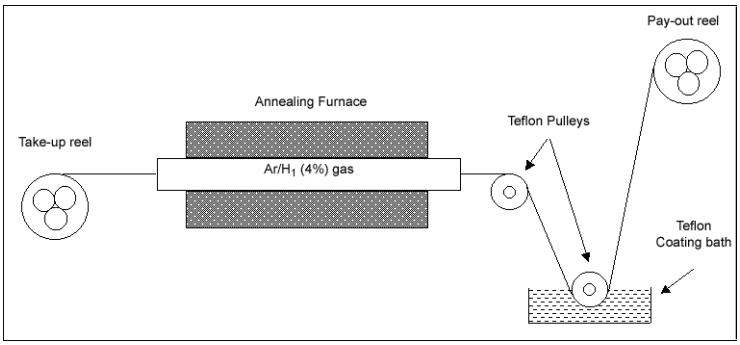


**Fig. 1.47. Schematic diagram of the reel-to-reel continuous dip-coating unit.**

#### 1.6.2.3 Preparation of YBCO test structures

Sputtering by the rf-magnetron technique was used to deposit both YSZ and $CeO_2$ overlayers on short segments of the dip-coated substrates, yielding the buffer-layer sequence, $CeO_2$/YSZ/$Gd_2O_3$/Ni-(3 at. % W-1.7 at. % Fe). Oxide sputtering targets were 2 in. in diameter, and the system base pressure was $1 \times 10^{-6}$ Torr. Samples were attached onto a heated substrate block assembly by clipping at both ends in an on-axis sputtering geometry. Sputtering conditions for both oxides consist of a mixture of 10 mTorr forming gas and $2 \times 10^{-6}$ Torr $H_2O$, and a substrate temperature of 780°C. Typical film thicknesses for these YSZ and $CeO_2$ layers were about 200 nm and 20 nm, respectively.

To assess the quality of the $CeO_2$/YSZ/$Gd_2O_3$/Ni-alloy multilayer structure, YBCO films were deposited by PLD, using a XeCl excimer laser system operated with an energy density of ≈4 J/cm$^2$. The laser repetition rate was 10 Hz, and the system background pressure was 5 to $8 \times 10^{-6}$ Torr. During YBCO deposition, substrates were maintained at 780°C in 120 mTorr of $O_2$. After deposition, the samples were cooled to 600°C at a rate of 5°C/min; then the $O_2$ pressure was increased to 550 Torr, and the samples were cooled to room temperature at the same rate. Typical YBCO film thicknesses were 200 nm.

#### 1.6.2.4 Characterization techniques

X-ray diffraction was employed to analyze phase, structure, and texture (i.e., the orientation relationship of the grains relative to the substrate material geometry) of the buffer layers as well as the YBCO coatings deposited on short samples. A Philips model XRG3100 diffractometer with Cu $K_\alpha$ radiation was used to record powder diffraction patterns. Texture analysis was achieved using a Rigaku rotating-anode X-ray generator with a graphite incident-beam monochromator selecting Cu $K_\alpha$ with slits defining $2 \times 2$ mm$^2$ beam. Pole figures were collected by a 4-circle diffractometer. The out-of-plane alignments (ω-rocking curve scans) of the films were measured by rocking the desired (00*l*) planes about an axis perpendicular to the scattering plane (ω-axis). The in-plane alignments (ϕ-scans) were measured by rotating the desired (hkl) planes normal to the sample plane. Peak-width FWHM values were determined by least-square fitting to Gaussian line shapes.

The texture of long-length samples was measured by a Huber four-circle diffractometer to accommodate a reel-to-reel translation stage. Data were obtained as a function of position by continuously measuring out-of-plane (ω-rocking curve scan) and in-plane (ϕ-scan) alignments, while translating the sample. Microstructural investigations were conducted using a Hitachi S-4100 high-resolution field emission type scanning electron microscope (HRSEM). Thicknesses of the buffer and superconducting layers were determined by RBS. In addition, ion spectroscopy techniques were employed to determine the carbon content of the dip-coated buffers by using a resonance for the 1.73 MeV $H^+$ ions at near-normal incidence. A standard four-point contact technique was applied to measure the superconducting critical temperature ($T_c$) and $J_c$ of the YBCO films. Values of $J_c$ were assigned at a 1-μV/cm criterion. Electrical contacts of silver were deposited onto the samples using dc-magnetron sputtering followed by an $O_2$ annealing for 30 min at 1 atm and 500°C.

### 1.6.3 Results and Discussion

#### 1.6.3.1 Growth of $Gd_2O_3$ Seed Layers on Biaxially Textured Ni-Alloy Substrates

Figure 1.48 shows the XRD θ-2θ spectrum for a series of dip-coated $Gd_2O_3$ seed layers processed at various temperatures, ranging from 1050 to 1170°C, at a fixed annealing speed of 10 cm/h. At a depostion temperature ($T_{dep}$) ≤ 1100°C, broad and relatively low-intensity (00*l*) $Gd_2O_3$ reflections were observed as

evidence of inhomogeneity or high structural defect density. For 1100°C < $T_{dep}$ < 1175°C, the (00*l*) peak intensities increase and the reflections sharpen, indicating substantial improvement in the crystalline quality of the films. Since the dip-coated film thickness is directly proportional to the coating speed, which was kept constant for each individual sample, comparison of the relative $Gd_2O_3$ (00*l*) peak intensities reflects the crystalline quality of the films. At temperatures above 1200°C, however, the films showed extra $Gd_2O_3$ peaks reflections, which are indexed as belonging to $Gd_2O_3$ monoclinic phase components.

To investigate the influence of annealing speed on the crystalline quality of $Gd_2O_3$, a series of films were annealed at annealing temperature ($T_{an}$) = 1150°C at different annealing speeds, in the range of 5 to 30 cm/h. From the comparable (00*l*) θ-2θ peak intensities, shown in Fig. 1.49, it is apparent that the annealing speed does not significantly affect the crystalline quality of the $Gd_2O_3$. The effect of annealing speed on the in-plane and the out-of-plane texture of $Gd_2O_3$ layers was also studied at a fixed speed ($S_{an}$ = 10 cm/h); the results are shown in Figs. 1.50(a) and 1.50(b), respectively. Note that biaxially textured Ni-alloy substrates generally have slightly different in-plane and out-of-plane textures, depending on the specific rolling and crystallization conditions. Thus, to make a direct and more quantitative comparison between the processing parameters and the crystalline quality of the grown films, the FWHM peak-width ratio relative to the underlying Ni-alloy is plotted as a function of $T_{an}$.

Substantial improvement in the in-plane and out-of-plane alignment of the $Gd_2O_3$ layers is observed with an increase in temperature above 1050°C. However, depositions at $T_{an}$ > 1100°C, did not significantly affect the epitaxial quality. Similarly, the effect of annealing speed on the epitaxial growth of the films (for the same samples studied in Fig. 1.49) can be observed from the results of ω- and ϕ-scan peak-width ratios, as shown in Fig. 1.51, for a fixed annealing temperature ($T_{an}$ = 1150°C).

While annealing speed does not have a remarkable influence on the in-plane alignment of the films, an increase in annealing speed beyond 20 cm/h has a negative effect on the out-of-plane texture, as evidenced by the gradual increase in the ω-scan FWHM ratios. Since the uniform hot-zone length is only approximately 10 cm for the present furnace, the latter effect for higher annealing speed can likely be correlated with the decreased residence time in the

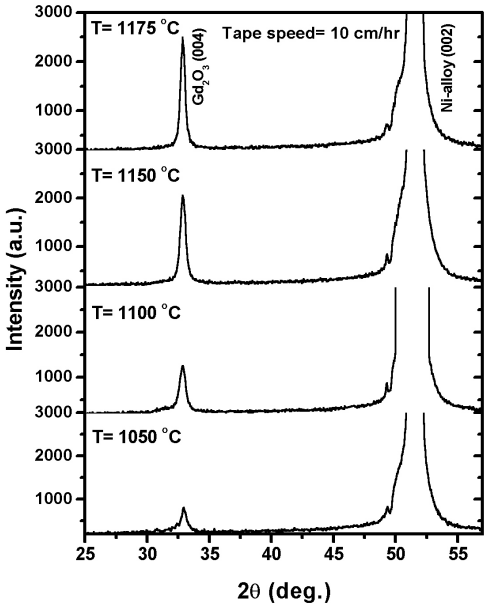


**Fig. 1.48. XRD θ-2θ patterns of dip-coated $Gd_2O_3$ films grown on biaxially textured Ni-(3 at. % W-1.7 at. % Fe) substrates at various annealing temperatures.**

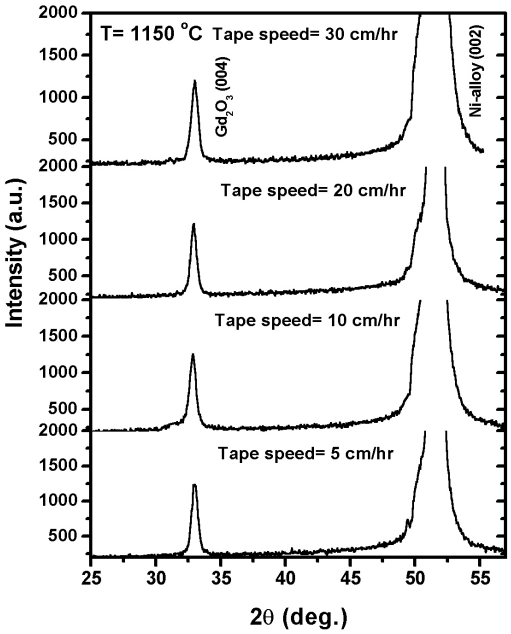


**Fig. 1.49. XRD θ-2θ patterns of dip-coated $Gd_2O_3$ films grown on biaxially textured Ni-(3 at. % W-1.7 at. % Fe) substrates at 1150°C, for various annealing speeds.**

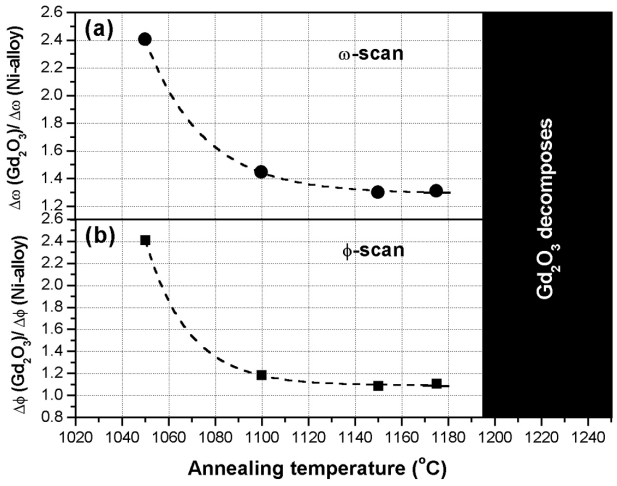


**Fig. 1.50. Dependence of the normalized XRD FWHM peak widths, quantifying the crystallinity of $Gd_2O_3$ films as a function of post-annealing temperature. (a) The out-of-plane distribution width $\Delta\omega$. (b) The in-plane distribution width $\Delta\phi$.** The lines serve as a visual guide.

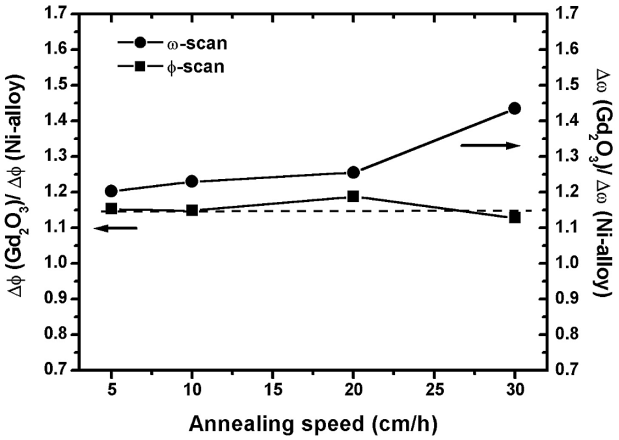


**Fig. 1.51. Effect of post-annealing speed on the FWHM ratios of $\omega$-rocking curves and $\phi$-scans for $Gd_2O_3$ films on Ni-(3 at. % W-1.7 at. % Fe) tapes, fabricated at 1150°C.** The dashed line serves as a visual guide.

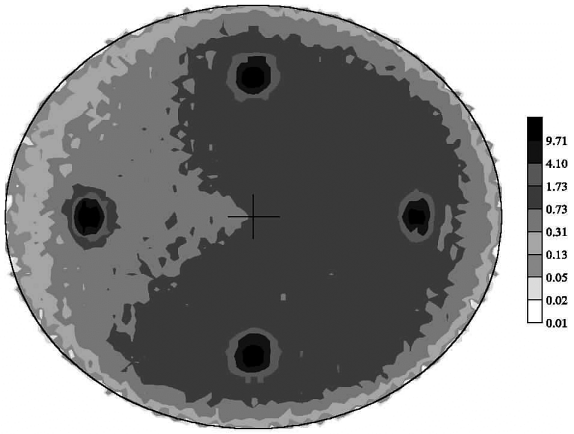


**Fig. 1.52. The (222) logarithmic pole figure of a 25-nm-thick dip-coated $Gd_2O_3$ film processed on biaxially textured Ni-(3 at. % W-1.7 at. % Fe) at 1150°C with an annealing speed of 20 cm/h.**

effective hot zone. On the other hand, the in-plane alignment is very likely governed by the crystallographic texture of the underlying substrate. Therefore, Figs. 1.48 through 1.51 suggest that the optimal ranges for annealing temperature and speed for epitaxial growth of $Gd_2O_3$ on Ni-(3 at. % W-1.7 at. % Fe) should be $T_{an}$ = 1100 to 1175°C and $S_{an}$ < 30 cm/h.

The epitaxial quality of the $Gd_2O_3$ films was examined by XRD pole figure analysis. The logarithmic-scale (222) pole figure for a film processed at $T_{an}$ = 1150°C and $S_{an}$ = 20 cm/h is shown in Fig. 1.52. The data indicate single-domain epitaxy, with the $Gd_2O_3$[001]//substrate[001] and the $Gd_2O_3$[110]//substrate[100]. This result is important, since any other orientational domains could lead to the potential disruption of current flow by high-angle grain boundaries in the HTS layer.

For implementation of low-cost, nonvacuum dip-coated $Gd_2O_3$ seed layers into long-length wire manufacturing, it is important grow dense, crack-free layers with minimum carbon contamination. Resonant RBS has been used to analyze the carbon levels (number of carbon atoms/number of gadolinium atoms) in several $Gd_2O_3$ samples, with an interest on the correlation with respect to annealing temperature and annealing speed. The results are summarized in Table 1.2. The slight variations in thickness for the same coating speed are due to differences in the solution viscosity. While we observe no strong dependence of carbon content on either annealing temperature or speed, the overall carbon levels

**Table 1.2. Processing conditions and the resulting carbon contents of several dip-coated $Gd_2O_3$ films for a series of annealing temperatures, annealing speeds and coating speeds**

| Temperature (°C) | Coating speed (cm/h) | Annealing speed (cm/h) | $Gd_2O_3$ thickness (Å) | Carbon atoms per unit cell area |
|---|---|---|---|---|
| 1050 | 300 | 10 | 700 | 165 |
| 1100 | 300 | 10 | 700 | 149 |
| 1150 | 300 | 10 | 700 | 88 |
| 1150 | 20 | 5 | 200 | 35 |
| 1150 | 20 | 20 | 200 | 24 |
| 1150 | 20 | 30 | 200 | 40 |

are significant (≈0.4–0.6 carbon/gadolinium atom). These levels, however, do not adversely affect the surface morphology of the thinner buffers, as shown in the following figures. Plan-view HRSEM micrographs of the surface morphology for 25-nm- and 73-nm-thick $Gd_2O_3$ films fabricated on biaxially textured Ni-alloy substrates are presented in Figs. 1.53(a) and 1.53(b), respectively. While each sample exhibits a continuous, crack-free, and dense surface morphology, significant surface roughening develops for the thicker coatings [Fig. 1.53(b)]. On the other hand, thinner coatings (25 nm) exhibit extremely smooth and featureless surface microstructure [Fig. 1.53(a)], with a root mean square (rms) roughness of ~3 nm as determined by atomic force microscopy measurements. Such surface morphology should best serve the goal of obtaining high-quality YBCO coatings, despite the internal carbon content of the $Gd_2O_3$. The effects of $Gd_2O_3$ seed layer thickness on the growth characteristics of subsequent oxide buffer layers are discussed in the following section.

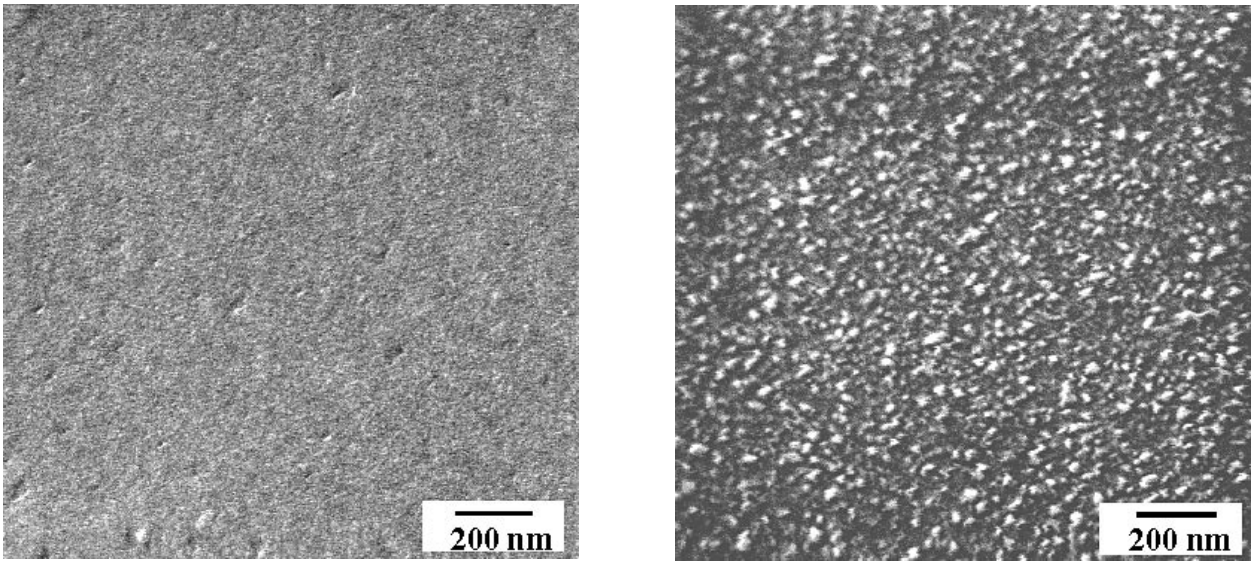


**Fig. 1.53. High-resolution SEM micrographs for (a) 25-nm, and (b) 73-nm sol-gel dip-coated $Gd_2O_3$ seed layers on (100) textured Ni-(3 at. % W-1.7 at. % Fe) substrates.**

### 1.6.3.2 Structural and Superconducting Property Characterizations of YBCO/$CeO_2$/YSZ/$Gd_2O_3$/Ni-Alloy Multilayer Structure

After optimizing the fabrication process for dip-coated $Gd_2O_3$ films on Ni-alloys, we first deposited YSZ and $CeO_2$ overlayers by rf-magnetron sputtering and then investigated the quality of this solution-seeded $CeO_2$/YSZ/$Gd_2O_3$ buffer layer structure by depositing YBCO films. In this architecture the YSZ buffer layer acts as a Ni diffusion barrier; the $CeO_2$ layer ensures a better lattice match with YBCO. Figures 1.54(a) and 1.54(b) show the results of XRD θ-2θ scans for the $CeO_2$/YSZ bilayers deposited on $Gd_2O_3$/Ni-alloy substrates, where the $Gd_2O_3$ layer thicknesses are 20 and 70 nm, respectively. The data show that $CeO_2$/YSZ bilayers grown on thicker $Gd_2O_3$ layers have a polycrystalline nature [Fig. 1.54(b)], whereas films deposited on thinner seed layers exhibit excellent *c*-axis oriented growth [Fig. 1.54(a)]. This growth behavior seems overwhelmingly governed by the surface morphology of the $Gd_2O_3$ films.

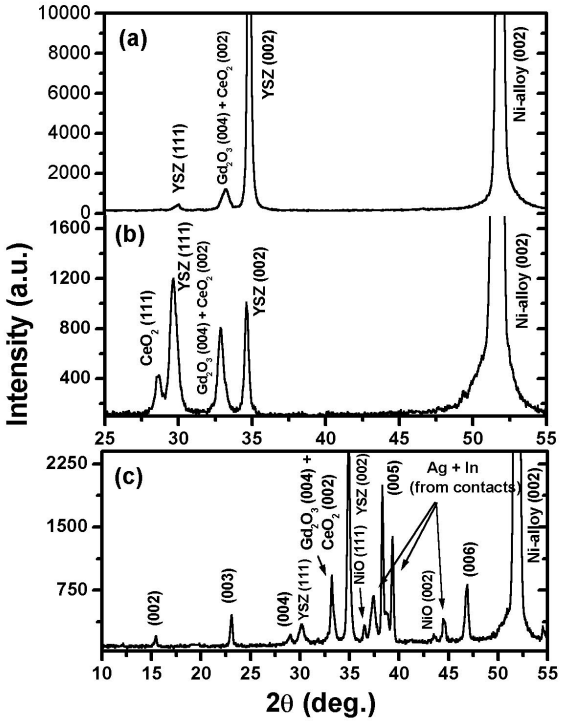


**Fig. 1.54. XRD θ-2θ scans of the $CeO_2$/YSZ bilayers on $Gd_2O_3$/Ni-(3 at. % W-1.7 at. % Fe) substrates, where the $Gd_2O_3$ layer thickness is about (a) 25 nm, and (b) 73 nm. (c) A typical XRD θ-2θ spectrum for a YBCO film on the $CeO_2$/YSZ/$Gd_2O_3$(20 nm)/Ni-(3 at. % W-1.7 at. % Fe) multilayer structure.** YBCO peaks are labeled by (00l) indices.

It is known that surface roughness exacerbates adverse interfacial reaction between the film and the substrate. Therefore, the relatively coarse surface morphology of thicker $Gd_2O_3$ films may contribute to polycrystalline growth behavior of the $CeO_2$/YSZ overlayers. Following deposition of $CeO_2$/YSZ overlayers, suitability of the $CeO_2$/YSZ/$Gd_2O_3$/Ni-alloy structure was tested with the growth of YBCO films. A typical XRD θ-2θ scan is shown in Fig. 1.54(c), where the pattern indicates only (00*l*) reflections for the YBCO, demonstrating a *c*-axis perpendicular to the substrate surface. After YBCO deposition, weak NiO impurity peaks are observed at 37° and 44°, implying minor oxidation of the metal substrate interface during the HTS processing step. However, this occurrence seems to have no adverse effect on the superconducting properties. The relative in-plane and out-of-plane textures between individual layers are documented in Figs. 1.55(a) and 1.55(b), respectively. The ω-rocking curve scans [Fig. 1.55(a)], obtained through the (002) peak reflections for Ni, YSZ, and $CeO_2$; the (004) reflection for $Gd_2O_3$; and the (006) reflection for YBCO, yield peak-width FWHM values (Δω) of 5.2, 7.2, 7.7, 6.4, and 5.8°, respectively, indicating good out-of-plane crystallographic alignment among the layers. In-plane textures of the individual layers for the same sample are illustrated in Fig. 1.55(b), where ϕ-scan data through the YBCO(103), $CeO_2$(111), YSZ(111), $Gd_2O_3$(222), and Ni(111) reflections reveal four equally spaced peaks, with similar in-plane FWHM values (Δϕ) of about 8 to 9°. These in-plane epitaxial orientations correspond to $CeO_2$, YSZ, and $Gd_2O_3$ basal planes that are rotated 45° relative to in-plane Ni-alloy substrate (100) axis, whereas the *a*-axis and *b*-axis of the YBCO are rotated 45° with respected to the top $CeO_2$ axes. The observed 45° rotations are anticipated according to the lattice match considerations between subsequent layers.

Since the qualifying test for any coated-conductor buffer-layer structure is compatibility with the deposition of high-quality, high-$J_c$ YBCO coatings, electrical-transport and superconducting property measurements were conducted on the same sample. Figure 1.56 compares the magnetic field (H∥*c*-axis) dependence of $J_c$ at 77 K with those of YBCO films grown on solution-derived $CeO_2$/YSZ/$Gd_2O_3$(dip-coated)/Ni and on standard, all vacuum deposited buffer-layer RABiTS™ architecture of $CeO_2$/YSZ/$CeO_2$/Ni. The inset in Fig. 1.56 shows the superconducting transition region of the temperature-dependent resistivity, yielding a zero-resistance $T_c$ = 90.5 K. The zero-field transport $J_c$ of the YBCO/$CeO_2$/YSZ/$Gd_2O_3$/Ni-alloy sample is $1.2 \times 10^6$ A/cm$^2$, and it exhibits a high irreversibility field ($H_{irr}$) of 7 T. This $J_c$ performance is comparable to that of epitaxial YBCO films on $CeO_2$/YSZ/$Gd_2O_3$(dip-coated) and $CeO_2$/YSZ/$CeO_2$ buffered biaxially textured Ni substrates. Thus, the microstructural requirements for high $J_c$ are imparted in YBCO through the $CeO_2$/YSZ/$Gd_2O_3$, including a near absence of weak-linked high-angle grain boundaries and an overall high degree of in- and out-of-plane alignment. The slight differences in high-field $J_c$ behavior of the different samples arise from subtle variations in flux pinning properties, which can be associated with small changes in YBCO deposition conditions, composition, and substrate surface properties.

### 1.6.3.3 Long-Length Fabrication of RABiTS™ Architecture Based on Dip-Coated $Gd_2O_3$/Ni Tapes

Having realized excellent structure and superconducting properties of YBCO films on short segments of $CeO_2$/YSZ capped, sol-gel synthesized $Gd_2O_3$ seed layers, we devoted our efforts to long-length implementation of the same architecture on Ni tapes. Figure 1.57 plots the XRD ω-rocking curve intensity distributions for the $CeO_2$(002)+$Gd_2O_3$(004) and YSZ(002) peak reflections taken along a 1-m length of $CeO_2$/YSZ/$Gd_2O_3$(dip-coated) buffered Ni tape. The tape was drawn through the solution at a rate of 80 cm/h, and the film was annealed in a

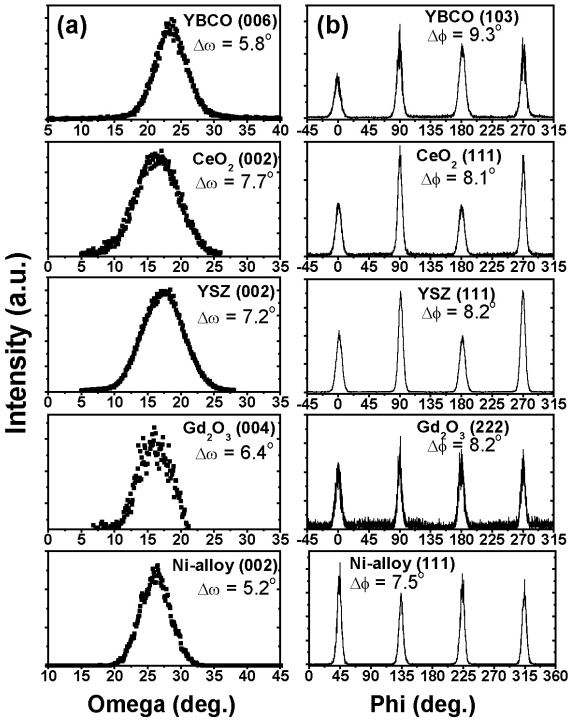


**Fig. 1.55. XRD (a) out-of-plane (ω-scans) and (b) in-plane (ϕ-scans) texture for an epitaxial YBCO film (200 nm thick) on a $CeO_2$/YSZ/$Gd_2O_3$/Ni-(3 at. % W-1.7 at. % Fe) multilayer structure.** The FWHM (Δω and Δϕ) for each scan are indicated.

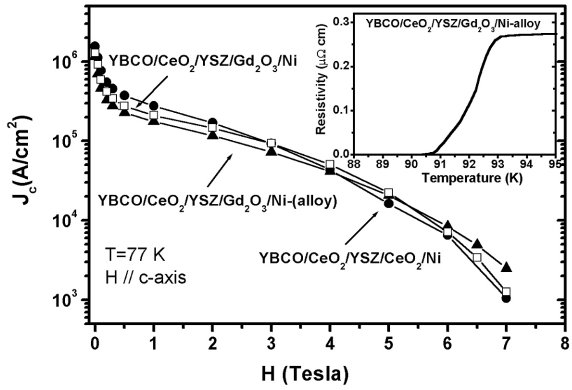


**Fig. 1.56. Magnetic field dependence of $J_c$, measured at 77 K, for a YBCO film on the $CeO_2$/YSZ/$Gd_2O_3$/Ni-(3 at. % W-1.7 at. % Fe) multilayer structure.** Also shown for comparison are $J_c$ (H, 77 K) for the YBCO/$CeO_2$/YSZ/$Gd_2O_3$/Ni and YBCO/$CeO_2$/YSZ/$CeO_2$/Ni. The inset shows the resistive superconducting transition region of the present sample.

preheated furnace (see Fig. 1.47) at a speed of 20 cm/h at 1130°C. It should be mentioned that by reducing the concentration of $Gd_2O_3$ precursor solution from 0.5 M to 0.25 M, an 80 cm/h coating speed results in a layer thickness of approximately 20 to 25 nm.

Uniform *c*-axis alignment among the buffer layers can be seen in Fig. 1.57. Slight changes in the ω-rocking curve intensities are caused by variations in the thickness of the buffer layers. Since the Bragg angles for the $CeO_2$(002) and $Gd_2O_3$(004) reflections are nearly coincident, it was not possible to distinguish them within the resolution of our XRD system. Similarly, excellent uniformity for the in-plane texture of the YSZ layer is evident from the plot of XRD ϕ-scan intensity distribution recorded from the YSZ(111) reflection along the tape length (Fig. 1.58). The ω- and ϕ-scan FWHM values of 7.7° and 8.7° obtained for the $CeO_2$-YSZ-$Gd_2O_3$ buffers and the YSZ layer, respectively, are comparable to those of the Ni substrate ($\Delta\omega = 7.8°$, $\Delta\phi = 8.5°$). The quality of this tape was examined by depositing YBCO films using the ex situ $BaF_2$ precursor process in a reel-to-reel system. The results of electrical transport $J_c$ measurements at 77 K and zero applied field, conducted over a 80-cm-long section of the same YBCO/$CeO_2$/YSZ/$Gd_2O_3$/Ni tape, are shown in Fig. 1.59. The sectional $J_c$ values were taken at each 1-cm increment along the tape length. The tape width is 1 cm, and the thickness of the YBCO coating is 300 nm. It is clear from the figure that the sample exhibits an average $J_c$ value of $7.5 \times 10^5$ A/cm$^2$ and that it supports an end-to-end $J_c$ of $6.25 \times 10^5$ A/cm$^2$, with some regions reaching to $J_c$ values of $1 \times 10^6$ A/cm$^2$. The latter value represents the best-recorded performance on short samples. The low-$J_c$ sections marked with an asterisk (*) are associated with visible line features along the YBCO thickness, resulting from the variations in the composition of YBCO($BaF_2$) precursor films. Despite the existence of these flaws, this result establishes a new benchmark for performance that was attained on a RABiTS™ structure having a nonvacuum solution-processed seed layer.

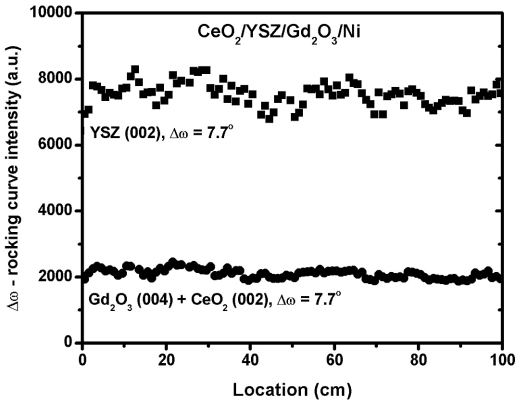


**Fig. 1.57. XRD ω-rocking curve intensity distributions for the $CeO_2$(002)+$Gd_2O_3$(004) and the YSZ(002) peak reflections as a function of the length over vacuum- and nonvacuum-processed $CeO_2$/YSZ/$Gd_2O_3$ buffer layers on a 1-m-long biaxially textured Ni tape.**

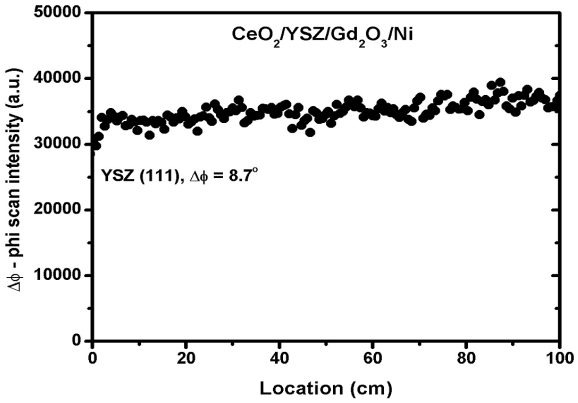


**Fig. 1.58. Longitudinal distribution of XRD ϕ-scan intensity of YSZ(111) peak reflection for the tape described in Fig. 1.57.**

Recently, we have successfully fabricated $Gd_2O_3$ seed layers on long lengths of Ni-alloy tapes as well (see Fig. 1.60). Currently, efforts are under way to complete the buffer structure with $CeO_2$/YSZ overlayers for the further growth of high-quality YBCO films on these lengths of $Gd_2O_3$/Ni-alloy substrates. In addition, we are also investigating an all-solution route to produce both buffers and YBCO superconductors for the practical development of coated conductors.

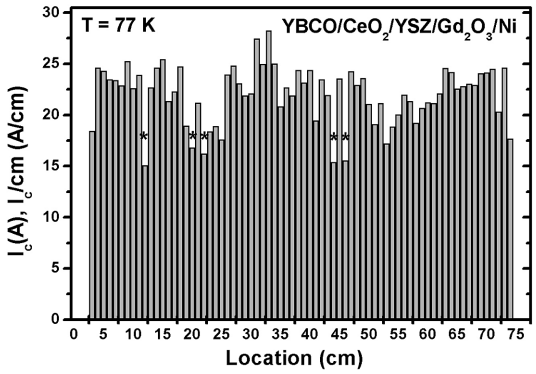


**Fig. 1.59. Sectional $J_c$ (77 K, self-field) values for the YBCO film obtained on 1-m-long sol-gel-seeded $CeO_2$/YSZ/$Gd_2O_3$/Ni tape.** Visible line features marked by an asterisk (*).

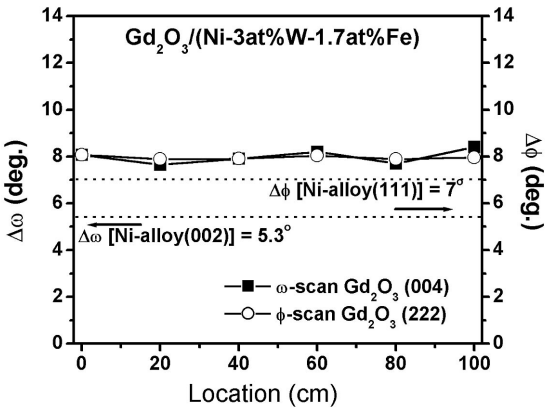


**Fig. 1.60. Phi and omega scans of a $Gd_2O_3$ seed layer deposited on a long length of biaxially textured Ni-3 at. % W-1 at. % Fe substrate.**

### 1.6.4 Summary and Conclusion

We have demonstrated for the first time the successful fabrication of high-$J_c$ YBCO coatings on sol-gel processed, reel-to-reel dip-coated $Gd_2O_3$ seed buffer layers on textured, strengthened Ni-alloy substrates, with sputtered $CeO_2$/YSZ overlayers. We first investigated the viability of $Gd_2O_3$ as the seed buffer layer and obtained the optimum processing conditions (i.e., post-annealing speed, coating speed, and temperature) for the epitaxial growth of $Gd_2O_3$ on Ni-alloy. High-quality $Gd_2O_3$ layers were achieved at temperatures between 1100 and 1150°C under a reducing forming-gas atmosphere (96% Ar + 4% $H_2$). It has been found that while the post-annealing speed does not have a significant effect on the in-plane alignment of $Gd_2O_3$, out-of-plane alignment has a tendency to degrade for an annealing speed exceeding 20 cm/h. Scanning electron microscopy observations revealed a continuous, dense, and crack-free surface morphology for these dip-coated buffers. Moreover, the surface roughness of $Gd_2O_3$ films depends strongly on the thickness of the layers, which depends on coating speed and solution viscosity. Our results indicated significant surface roughening for thicker $Gd_2O_3$ layers, whereas thinner coatings produced extremely smooth and uniform films. These findings also showed notable differences on the growth characteristics of the subsequent YSZ and $CeO_2$ barrier and cap layers. The YBCO films grown on the short segments of $CeO_2$/YSZ/$Gd_2O_3$/Ni-(3 at. % W-1.7 at. % Fe) multilayer structure, having 20-nm-thick $Gd_2O_3$ seed layers, yielded self-field $J_c$ values as high as $1.2 \times 10^6$ A/cm$^2$ at 77 K. The magnetic field performance of $J_c$ was as good as that obtained for YBCO films on standard $CeO_2$/YSZ/$CeO_2$ buffered Ni substrates.

After establishing this proof of principal on short prototype conductors, we have presented our results in a long-length demonstration of dip-coated $Gd_2O_3$ seed layers on biaxially textured Ni. The $Gd_2O_3$ seed layers showed a very uniform texture along the tape length (100 cm). The YBCO films grown using the ex situ $BaF_2$ precursor approach on the nonvacuum and vacuum-derived $CeO_2$(sputtered)/YSZ(sputtered)/$Gd_2O_3$(dip-coated)/Ni multilayer structure supported a mean self-field $J_c$ value of $7.5 \times 10^5$ A/cm$^2$ at 77 K with some regions reaching to $1 \times 10^6$ A/cm$^2$. These observations clearly underscore the strong viability of a nonvacuum, chemical-solution-based sol-gel synthesis route in manufacturing high-quality, long-length buffered tapes (Ni or Ni-alloys) for the development of RABiTS™-based coated conductors.

## 1.7 $La_{0.7}Sr_{0.3}MnO_3$: A SINGLE, CONDUCTIVE-OXIDE BUFFER LAYER FOR THE DEVELOPMENT OF $YBa_2Cu_3O_{7-\delta}$ COATED CONDUCTORS

*T. Aytug, M. Paranthaman, B. W. Kang, S. Sathyamurthy, A. Goyal, and D. K. Christen*

Here we report the fabrication of high-quality YBCO coatings on a single, conductive buffer layer deposited on high-purity biaxially textured Ni tapes. We also report the structural, electrical, and superconducting properties of these short prototype conductors.

Biaxially textured Ni substrates were obtained from randomly oriented high-purity (99.99%) Ni bars, which were first mechanically deformed by cold-rolling and then annealed in vacuum at 1000°C for 1 h to obtain the desired (100) cube texture. The deposition of $La_{0.7}Sr_{0.3}MnO_3$ (LSMO) buffer layers was performed with an rf-magnetron sputtering system using the oxide target. Typical sputtering conditions for LSMO consisted of a sputter-gas mixture of Ar and $O_2$ at a ratio of Ar:$O_2$ = 15:2, with a total pressure of 3 mTorr, and a substrate temperature in the range of 550 to 600°C. A deposition rate of ≈0.7 Å/s resulted, yielding film thicknesses of 400 to 700 nm.

PLD was used for the deposition of YBCO films, utilizing a XeCl excimer laser system, operated with an energy density of ≈4 J/cm$^2$, at a repetition rate of 10 Hz. During YBCO deposition, substrates were maintained at 790°C in 120 mTorr of $O_2$. After deposition, the samples were first cooled to 600°C at a rate of 7°C/min; then the $O_2$ pressure was increased to 550 Torr, and the samples were cooled to room temperature at the same rate. Typical YBCO film thicknesses were 200 nm. Crystal structures were characterized with a Huber high-resolution XRD, and microstructural analyses were conducted on a JOEL model JSM-840 scanning electron microscope (SEM). Secondary ion mass spectrometry (SIMS) depth-profile analyses were made to document possible cation contamination of YBCO. Electrical property characterizations were made using a standard four-probe technique, with values of $J_c$ assigned at a 1 μV/cm criterion.

The XRD θ-2θ spectrum for an LSMO buffer layer deposited on biaxially textured Ni is plotted in Fig. 1.61(a). Figure 1.62(b) plots the pattern for a YBCO film on an LSMO/Ni substrate. In both cases,

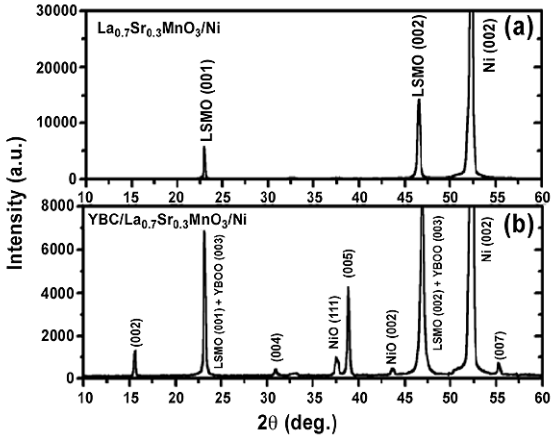


**Fig. 1.61. Typical XRD θ-2θ patterns (a) for a 600-nm-thick LSMO film on a biaxially textured Ni substrate and (b) for a 200-n-thick YBCO film on a LSMO/Ni multilayer.**

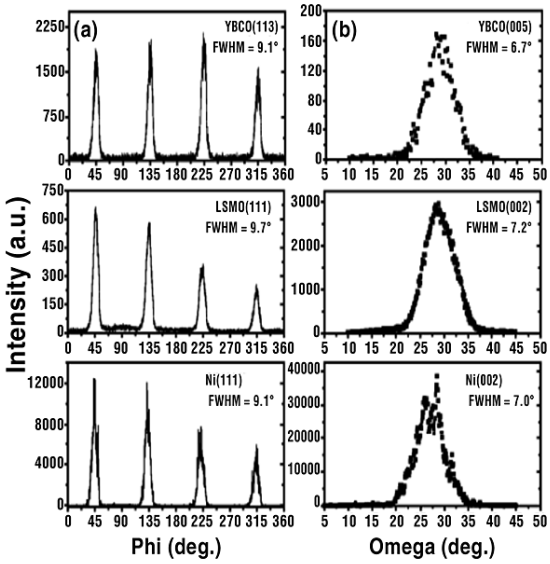


**Fig. 1.62. XRD (a) ϕ-scans and (b) ω-rocking curves for the YBCO/LSMO/Ni structure showing that the oxide layers tend to replicate the in-plane and out-of-plane texture of the Ni substrate.**

predominantly (00l) reflections are indexed, indicating excellent c-axis texture. After YBCO deposition, small impurity peaks at 37° and 44°, belonging to NiO, were detected, the consequence of which to the electrical properties of the samples will be discussed later. The relative in-plane (ϕ-scan) and out-of-plane (ω-rocking curve) textures of all three layers are documented in Figs. 1.61(a) and 1.61(b), respectively. The ϕ-scan FWHM values (Δϕ) of 9 to10° for Ni(111), LSMO(111), and YBCO(113) imply that both oxide layers closely replicate the in-plane texture of Ni. The layers assume in-plane epitaxial orientations, YBCO[110]//LSMO[110]//Ni[110]. The *c*-axis alignment was determined by T-rocking curve measurements as shown in Fig. 1.61(b). The data reveal good out-of-plane crystallographic texture among all layers. The FWHM values for YBCO(005), LSMO(002), and Ni(002) are 6.7°, 7.2°, and 7°, respectively.

The surface morphology of LSMO buffers is smooth, uniform, and crack-free; it has dense coverage, including on the Ni grain-boundary regions, as illustrated in Fig. 1.63(a). The surface microstructure of the same sample after YBCO deposition is shown in Fig. 1.63(b), where a dense and uniform microstructure is also observed. These results demonstrate that LSMO buffer layers can be grown epitaxially on biaxially textured Ni substrates and that they can provide a morphologically excellent template for the growth of YBCO films.

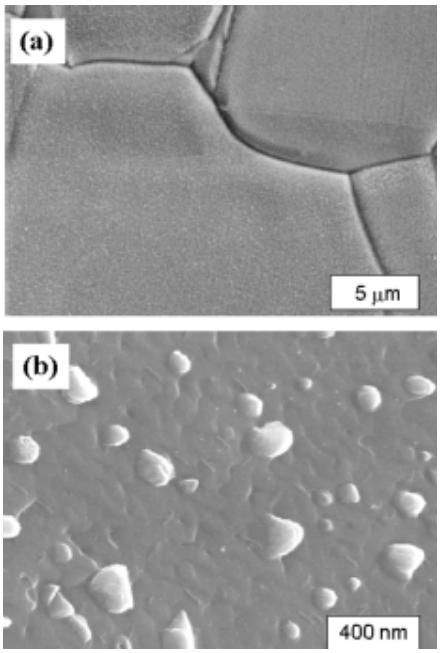


**Fig. 1.63. SEM micrographs of (a) the grain boundary region of LSMO/Ni structure and (b) the surface morphology of the YBCO film grown on the same conductive buffer structure shown in part (a).**

Electrical transport and superconducting property characterizations were conducted on the same sample, and the results are shown in Fig. 1.64, which displays the magnetic field dependence of $J_c$ at 77 K, with the field applied parallel to the c-axis. At zero applied field, the sample exhibits a high $J_c$ of $0.5 \times 10^6/cm^2$. This value is approximately half that obtained on RABiTS™ having both the "standard trilayer insulating buffer architecture," $CeO_2$/YSZ/$CeO_2$/Ni, and "bilayer conductive architecture," $SrRuO_3$/$LaNiO_3$. The SIMS depth profile analyses of YBCO/LSMO/Ni samples have indicated a low-level Sr contamination of YBCO, from the LSMO layer. We speculate that the observed lower $J_c$ behavior results from the combination of a somewhat broader distribution of grain-to-grain misorientations (resulting from the texture of the metal tape) and the observed contamination of YBCO with Sr, although the latter has not produced a marked depression of $T_c$. Efforts are under way to confirm this issue. Nevertheless, these results establish a new benchmark for performance in that the results were attained on a RABiTS™ structure having a single, conductive buffer layer. The inset of Fig. 1.64 displays the overall temperature-dependent resistivity and electrical coupling among the layers. Note that the net resistivity ($\rho_{net}$) is calculated from the thickness of the conductive structure (YBCO + LSMO + Ni substrate). For direct comparison, data for LSMO/Ni, as well as data for bare, biaxially textured Ni substrate are included. The $T_c$ of YBCO/LSMO/Ni is 89 K. Excellent electrical contact at the LSMO-Ni interface is evidenced by the similar $\rho_{net}$-$T$ behavior before and after deposition of the LSMO layer. After YBCO deposition, however, $\rho_{net}$ of entire structure increased beyond that expected from ideally coupled, parallel layers, given by $\rho_{net} = d_{tot}[d_M/\rho_M + d_B/\rho_B + d_S/\rho_S]^{-1}$. Here, the $d_i$ and $\rho_i$ values are thicknesses and resistivities of the various layers ($i$ = M, B, and S for the metal tape, buffer layer, and superconducting layer, respectively). This increase can be ascribed to the presence of some (111) and (002) textured NiO at

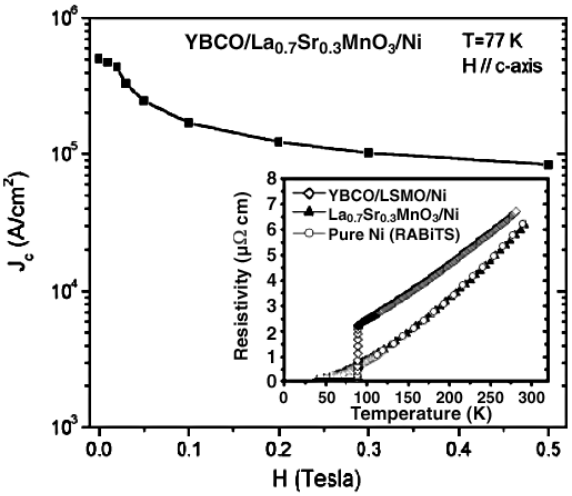


**Fig. 1.64. Magnetic field dependence of $J_c$ for YBCO/LSMO/Ni at 77 K.** The inset shows the temperature dependence of the net resistivity of the YBCO/LSMO/Ni structure. Also shown for comparison are the $\rho_{net}$-*T* data for as-grown LSMO/Ni and for a pure biaxially-textured Ni substrate.

the substrate-buffer interface, which was detected in the XRD spectra of Fig. 1.61(b). Nevertheless, the net resistivity value of only 2 to 3 μΩ-cm near liquid-nitrogen operating temperatures should provide significant stabilization. For example, a transient event that forced complete current sharing from a YBCO coating carrying 100 A/cm-width would dissipate a heat flux of only ~4 W/cm$^2$, which is well below the critical heat flux of ~10 W/cm$^2$ for nucleate boiling of liquid nitrogen.

In summary, we have demonstrated fabrication of high-quality epitaxial YBCO coatings on a single, conductive buffer layer of LSMO deposited on textured Ni substrates. The crystalline structure and the surface quality of this conductive architecture are excellent. For 200-nm-thick YBCO, self-field $J_c$ values of $0.5 \times 10^6$ A/cm$^2$ were achieved at 77 K. Most significantly, electrical-property characterizations revealed that there is good metallic connectivity between the YBCO coatings and the Ni substrate. The results in this work underscore the great potential and additional feasibility of LSMO buffer layers for the development of fully conductive RABiTS™-based YBCO coated conductors for HTS power applications.

## 1.8 HIGH-CURRENT-DENSITY YBCO COATED CONDUCTORS ON BIAXIALLY TEXTURED Ni-W (3 AT. %) SUBSTRATES

*M. Paranthaman, A. Goyal, R. Feenstra, D. F. Lee, S. Sathyamurthy, P. M. Martin, and D. M. Kroeger*

To demonstrate the growth of high-quality YBCO films on biaxially textured Ni-alloy substrates, we have chosen annealed Ni-W (3 at. %) substrates for this study. The annealed Ni-W (3 at. %) substrates are much stronger and have reduced magnetism compared with pure Ni substrates. The yield strength at 0.2% is 150 MPa, comparable to the 164-MPa yield strength of completely nonmagnetic Ni-Cr (13 at. %) substrates.

Here, we report our successful growth of high-current-density YBCO films on buffered Ni-W (3 at. %) substrates. Biaxially textured substrates were obtained by mechanically deforming metal rods over 95% followed by annealing at 1250 to 1300°C for 1 h in the presence of Ar/$H_2$ (4%) gas. The substrates used were 1 cm wide and 50 μm thick. Prior to annealing, the substrates were cleaned by sonification in isopropanol.

The $Y_2O_3$ seed layers were deposited directly on the substrates by reactive e-beam evaporation. An AIRCO Temescal CV-14 10-kW power supply with three e-beam guns was used for the deposition. The substrates were mounted on a heater in the e-beam system. The chamber was evacuated until the vacuum in the chamber reached $1 \times 10^{-6}$ Torr at room temperature. A gas mixture of 4% $H_2$ and 96% Ar was introduced until the pressure inside the chamber reached few Torr. The Ni-W substrates were pre-

annealed at 650°C for 1 h at that pressure. The chamber was then pumped and maintained at a pressure of $4 \times 10^{-5}$ Torr using a mixture of 4% $H_2$ and 96% Ar. A dc-powered piezoelectric valve controlled the gas flow. Yttrium metal in a tungsten crucible was used as the source.

The $Y_2O_3$ seed layers were grown on the substrates at 650°C. To measure the partial-pressure $H_2O$, $O_2$, $H_2$, and $CO_2$ gas flow in the chamber, an SRS RGA-100 gas analyzer was mounted in the e-beam system. The background $H_2O$ pressure was maintained at around $1 \times 10^{-5}$ Torr. The $H_2O$ pressure supplied in the chamber was sufficient to oxidize the film to the stoichiometric $Y_2O_3$. The deposition rate was 2 Å/s with the operating pressure of $10^{-5}$ Torr, and the final thickness was around 500 Å. The measured partial pressure of $O_2$ was in the range of $10^{-8}$ Torr during deposition.

The rf-magnetron sputtering technique was used to grow both YSZ and $CeO_2$ layers on e-beam grown $Y_2O_3$-buffered Ni-W substrates at 780ºC and 10 mTorr of Ar/$H_2$ (4%) gas. The plasma power was 75 W at 13.56 MHz. Ex situ YBCO precursors were deposited on $CeO_2$-buffered YSZ/$Y_2O_3$/Ni-W substrates using e-beam co-evaporation of Y, $BaF_2$, and Cu.

The $CeO_2$-buffered YSZ/$Y_2O_3$/Ni-W substrates were annealed under $N_2$ at 650ºC for 1 h prior to the YBCO precursor deposition. The YBCO precursor films were shiny, brown-black in color, and stable in air. The YBCO film thickness was close to 3200 Å. The YBCO precursor films were heated to 100ºC in a three-zone furnace under linear gas flow conditions, first in flowing Ar gas and then switched to $H_2O$ with a dew point of approximately 40ºC and an oxygen partial pressure ($pO_2$) of of 180 ppm while heating to 730ºC. The $H_2O$ dew point of 40ºC corresponds approximately to an $H_2O$ partial pressure of 55 Torr. The low-$pO_2$ gas atmosphere was prepared by mixing high-purity Ar gas with Ar/$O_2$ (2%) gas mixtures. The gas flow used was 2 to 4 L/min. The furnace was ramped to 730ºC in 15 min followed by slow ramp to 740ºC in another 5 min. The furnace was kept at 740ºC for 80 min. During the annealing process, wet gas was switched to dry gas after 50 min of reaction. The sample was then cooled to 500ºC in 20 min and switched from low-$pO_2$ to pure 1-atm $O_2$. The film was kept at 500ºC for 30 min in $O_2$ before furnace cooling to room temperature. The high-temperature anneal under wet conditions resulted in the conversion of the Y, $BaF_2$, and Cu into $YBa_2Cu_3O_{7-y}$.

The films were analyzed by XRD techniques. A Philips model XRG3100 diffractometer with Cu $K_\alpha$ radiation was used to record powder-diffraction patterns. A Picker four-circle diffractometer was used to determine the texture of the films by omega and phi scans. Pole figures were collected for all the layers to determine whether the film had a single cube texture. SEM micrographs were taken using a Hitachi S-4100 field emission microscope. The thicknesses of both the buffers and the YBCO films were determined by both RBS and alpha-step profilometer scans. The resistivity and transport critical current density, $J_c$, were measured using a standard four-probe technique. The voltage contact spacing was 0.4 cm. Values of $J_c$ were calculated using a 1-μV/cm criterion.

A typical θ-2θ scan for a 500-Å-thick $Y_2O_3$ film on a Ni-W (100) substrate is shown in Fig. 1.65. The strong $Y_2O_3$ (004) signal revealed the presence of a good out-of-plane texture. The ω and ϕ scans on the same film indicated the presence of a single in-plane and out-of-plane texture as well. From the XRD results, it can be concluded that $Y_2O_3$ can be grown epitaxially on {100}<001> Ni-W substrates. An SEM micrograph for a 500-Å-thick $Y_2O_3$ film on Ni-W (100) substrate is shown in Fig. 1.66. As can be seen

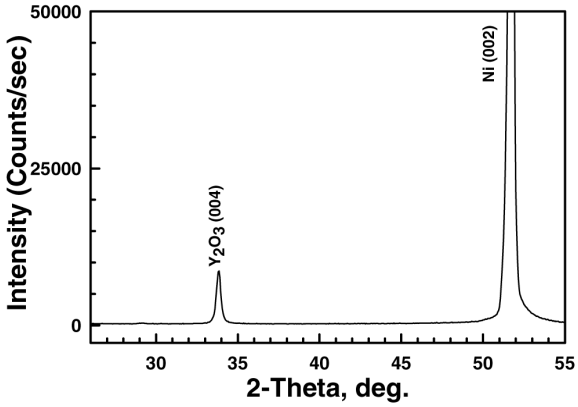


**Fig. 1.65. A typical θ-2θ scan for a 500-Å-thick $Y_2O_3$ film on Ni-W (100) substrates.**

from the SEM micrograph, the $Y_2O_3$ films were crack-free and continuous. Also, the XRD results indicated the presence of a highly aligned sputtered YSZ and $CeO_2$ layers. In addition, both sputtered YSZ and $CeO_2$ had dense microstructures.

A typical θ-2θ scan for a 3200-Å-thick YBCO film is shown in Fig. 1.67. Figure 1.67 indicates the presence of *c*-axis-aligned films. A small impurity peak at approximately 28.7°, which belongs to $BaCeO_3$, indicates that there is some interaction between the $CeO_2$ layer and YBCO. A small amount of NiO was also observed in the film. As shown in Fig. 1.68, the XRD results from ω and ϕ scans revealed good epitaxial texturing. The FWHM values for Ni-W (002), YSZ (002), and YBCO (006) are 5.1, 5.6, and 4.4°, respectively, and those of Ni (111), YSZ (111), and YBCO (103) are 6.9, 7.8, and 8.3°, respectively.

Typical RBS spectra are shown in Fig. 1.69. The simulation studies indicate the Y:Ba:Cu stoichiometry to be 1.1:1.8:3.3. An SEM micrograph for the 3200-Å-thick YBCO film is shown in

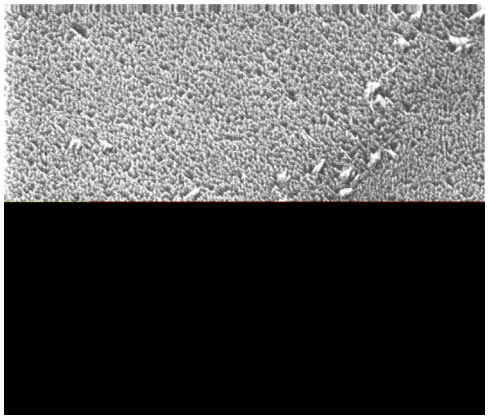

**Fig. 1.66. SEM micrograph for a 500-Å-thick $Y_2O_3$ film on Ni-W (100) substrates.**

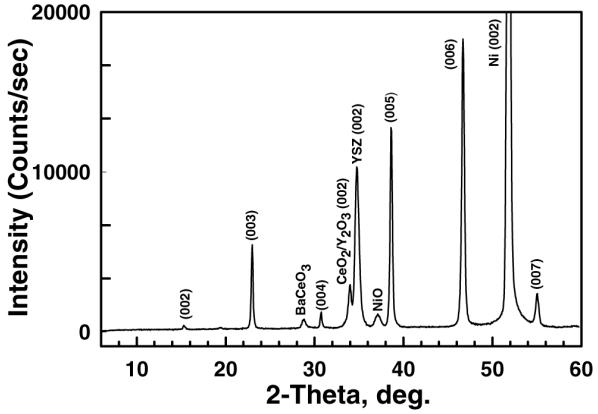


**Fig. 1.67. A typical θ-2θ scan for a 3200-Å-thick YBCO film on vacuum-buffered $CeO_2$/YSZ/ $Y_2O_3$/Ni-W substrates.**

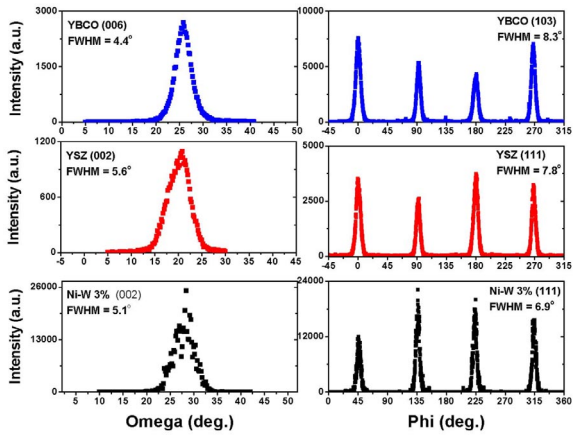


**Fig. 1.68. The ω and ϕ scans for a 3200-Å-thick YBCO film on vacuum-buffered $CeO_2$/ YSZ/$Y_2O_3$/Ni-W substrates.** The FWHM values for each scan are shown inside the scans.

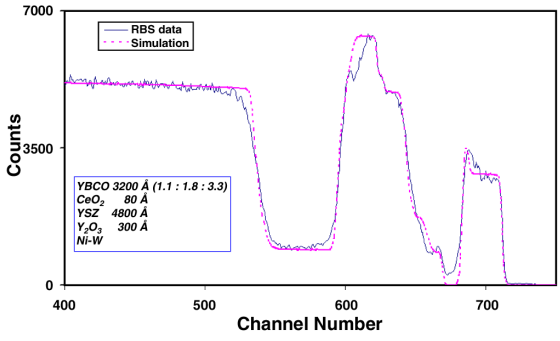


**Fig. 1.69 Rutherford backscattering spectra of a 3200-Å-thick e-beam co-evaporated YBCO precursor (Y, $BaF_2$, and Cu) on $CeO_2$ (80 Å) (sputtered)/YSZ (4800 Å) (sputtered)/$Y_2O_3$ (300 Å) (e-beam)/Ni-W (3 at. %) substrates.** The spectra were measured with 5.0-MeV He+ ions at near-normal incidence, detected at a 160° scattering angle.

Fig. 1.70. The microstructure of the YBCO film appears porous but with a platelike morphology. The field dependence of $J_c$ for the same film is shown in Fig. 1.71. The zero-field $I_c$ measured was 59.10 A, which translates to a $J_c$ of 1.9 MA/cm$^2$ at 77 K for a 3200-Å-thick YBCO film. $J_c$ at 0.5 T was about 21% of the zero-field $J_c$. This indicates the presence of a strongly linked YBCO film. The high-current performance of this film could be because of the better texture in the starting Ni-W substrate. In addition, buffers also transferred the texture all the way to the YBCO film. This resulted in better YBCO grain-to-grain connectivity. Efforts are under way to fabricate long lengths of similar YBCO-coated conductors using continuous reel-to-reel processing.

In summary, we have demonstrated the growth of high-quality YBCO films with a $J_c$ of 1.9 MA/cm$^2$ and an $I_c$ of 59 A/cm-width at 77 K and self-field on $CeO_2$/YSZ/$Y_2O_3$/Ni-W substrates. The $Y_2O_3$ seed layers were grown directly on Ni-W (3 at. %) substrates using reactive e-beam evaporation. The YSZ and $CeO_2$ layers were epitaxially grown on $Y_2O_3$-buffered Ni-W substrates using rf-magnetron sputtering. The YBCO films were also grown successfully on buffered-Ni-W substrates by the ex situ $BaF_2$ precursor process. It should be possible to scale up all the layers to produce long lengths.

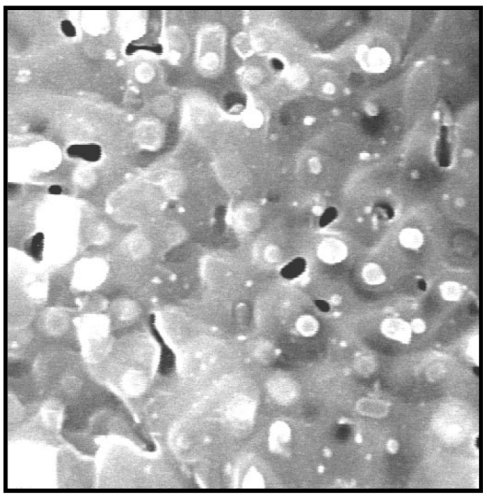


**Fig. 1.70. SEM micrograph for a 3200-Å-thick YBCO film on vacuum-buffered $CeO_2$/YSZ/$Y_2O_3$/Ni-W substrates.**

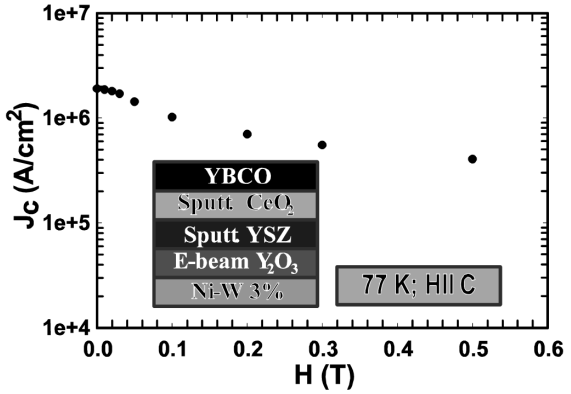


**Fig. 1.71. Field dependence of critical current density, $J_c$, for 3200-Å-thick YBCO film on vacuum-buffered $CeO_2$/YSZ/$Y_2O_3$/Ni-W substrates.** This film carried an $I_c$ of 59 A, which corresponds to a $J_c$ of 1.9 MA/cm$^2$ at 77 K and self-field.

## 1.9 CHEMICAL SOLUTION DEPOSITION OF LANTHANUM ZIRCONATE BUFFER LAYERS ON BIAXIALLY TEXTURED Ni-3 AT. % W ALLOY SUBSTRATES FOR COATED-CONDUCTOR FABRICATION

*S. Sathyamurthy, M. Paranthaman, and T. Aytug, B. W. Kang, P. M. Martin, A. Goyal, D. M. Kroeger, and D. K. Christen*

### 1.9.1 Introduction

Current trends in research and development in HTS are geared toward fabrication of YBCO-coated conductors. A coated conductor is defined as the superconductor deposited on a long-length textured substrate. The different stages involved in coated-conductor fabrication are (a) development of long

lengths of flexible metal substrate, (b) deposition of textured buffer layers that act as a crystallographic template for further growth of the HTS film while preventing the diffusion of the metal from the substrate to the HTS film, and (c) deposition of the HTS film. To fabricate coated conductors in long lengths, it is imperative that the processing techniques used in each stage be scalable. Chemical solution deposition techniques have proven to be a viable, low-cost nonvacuum process for coating long lengths. RABiTS™ are ideal templates for the solution process. Solution precursors can be used for processing both buffer layers and superconductor films. Typically in this process, the substrates are coated with a metallorganic precursor solution at room temperature and are then annealed at high temperature to obtain highly crystalline phases. The main advantage of using solution precursors is the ease with which precursor stoichiometry can be controlled.

Early attempts to grow epitaxial buffer layers on textured Ni substrates by solution processing resulted in films with multiple orientations. We recently demonstrated the growth of $Gd_2O_3$ buffer layer by sol-gel process with single cube-on-cube epitaxy on textured nickel (100) substrate. The process has since been extended to other $RE_2O_3$ (rare-earth oxides; RE = Gd, Yb, and Eu), and critical current densities ($J_c$s) of about 1 MA/cm$^2$ have been demonstrated on textured Ni (100) substrates with a solution-processed seed layer and rf-sputtered YSZ and $CeO_2$ barrier layers. Notwithstanding these results, the cubic-to-monoclinic phase transition in most $RE_2O_3$ layers imparts some restrictions to the process window for the deposition of these buffer layers. Lanthanum zirconate (LZO) has a cubic pyrochlore structure stable up to 1500°C, and a close lattice match with YBCO offers a wider processing window.

We reported previously the processing of LZO films using a sol-gel chemistry similar to the one used for $RE_2O_3$. YBCO with a $J_c$ of 0.5 MA/cm$^2$ was reportedly being produced on textured nickel (100) substrate by using LZO films as seed layer and sputtered YSZ and $CeO_2$ films as barrier layers. In this work, we report successful growth of LZO buffer layers on textured Ni-3 at. % W alloy substrates using a continuous reel-to-reel dip-coating unit. We discuss the effect of the annealing conditions on microstructure and properties and demonstrate high-$J_c$ YBCO film on a sol-gel buffer layer capped with sputtered YSZ/$CeO_2$ barrier layers.

## 1.9.2 Experimental

### 1.9.2.1 Preparation of Coating Solution

Lanthanum isopropoxide (Alfa, La 40% assay), zirconium n-propoxide in n-propanol (Alfa, 70%), and 2-methoxyethanol (Alfa, spectrophotometric grade) were used as received. Lanthanum isopropoxide was handled in an argon-filled glove box, and the solution preparation was carried out under an argon atmosphere in a Schlenck-type apparatus. About 1.976 g (6.25 mmol) of lanthanum isopropoxide and 2.925 g (6.25 mmol) of zirconium n-propoxide were dissolved in 50 mL of 2-methoxyethanol in a 250-mL round-bottom flask. The solution was refluxed in excess 2-methoxyethanol to get lanthanum and zirconium methoxyethoxides. The isopropanol formed during the exchange reaction was distilled out along with the excess 2-methoxyethanol, and the final concentration of the solution was adjusted to 0.25 M total cations.

### 1.9.2.2 Preparation of Ni-3 at.% W Substrates

The Ni-W tapes were fabricated by cold-rolling to total deformations greater than 98%. The details of this process have been reported earlier. The substrates were then cleaned by ultrasonication in isopropanol for 1 h, followed by a recrystallization anneal at 1300°C for 1 h in Ar/$H_2$ (4%) atmosphere to obtain the desired cube-textured (100) Ni-W substrates.

### 1.9.2.3 Reel-to-Reel Dip-Coating

A schematic diagram of the reel-to-reel dip-coater is illustrated in Fig. 1.72. The annealed Ni-W tape was electrically spot-welded to nickel leaders mounted on two reels. The tapes were drawn out of the coating bath at a constant coating speed. The tapes were then crystallized at a given annealing speed in a furnace, which had been preheated to 1100°C and purged with flowing Ar-4% $H_2$. In this study, the coating speed, annealing speed, and process atmosphere were varied, and their influence on the microstructure and properties of the film were studied.

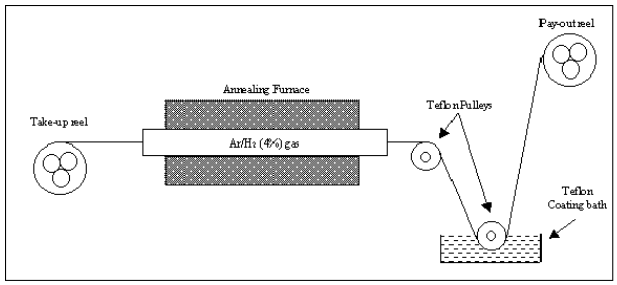


**Fig. 1.72. Schematic illustration of the reel-to-reel continuous dip-coating unit.**

### 1.9.2.4 Characterization

The LZO layers were characterized by XRD for phase purity and texture, SEM for homogeneity and microstructure, and RBS for composition and carbon analysis. A Philips XRG3100 diffractometer with Cu-$K_\alpha$ radiation was used to record θ-2θ XRD patterns. The texture analysis was performed with a Picker 4-circle diffractometer. The microstructural analysis of these samples was performed with a Hitachi S-4100 SEM with a field-emission gun. The thickness, composition, and carbon analyses were performed by RBS, using 5-MeV $He^{2+}$ ions at near normal incidence detected at a 160° scattering angle.

### 1.9.2.5 Superconducting Test Structures

The superconducting test structure with a layering sequence of YBCO/$CeO_2$/YSZ/LZO/Ni-W was prepared by using the LZO-seeded Ni-W substrates. A 200-nm-thick YSZ layer and 10-nm-thick $CeO_2$ cap layer were deposited by rf-magnetron sputtering on the LZO-seeded Ni-W substrates at 780°C in 10 mTorr of Ar/$H_2$ (4%) gas and a water pressure of $2 \times 10^{-6}$ Torr. The plasma power was 75 W at 13.56 MHz. The YBCO was deposited by PLD at 790°C in 120 mTorr oxygen with an average laser energy of 400 to 410 mJ, followed by annealing under 550 Torr oxygen during cooldown. The samples were then prepared for current density measurements by depositing silver for current and voltage leads, followed by oxygen annealing at 500°C for 1 h. Resistivity and transport $J_c$ were measured by means of a standard four-point probe technique.

## 1.9.3 Results and Discussion

The coating speed, annealing speed, and the atmosphere were varied during the LZO dip-coating. Four coating speeds (20, 80, 300, and 1000 cm/h) were used along with four annealing speeds (10, 30, 40, and 60 cm/h), and the process atmosphere was varied between dry and wet Ar-4% $H_2$ gas. The effect of these variables on the properties of the LZO film are discussed in the following sections.

### 1.9.3.1 X-Ray Studies

A typical θ-2θ scan for a dip-coated LZO film on textured Ni-3 at. % W (100) substrate is shown in Fig. 1.73. The strong LZO (004) signal reveals the presence of a *c*-axis-aligned film. Typical ω and ϕ scans of these films along with those of the Ni-3 at. % W (100) substrates are shown in Fig. 1.74.

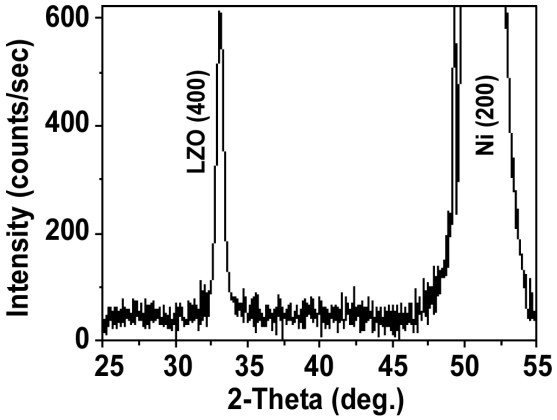


**Fig. 1.73. Typical θ-2θ scan for dip-coated LZO film on textured Ni-3 at. % W (100) substrate.**

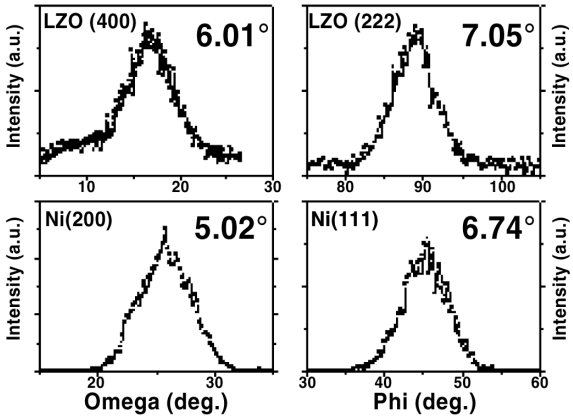


**Fig. 1.74. Typical ω and ϕ scans for dip-coated LZO film on textured Ni-3 at. % W (100) substrate.**

FWHMs of 6.01° and 7.05° for the LZO and 5.02° and 6.74° for the Ni-3 at. % W substrate were obtained for the ω and the ϕ scans, respectively. The variation of the texture of these samples with the coating and annealing speeds is shown in Fig. 1.75, where in-plane and out-of-plane textures of the LZO films have been normalized with that of the Ni-3 at. % W (100) substrate and plotted against coating and annealing speed. It is evident from this figure that the variations in coating and annealing speeds within the range of these experiments do not show a significant effect on the texture of the seed layers.

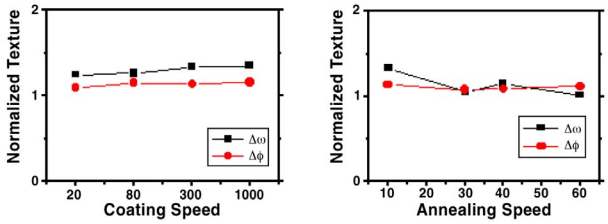


**Fig. 1.75. (a) Effect of coating speed on normalized texture of LZO film. (b) Effect of annealing speed on normalized texture of LZO film.** (Normalized texture = texture of LZO/texture of Ni-3 at. % W.)

### 1.9.3.2 Microstructure

Variations in microstructures were monitored for the three process variables studied (the coating speed, the annealing speed, and the process atmosphere). In the dip-coating process, as the coating rate increases, the thickness of the film increases. The variation of the microstructure with the coating speed is illustrated in Fig. 1.76. As the coating rate was increased from 20 cm/h through 80 cm/h to 300 cm/h, the microstructure showed signs of increasing densification and decreasing porosity. However, the grain size of the LZO films did not show a significant change.

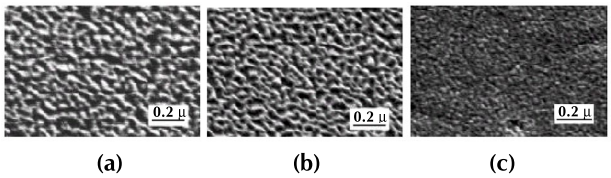


**Fig. 1.76. Variation of SEM microstructure of dip-coated LZO buffer layer with coating rate.** (a) Coating rate = 20 cm/h, (b) coating rate = 80 cm/h, and (c) coating rate = 300 cm/h.

Unlike the effect of the coating rate, the effect of the annealing rate on the microstructure was found to be minimal within the range of these experiments. The samples processed with various annealing rates did not show any significant variation in grain size or porosity. The most dramatic change in

microstructure was observed by changing the process atmosphere from dry Ar-4% $H_2$ to wet Ar-4% $H_2$ gas. The grain size of the LZO film, which was less than 20 nm for films processed in dry Ar-4% $H_2$, increased to greater than 100 nm when moisture was introduced into the furnace. Coupled with the increase in grain size, an increase in porosity was also observed. These effects are illustrated in Fig. 1.77. In the presence of oxygen in the form of moisture, the stability of the crystalline LZO phase is enhanced. This would cause the nucleation and growth of LZO from the amorphous coating to start much earlier during the annealing and hence would lead to a larger grain size. One aftermath of such a microstructure was that the YSZ/$CeO_2$ subsequently deposited on the LZO seed layers were randomly oriented. This is illustrated in Fig. 1.78, where the XRD patterns of two samples processed with the same coating speed (300 cm/h) and annealing speed (30 cm/h) in dry and wet Ar-4% $H_2$ atmospheres are compared. Figure 1.78 suggests that in these ranges of coating speed, annealing speed, and temperature, a dry Ar-4% $H_2$ atmosphere gives better films.

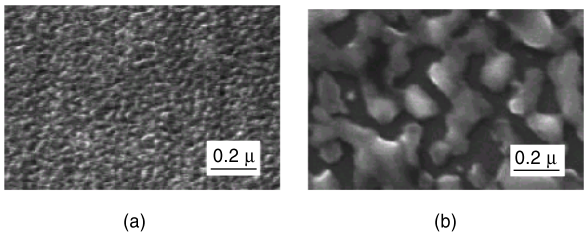


**Fig. 1.77. Effect of moisture on the microstructure of the dip-coated LZO buffer layer. (a) LZO seed layer processed in dry Ar-4%$H_2$. (b) LZO seed layer processed in wet Ar-4%$H_2$.**

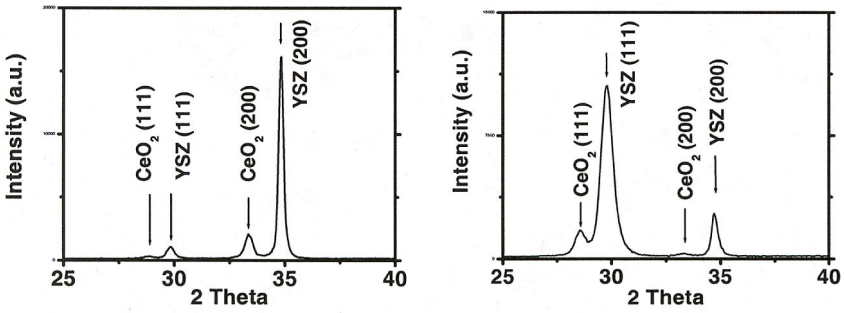


**Fig. 1.78. Effect of moisture illustrated by XRD patterns of YSZ/$CeO_2$ deposited on LZO seed layers.**

### 1.9.3.3 Film Thickness and Composition Analysis

The thickness and composition of the films were analyzed by using RBS. The thickness was found to vary as a function of the coating rate from 10 nm for 20 cm/h to 60 nm for 1000 cm/h. All the samples were found to have a La:Zr stoichiometry of about 1:1. The presence of carbon in the annealed film was also monitored qualitatively by using the intensity of the carbon peak in the $He^{2+}$ RBS spectra. It has been observed in the case of $RE_2O_3$ seed layers that the presence of carbon in the seed layer has a deleterious effect on the ability of these films to support epitaxial YSZ/$CeO_2$ layers. Therefore, it was essential to monitor the carbon content in the film. An increase in carbon content with increasing coating speed, as illustrated in Fig. 1.79, has been observed. This is most

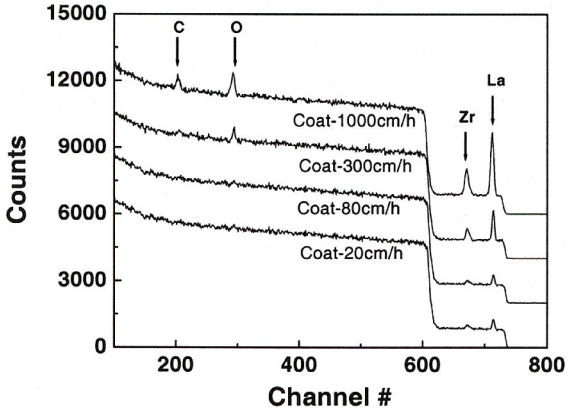


**Fig. 1.79. Effect of coating speed of LZO films on the carbon content.**

likely because of the increased thickness of the films coated at higher speeds. In Fig. 1.79, RBS spectra of four samples processed at different coating speeds, all annealed at 10 cm/h at 1100°C, have been plotted. It can be seen that very thin films (coated at 20 cm/h or 80 cm/h) are essentially carbon-free while thicker films (coated at 300 cm/h or 1000 cm/h) have retained a significant amount of carbon. Increasing annealing speed also seems to increase the carbon content in the LZO films, as illustrated in Fig. 1.80. RBS spectra of four samples, all coated at 300 cm/h and annealed at different annealing speeds at 1100°C, have been plotted. An increase in annealing speed constitutes a decrease in residence time at the crystallization temperature and hence could contribute to an increase in carbon retention in the film. The effect of moisture on the carbon content is illustrated in Fig. 1.81. In this figure, samples coated at 300 cm/h and annealed at 40 cm/h and 60 cm/h, in dry and wet Ar-4% $H_2$ atmospheres, are compared. It can be seen that for both annealing rates, the use of moisture eliminates all carbon. In the presence of oxygen in the form of moisture, it is easier to burn off all carbon from the film and hence, all the films processed in a wet Ar-4% $H_2$ atmosphere have essentially no retained carbon.

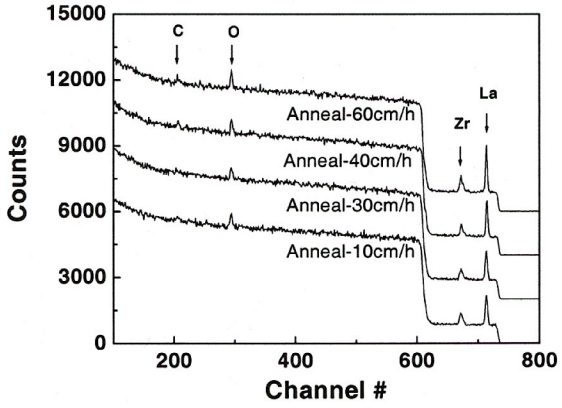


**Fig. 1.80. Effect of annealing speed of LZO film on carbon content.**

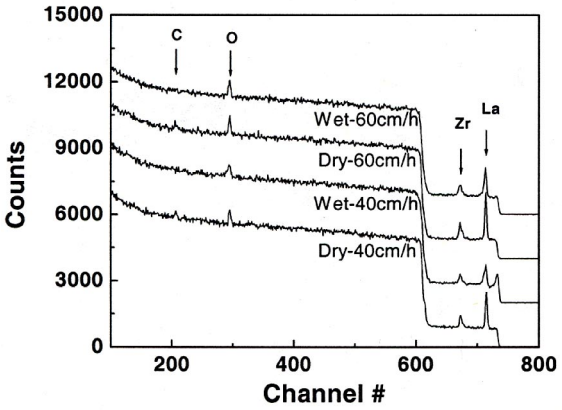


**Fig. 1.81. Effect of moisture on retained carbon in dip-coated LZO films.**

### 1.9.3.4 Superconducting Test Structures

Substrates for YBCO deposition were prepared by using rf sputtering to deposit YSZ/$CeO_2$ on the dip-coated LZO films. Typical XRD patterns obtained from these films are shown in Fig. 1.78(a). The extent of in-plane and out-of-plane texturing across these layers was characterized by ω- and ϕ- scans. These results, summarized in Fig. 1.82, show that the FWHM of the out-of-plane texture (ω-scan) varies (5.0° for Ni-3 at. % W, 6.0° for LZO, 5.0° for YSZ, and 5.2° for $CeO_2$) and that the in-plane texture varies (6.7° for Ni-3 at. % W, 7.1° for LZO, 7.2° for YSZ, and 7.2° for $CeO_2$). YBCO films, 200 nm thick, were deposited on these textured substrates by PLD. X-ray diffraction patterns obtained from these YBCO films showed that the YBCO film has a strong *c*-axis texture. The XRD pattern also reveals the presence of a small amount of nickel oxide in the sample. The out-of-plane and in-plane textures for a typical YBCO film, also shown in Fig. 1.82, were found to be about 5.9° and 8.2°, respectively. Transport measurements on these films showed that the $I_c$ of samples processed on various LZO seed layers ranged from about 10 A to 19 A at 77 K in self-field. This translates to a $J_c$ of 1 to 1.9 MA/cm$^2$. The field dependence of all the samples was found to be similar. However, the variation in the $J_c$ did not show a clear trend with variation in the LZO processing conditions, as illustrated in Fig. 1.83. In this figure, the field dependence of the critical current density of various samples with different coating and annealing speeds for the LZO seed layer is plotted, and it shows the presence of strongly linked YBCO films. Field

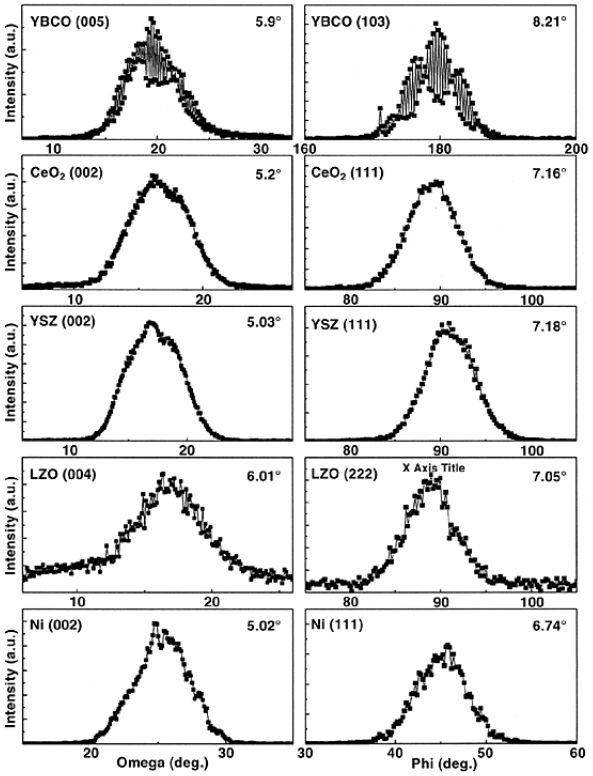


**Fig. 1.82. Omega and phi scans for the various layers, namely Ni-3 at. % W, LZO, YSZ, and $CeO_2$ in the substrate, along with that of the YBCO deposited by PLD.**

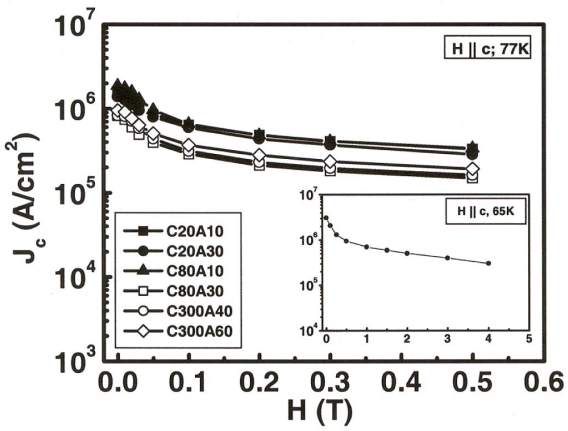


**Fig. 1.83. Field dependence of $J_c$ for YBCO samples deposited on $CeO_2$/YSZ/LZO/Ni-3 at. % W substrates for various coating and annealing speeds used in LZO processing.** (Legend: C = Coating Speed in cm/h, A = Annealing speed in cm/h.) Inset: Field performance of YBCO sample deposited on $CeO_2$/YSZ/LZO/Ni-3 at. % W at 65 K.

dependence of these samples for higher fields at 65 K, measured across a 2-mm bridge in the sample, is shown in the inset in Fig. 1.83. A self-field $J_c$ of more than 3 MA/cm$^2$ and a $J_c$ greater than 0.5 MA/cm$^2$ at 2 T were measured at 65 K. The performance of solution seed layers is comparable to that of vacuum seed layers. From these results, it can be concluded that dip-coated LZO layers act as good seed layers for coated-conductor processing. Currently, efforts are being made to extend this process to long lengths and to produce meter lengths of high-current YBCO coated conductors.

### 1.9.4 Conclusions

We have demonstrated that epitaxial LZO buffer layers can be grown on textured Ni-3 at. % W substrates in a continuous reel-to-reel dip-coating unit. The effects of processing conditions on the properties of these solution buffer layers have been studied. If moderate coating speeds and annealing speeds are used, the microstructure and the carbon content of the films can be kept under control and useful buffer layers can be processed. On these dip-coated LZO films, epitaxial YSZ/$CeO_2$ layers were deposited using rf-magnetron sputtering. High-quality YBCO films that have a $J_c$ of 1.9 MA/cm$^2$ at 77 K and self-field have been processed on these substrates by PLD. The properties of these films approach those of the best YBCO processed on vacuum-deposited buffer layers.

# 1.10 GROWTH OF COMPOSITIONALLY MIXED AND COMPOSITIONALLY GRADED FILMS BY PLD

*H. M. Christen, H. Y. Zhai, and D. H. Lowndes, ORNL; J. Wen, Boston College*

## 1.10.1 Introduction

The development of new and improved buffer layers depends to a large extent on a rapid, efficient prototyping method to produce such layers of various chemical compositions. PLD, even if not envisioned as the ultimate fabrication method, plays a significant role in this research because of the inherent flexibility of the approach.

Conventional PLD relies on the fabrication of a ceramic target of a certain composition, from which a thin film is then grown. In this research, we present an approach that can be used to efficiently fabricate thin films of alloy buffer layers, such as "solid solutions" of oxides, without requiring a target of each composition. Particular examples are perovskite materials and the alloys of the type $A^{(1)}_{x}A^{(2)}_{1-x}BO_3$ and $AB^{(1)}_{y}B^{(2)}_{1-y}O_3$. Research into such mixed oxides is motivated by observations such as the fact that PLD-grown $SrTiO_3$ appears to nucleate nicely on sulfur-terminated nickel tapes, whereas the isostructural $SrRuO_3$ is much more difficult to obtain. Unfortunately, $SrTiO_3$ provides an insufficient oxygen diffusion barrier for thin films, unlike $SrRuO_3$. The $SrTi_yRu_{1-y}O_3$ alloy can be synthesized in bulk only for values of y close to 0 or 1, but this research demonstrates that thin films of metastable mixed phases can be obtained.

It is not clear whether there exists a stable or metastable alloy between $SrRuO_3$ and $SrTiO_3$ that may serve as a single buffer layer on Ni, or whether other perovskite-type alloys may be more useful than many of the currently explored materials. It is, however, the first goal of this research to develop a technique that can rapidly produce such alloys of arbitrary composition based on ceramic targets of only the end members.

The development of such a technique immediately enables the fabrication of much more interesting, unusual layers, namely thin films in which the chemical composition varies in the growth direction. For example, a layer of $SrTiO_3$ could be nucleated first onto a Ni tape, and then the composition could gradually change to the more desirable $SrRuO_3$. While this is somewhat similar to the growth of bilayers, it offers much more flexibility in choosing the appropriate composition gradient that may be less prone to defect formation at the interface and in fact can even lead to defect termination within the graded material, as we will show subsequently.

Once again, PLD cannot be the method of choice for the fabrication of such advanced structures. Techniques such as co-sputtering from two sources onto a moving tape or dip-coating with various precursors followed by an anneal to promote partial interdiffusion are much more promising for long-length applications. The advantage of the presented PLD-based approach is the ease by which the composition profile can be chosen and tailored, and the control that can be exercised over the entire process.

## 1.10.2 Compositionally Mixed Films by Sequential Deposition of Sub-Monolayer Amounts

Repeated deposition of less than a monolayer of one material followed by the deposition of less than a monolayer of a second material results in an intimate intermixing of these two constituents and to the formation of a homogeneous alloy, as has been shown previously in the growth of $KTa_xNb_{1-x}O_3$ films from a segmented target (consisting of $KTaO_3$ and $KNbO_3$ "wedges")[1] and in laterally compositional-spread layers.[2] The requirement for rapid growth of films by this method is the rapid exchange of targets

between laser pulses. Contrary to the traditional "point-and-shoot" approach, we introduced a method of synchronizing the laser firing with a continuously moving target exchange mechanism.

In our growth geometry, each laser pulse deposits approximately 0.15 Å of material for a typical perovskite, such as $SrTiO_3$ or $BaTiO_3$. With a unit cell of almost 4 Å, 26 laser pulses are required for the growth of a single unit cell of the material. Our mixing approach uses an algorithm that limits the number of laser pulses fired onto one target to four pulses before deposition of the second material. Clearly, this results in a discrete number of compositions that are accessible. In the test system $Ba_xSr_{1-x}TiO_3$, for example, the smallest accessible value of x corresponds to 1 pulse of $BaTiO_3$ for 25 pulses of $SrTiO_3$ (i.e., $x = 0.04$, and the largest value of $x$ similarly is $x = 0.96$). There are, however, 213 total compositions accessible between 0.04 and 0.96.

At a target carousel rotation of one revolution per second, the target spends about 0.1 s at the focal point of the laser beam. Using a burst at 100 Hz, four pulses can easily be fired onto the moving target. Thus film growth at an equivalent average repetition rate of eight pulses per second can be achieved using two targets. (The use of four targets would double that deposition rate.)

To test the method, layers of various composition of $Ba_xSr_{1-x}TiO_3$ were grown onto $LaAlO_3$ and MgO substrates. Figure 1.84 shows an X-ray θ-2θ scan for trilayers consisting of three layers with differing values of $x$. Figure 1.85 shows a cross-section transmission electron microscopy image of the same structure.

Films of the composition $SrRu_xTi_{1-x}O_3$ were also grown by this method and are currently being characterized for their physical and structural properties.

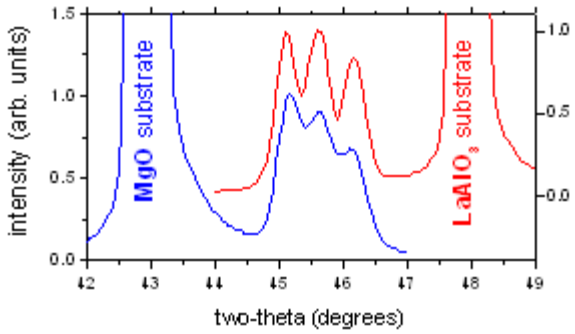


**Fig. 1.84. X-ray θ-2θ scan of $Ba_xSr_{1-x}TiO_3$ trilayers grown onto MgO and $LaAlO_3$ substrates.**

## 1.10.3 Compositionally Graded Films

It is clearly a straightforward generalization of the approach described previously to continuously vary the composition during the growth progress. Linear profiles have been grown exclusively at this point [i.e., films with composition $Ba_{x(h)}Sr_{1-x(h)}TiO_3$, where $h$ is the distance from the film-substrate interface and $x(h) = \alpha + \beta h$], even though the approach could easily be modified to alternative profiles. (The control software simply reads a spreadsheet file containing the description of the desired growth profile.) Profiles with the composition varying linearly from $x = 0.2$ to $x = 0.8$ (so-called "up" gradients) and varying linearly from $x = 0.8$ to $x = 0.2$ ("down" gradients) were grown onto $LaAlO_3$ and MgO substrates (see Fig. 1.86).

The most important factor in the physical properties of these films is the large lattice mismatch between the end-members of the alloy. Assuming, for simplicity, that $BaTiO_3$ can be approximately described as a cubic material, we have $a(SrTiO_3) = 3.905$ Å and $a(BaTiO_3) = 3.994$ Å. Films with opposite composition gradient exhibit significantly different X-ray peaks, even though they are chemically identical, while the influence of the substrate is in fact rather weak.

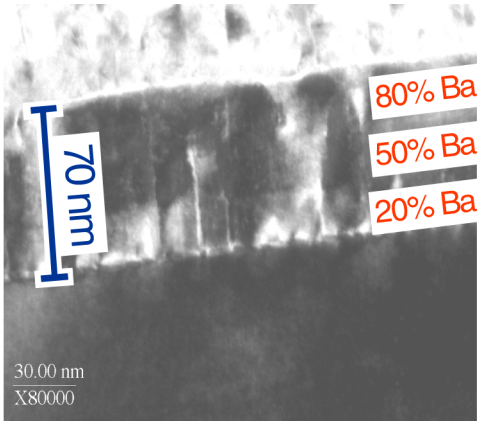


**Fig. 1.85. Scanning transmission micrograph of a $Ba_xSr_{1-x}TiO_3$ trilayer on $LaAlO_3$.**

Figure 1.87 illustrates the reason for the almost bulk-like, relaxed crystal structure of the down-gradient films. In these films, the tensile strain (resulting from within the film, not the substrate) gradually increases with distance from the substrate, and this strain can easily be relieved by the formation of cracks and voids. This leads to a film that appears reasonably strain-relieved in the X-ray scans but that obviously has little use in buffer-layer applications.

The situation in up-gradient films, however, is quite different. Figure 1.88 shows the remarkable phenomenon of defect termination within the film. A similar effect was reported previously in strained $Si_xGe_{1-x}$ layers on Si substrates,[3] but to the best of the author's knowledge, this is the first report of such a phenomenon in perovskites. In addition, the earlier reported $Si_xGe_{1-x}$ films are nucleated on Si with an initial composition of $x = 0$, and thus with no nominal lattice mismatch at the film-substrate interface. In the case of the $Ba_xSr_{1-x}TiO_3$ on $LaAlO_3$, the initial lattice mismatch between the film ($a = 3.931$ Å) and the substrate ($a = 3.792$ Å) is more than 3.5%, leading to the large number of defects visible at the film-substrate interface in Fig. 1.88.

When $Ba_{0.8}Sr_{0.2}TiO_3$ ($a = 3.971$ Å) is nucleated directly on $LaAlO_3$ (as in the case of the down-gradient of Fig. 1.87), a large number of defects is formed at the film-substrate interface. In the case of a simple film growth, one would therefore expect a $Ba_{0.8}Sr_{0.2}TiO_3$ film on $LaAlO_3$ to be rather defective. As is clearly evidenced in Fig. 1.88, however, the present method allows us to grow a final composition of $Ba_{0.8}Sr_{0.2}TiO_3$ with comparatively few defects in a graded structure.

Finally, let us present a crude model that is qualitatively sufficient to explain the data presented in Fig. 1.86. A simple forward calculation can be performed by making the assumption that a graded film consists of a finite number of imaginary layers with fixed composition and that each of these imaginary layers diffracts X rays in the same way that a thick slab of material would. This obviously ignores some broadening that will be associated with very steep gradients. Furthermore, we assume that the structure factor is independent of the composition, an obvious oversimplification that leads to calculated curve shapes that may be significantly distorted. Our model thus simply adds up Lorentzian line shapes (assuming a line width of 0.35°) associated with the various normal lattice parameters encountered in the film (ignoring furthermore that layers deeper in the

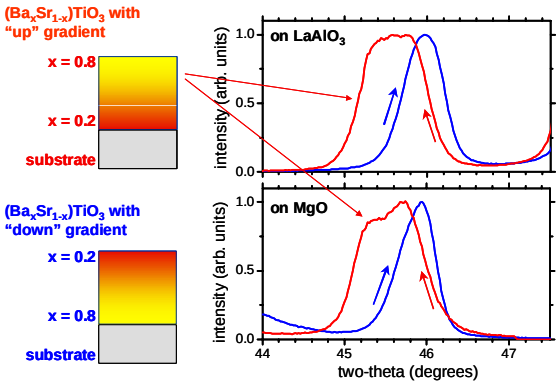


**Fig. 1.86. X-ray θ-2θ scans of compositionally graded films on $LaAlO_3$ and MgO single crystal substrates.** The up-gradient material shows a significantly broadened X-ray diffraction peak, whereas the down-gradient structure exhibits properties more similar to those expected from the bulk values of $SrTiO_3$ and $BaTiO_3$. This difference between these two types of chemically identical films illustrates the importance of the strain and defect evolution.

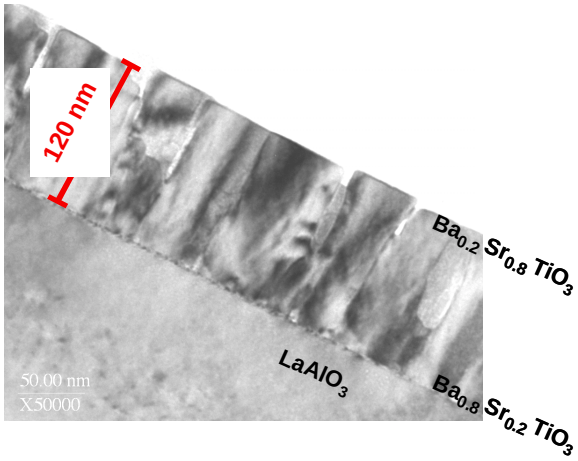


**Fig. 1.87. Defect evolution in a "down"-gradient $Ba_xSr_{1-x}TiO_3$ film on $LaAlO_3$.** As the film grows, the tensile strain (resulting from within the film, not the substrate) gradually increases, leading to the formation of cracks and voids.

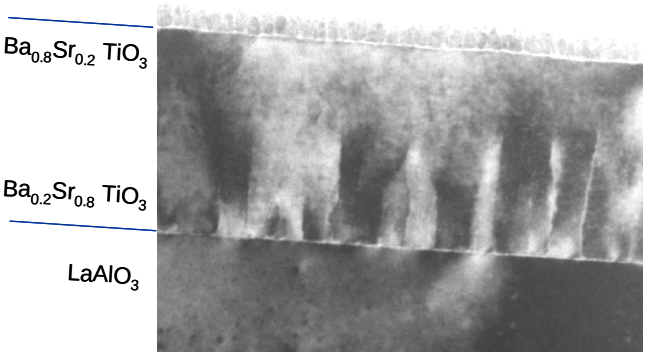


**Fig. 1.88. Defect termination in up-gradient $Ba_xSr_{1-x}TiO_3$ films on $LaAlO_3$.** In these films, points farther from the substrate experience a larger compressive strain because of the changing composition, resulting in a microstructure that is fundamentally different from that of the chemically identical film in Fig. 1.87.

structure will see a weaker X-ray signal than those at the surface).

For the calculation of the lattice parameter at each point in the structure, we assume that all distortions are tetragonal (i.e., that the material has in-plane lattice parameters $a = b$). We also assume that the volume per formula unit is independent of the strain (i.e., that $a \times b \times c = c_0^3$; this is equivalent to assuming a Poisson ratio of 0.5) and that $c_0$ depends only on the composition, and thus on the height z as measured from the film/substrate interface: $c_0 = c_0(z)$.

From the observation that the X-ray data appear very similar for $LaAlO_3$ substrates ($a$ = 3.792 Å) and for MgO substrates ($a$ = 4.213 Å), we can assume that the nucleation of the first few monolayers results in a completely relaxed structure, effectively erasing the memory of the substrate's lattice parameter for the rest of the film growth.

Finally, we pose that the strain relaxation at each point follows the relation

$$a(z + dz) = a(z) + z_0^{-1} \{c_0(z) - a(z)\}\, dz\,, \qquad (1.2)$$

where $z_0$ is a strain relaxation depth. For a film with constant composition ($c_0 = const.$), Eq. (1.2) leads to an exponential relaxation of the lattice parameter toward the bulk value. Assuming $z_0 = 0$ for the down gradients ($x$ = 0.8 → 0.2) and $z_0$ = 70 nm for the up gradients ($x$ = 0.2 → 0.8) with a total film thickness of 120 nm, a very satisfactory agreement between the observed and calculated X-ray scans is observed (Fig. 1.89). This holds even for the case of trilayers (containing films with $x$ = 0.2, 0.5, and 0.8). Note that the only parameters used for the calculation of all four curves are the lattice parameters of $BaTiO_3$ and $SrTiO_3$ and the two strain relaxation depths for up-gradient and down-gradient structures.

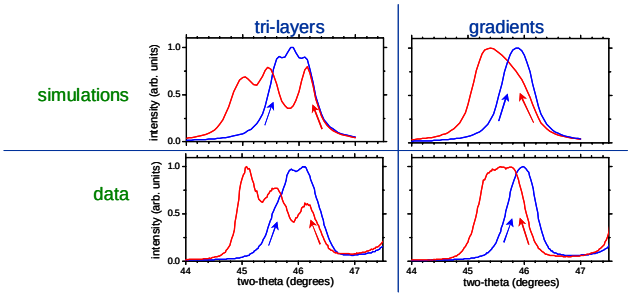


**Fig. 1.89. Comparison of simulated and measured X-ray θ-2θ scans for trilayers (left) and linear gradients (right).** Curves for up gradients and down gradients are shown in both cases. The only variable parameters for these four simulations are the strain relaxation depths for the up gradients ($z_0$ = 70 nm) and the down gradients ($z_0$ = 0 nm), and an experimental line width (0.35°). The qualitative agreement with the data is satisfactory, considering that no corrections have been made for intrinsic line broadening or varying structure factors.

## 1.10.4 Conclusions

Preliminary results have been presented on the growth of alloyed oxide layers and, more importantly, of compositionally graded oxide films. The evolution of the strain in these structures can readily be understood from a simplified elastic model. Gradient films in which the composition-induced strain is increasingly

tensile in the growth direction show degraded structural properties (i.e., rough surfaces, cracks, and voids). In contrast, films grown with an increasingly compressive strain exhibit a strong tendency for defect termination, resulting in dense, smooth films at the surface. To the best of the author's knowledge, such a "self-healing" mechanism has not been observed previously for oxide materials and is markedly different from the situation in the better-known strain-relieving graded $Si_xGe_{1-x}$ layers. Further work will focus on applying these mechanisms to buffer layers grown onto metallic tapes.

### 1.10.5 References

1. H. M. Christen, D. P. Norton, L. A. Géa, and L. A. Boatner, *Thin Solid Films* **312**, 156 (1998).
2. H. M. Christen, S. D. Silliman, and K. S. Harshavardhan, *Rev. Sci. Instrum.* **72**, 2673 (2001).
3. F. K. LeGoues, B. S. Meyerson, and J. F. Morar, Phys. *Rev. Lett.* **66**, 2903 (1991).

## 1.11 MAGNESIUM DIBORIDE: GROWTH MECHANISMS, REACTIVITY, AND RELATED ISSUES

*H. M. Christen, H. Y. Zhai, C. Cantoni, M. Paranthaman, L. Zhang, B. C. Sales, D. K. Christen, D. H. Lowndes, and A. Goyal*

### 1.11.1 Introduction

Within months of the first report of superconductivity in $MgB_2$, our group was able to synthesize thin films of this compound by both an ex situ reaction approach and a PLD-based in situ method. In this section, we summarize results related to the PLD growth of $MgB_2$, compare the properties of these films to those obtained by the ex situ approach, and show that $MgB_2$ decomposes readily when in contact with water. Isostructural $TiB_2$, which, unlike $MgB_2$, can be grown epitaxially by PLD, has been studied as a potential protective coating or as a seed layer for $MgB_2$

### 1.11.2 Pulsed Laser Deposition of Magnesium Diboride

Ideally, the goal of using PLD is to achieve the stoichiometric transfer of material from a solid target to a substrate. In compound materials having constituents with differing volatility, this may be difficult. $MgB_2$ is a particularly clear illustration of this point. In fact, at a substrate temperature of 400°C, Mg does not condense onto an oxide or silicon surface, and a Mg film deposited at room temperature evaporates almost immediately when heated to 500°C in vacuum. Therefore, simple PLD growth from a stoichiometric target is not likely to be successful at elevated substrate temperatures.

Various approaches can be used to compensate for a constituent's volatility in PLD, such as the use of nonstoichiometric (enriched) targets or the introduction of additional deposition sources (e.g., co-evaporation). In our first experiments, we used a segmented rotating target, which consisted of a half-disc of $MgB_2$ (obtained by either conventional sintering or by hot-pressing) and a half-disc of Mg. Target rotation and laser firing were chosen such that at most two pulses of the laser were fired onto the $MgB_2$ portion of the target before adding additional magnesium.

Both R-plane and C-plane $Al_2O_3$ substrates were used, but no superconductivity was observed in the as-grown films (deposition temperatures between 25 and 600°C). However, films deposited at room temperature could be annealed in situ at 600°C, which resulted in a transition temperature of about 23 K. As an additional precaution to avoid evaporative loss of Mg, the films were coated with a 100- to 500-nm-thick layer of Mg prior to the anneal.

During the anneal in ambient conditions of 0.7 atm of Ar/4% $H_2$ (in a chamber with a background pressure of about $10^{-6}$ torr), this magnesium layer evaporates and leaves a "skin" of MgO at the surface, as seen in Fig. 1.90(a).

In order to avoid the formation of such MgO skins, experiments were performed in which a stoichiometric precursor, deposited directly onto Si substrates, was annealed in vacuum at 630°C. Figure 1.90(b) shows an SEM image of such a sample. While some cracking and delamination can be observed, the film surface is comparatively smooth, and this film exhibited a $T_c \approx 24$ K. The optimal annealing temperature was measured by a thermocouple embedded into the heater block, onto which the sample was mounted with silver paint. The optimal temperature is slightly higher than that for the $Al_2O_3$ substrates with the Mg-rich precursors.

Both types of these PLD-derived films exhibit microstructures significantly different from those of the films reacted ex situ, where large (≥0.5-μm), hexagonal grains are usually observed. To determine the origin of the inhibited grain growth, stoichiometric PLD precursors were annealed in the same ex situ process described elsewhere in this report (for details, see Sect. 1.12). A modest increase in $T_c$ was observed ($T_c \approx 28$ K), but the grain growth was significantly inhibited compared those of the films reacted ex situ (where an e-beam-evaporated layer of boron served as a precursor to be reacted with Mg vapor).

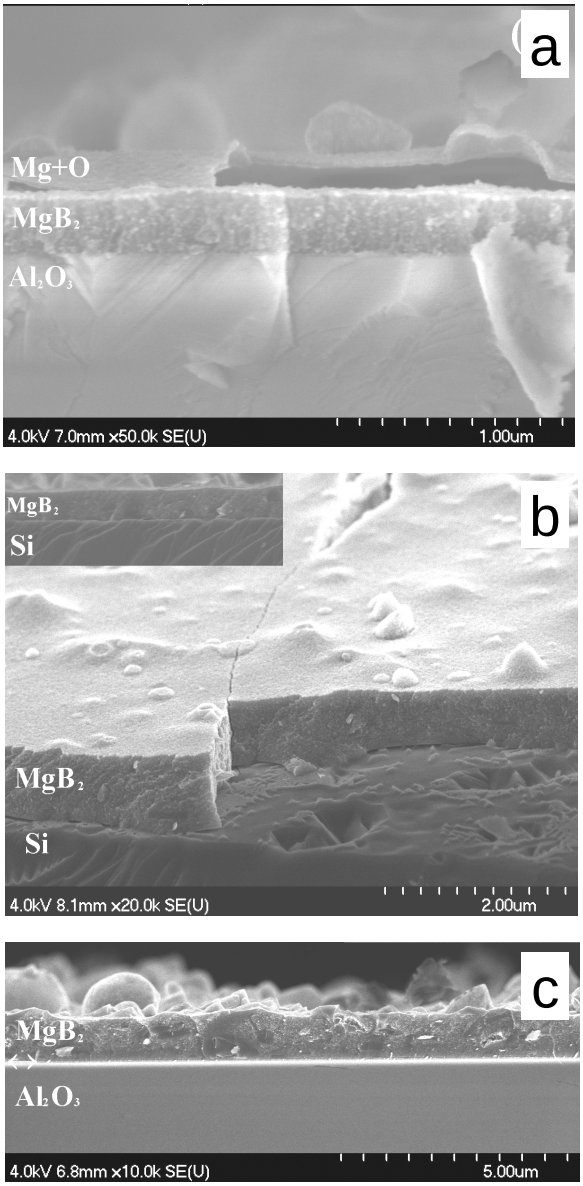


**Fig. 1.90. Scanning electron micrographs of $MgB_2$ films derived from PLD precursors.** (a) $MgB_2$ film on $Al_2O_3$ obtained by in situ annealing of a precursor grown from a segmented target and capped with a magnesium layer. (b) $MgB_2$ film on Si obtained by in situ annealing of a stoichiometric precursor. (c) Film morphology of a $MgB_2$ film obtained from a PLD precursor by an ex situ anneal at 900°C in the presence of excess Mg.

### 1.11.3 The Role of Oxygen Contamination

Clearly, the $MgB_2$ films derived from PLD precursors show significantly decreased $T_c$ and grain growth. Interestingly, results from energy dispersive spectroscopy (EDS) indicate that the PLD-derived films also contain a larger amount of oxygen than the ex situ films obtained from e-beam-evaporated boron.

Based on the preceding observations, we postulate that there is a causal relationship between the oxygen contamination, decreased $T_c$, and reduced grain growth in the PLD-derived films, even after additional ex situ anneals. The origin of the contamination appears to be twofold: oxygen contamination in the target material, and oxygen incorporation during film growth. First, the starting materials (both as $MgB_2$ or as Mg target) contain commercial-grade, high-purity magnesium. The purity of commercially available

metals, however, is specified for metal contaminants only. X-ray analysis showed a presence of several percent of MgO in the targets. Evaporative techniques (e-beam evaporation and ex situ reaction in Mg vapor) selectively use pure magnesium (low vaporization temperature) and thus eliminate some of the MgO (low vapor pressure) from the process. PLD is quite different in that the ablation process is approximately equally efficient for Mg and MgO (and any other contaminants).

The second pathway of oxygen incorporation into the PLD precursors is related to the high reactivity of the PLD plume. This plasma plume, which transports the material from the target to the substrate and travels through the background ambient of the vacuum system, contains Mg ions that likely react with oxygen or water vapors much more readily than thermal vapors.

Experiments were performed using the same targets in an ultrahigh vacuum system with a much lower background pressure and thus with a smaller amount of oxygen to be incorporated from the gas phase. The experiments resulted in films with only slightly enhanced values of $T_c$. This indicates that the MgO content in the target is the dominant source of oxygen contamination in the precursors.

While further experiments are needed to establish the causal relationship between the oxygen incorporation in the PLD process and the reduced grain growth and $T_c$-values, we believe that this may be the most significant limitation of the PLD approach. There currently appears to be some consensus in the scientific community that $MgB_2$ films with $T_c \approx 25$ K are in the "dirty limit" and that the films processed ex situ from boron precursors ($T_c \approx 39$ K) are in the "clean limit."

### 1.11.4 Effect of Exposure to Water

It is of paramount importance for practical commercial applications of $MgB_2$ to understand its behavior when in contact with moisture. To this end, a simple experiment was performed in which a sample of ex situ reacted $MgB_2$ on a $Al_2O_3$ substrate was immersed into deionized water at room temperature for various amounts of time.

As is shown in Fig. 1.91, the characteristics of the $R(T)$ curve change significantly. It is quite remarkable that a shoulder appears in the $R(T)$ curves at a temperature very similar to that of the $T_c$ of $MgB_2$ films derived from PLD precursors. Clearly, $MgB_2$ exhibits a very limited stability in the presence of water, and a possible explanation of the data in Fig. 1.91 is a change of the behavior of the material from the "clean limit" to the "dirty limit."

Based on this observation of rapid degradation of the superconducting properties of $MgB_2$ in contact with water, it is important to develop a chemically compatible cap-layer material that can be used to protect $MgB_2$.

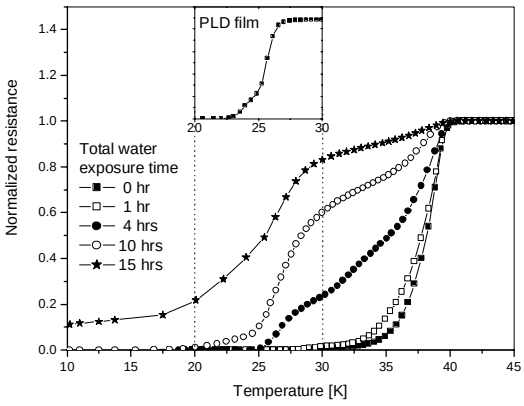


**Fig. 1.91. $R(T)$ curves measured on a $MgB_2$ film after various times of exposure to water at room temperature.** The $MgB_2$ film was obtained via the ex situ reaction of a boron film with magnesium. The inset shows a representative R(T) curve for a $MgB_2$ film obtained by the in situ anneal of a PLD precursor layer.

### 1.11.5 Epitaxial $TiB_2$ Films as Seed Layers and Protective Covers

The motivation for the growth of $TiB_2$ layers is twofold. First, the results of the study of the effects of exposure to water indicate the necessity of a protective cap layer for practical applications. Second, the epitaxial growth of $MgB_2$ films has not been obtained to date. Clearly, part of the reason for this is the high volatility that makes in situ growth difficult. However, a seed

layer with the correct type of chemical bonding may facilitate the nucleation of epitaxially aligned grains.

$TiB_2$ does not suffer from the high volatility of one of the constituents, and PLD growth at elevated temperature is in fact possible. Figure 1.92 shows an X-ray θ-2θ scan of an epitaxial $TiB_2$ film grown at 600°C on SiC. RHEED observations during growth indicate the in-plane alignment of $TiB_2$ with the substrate (data not shown). Studies characterizing the physical properties of these epitaxial films are currently being pursued.

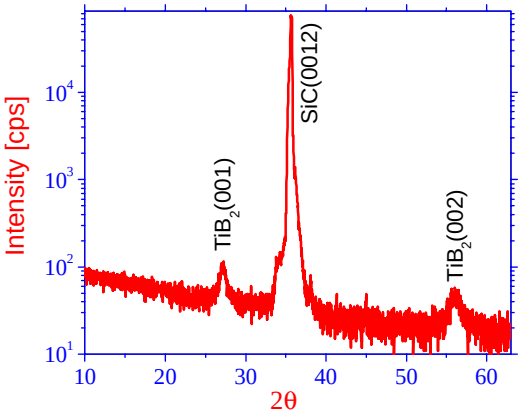


**Fig. 1.92. X-ray θ-2θ scan for an epitaxial, 100-nm-thick $TiB_2$ film on SiC.**

### 1.11.6 Conclusions

The studies related to the PLD growth of $MgB_2$, the effect of exposure to water, and the growth of epitaxial $TiB_2$ films shed light on a number of relevant aspects related to the potential use of $MgB_2$ in coated conductor applications.

First, it became obvious that, unlike the ex situ reaction of boron films, PLD may not be an appropriate method for the easy fabrication of $MgB_2$ without careful and potentially expensive modifications. Second, $MgB_2$ is sensitive to exposure to water and thus needs to be protected appropriately. Third, $TiB_2$ can be grown epitaxially onto SiC and may thus potentially be used as a seed layer for the epitaxial growth of $MgB_2$ and as a protective coating. Further experiments related to the integration of $MgB_2$ with $TiB_2$ are currently in progress.

## 1.12 SUPERCONDUCTING $MgB_2$ FILMS WITH ENHANCED CRITICAL CURRENT DENSITIES AND IRREVERSIBILITY FIELDS

*M. Parans Paranthaman, D. K. Christen, H. M. Christen, J. R. Thompson, C. Cantoni, H. Y. Zhai, and R. Jin*

### 1.12.1 Introduction

We report our successful demonstration of the growth of high-quality $MgB_2$ superconducting films using e-beam-evaporated boron precursor films followed by post-annealing. We also report our detailed transport-property measurements on these ex situ grown $MgB_2$ films.

### 1.12.2 Experimental Procedure

E-beam evaporation was used to deposit boron films directly on $Al_2O_3$ (102) single-crystal substrates with dimensions of 0.35 × 1.2 cm at room temperature in a vacuum system with a base pressure of $1 \times 10^{-6}$ Torr. The deposition rate for B was 10 to 12 Å/s with an operating pressure of $10^{-5}$ Torr. The film thickness was varied from 5000 to 6000 Å. The shiny amorphous B films were sandwiched between cold-pressed $MgB_2$ pellets, along with excess Mg turnings, and were packed inside crimped Ta tubes. The arrangement of materials for $MgB_2$ film-growth is shown in Fig. 1.93. The polycrystalline $MgB_2$ superconductors were prepared by a solid-state reaction of a stoichiometric mixture of Mg turnings (Aldrich, 98% pure) and amorphous boron powder (Alfa, 99+% pure) sealed in Ta tubes and heated

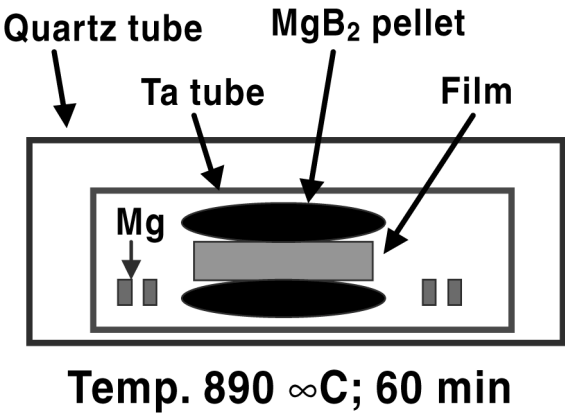


**Fig. 1.93. $MgB_2$ film-growth.**

rapidly to 890°C and held at 890°C for 2 h. The Ta tube containing the precursor film was then introduced into a quartz tube, which was evacuated to $1 \times 10^{-5}$ Torr, and sealed. The sealed quartz tube was placed inside a box furnace, where the films were heated rapidly to 890°C, held at 890°C for 60 min, and then furnace-cooled to room temperature. The as-formed purplish gray film had a very low two-probe resistance of <1 Ω. The $MgB_2$ films were analyzed by XRD. For texture analysis, a Rigaku rotating-anode X-ray generator was used, with a graphite monochromator selecting Cu $K_\alpha$ radiation, and slits defining a $2 \times 2$ mm$^2$ incident beam. A four-circle diffractometer was used to collect pole figures, ω scans, and ϕ scans. A Hitachi S-4100 field-emission SEM with a beam voltage of 15 kV was used to take images. The thickness of the films was determined by alpha step profilometer scans. $T_c$ and $J_c$ were measured with a standard four-probe method, at a criterion of 1 μV/cm to define $J_c$. During the $J_c$ measurements, a magnetic field ($H$) was applied perpendicular to the film, and the irreversibility field was defined according to the emerging voltage-current power-law characteristic, $V \alpha I^2$.

The hysteretic magnetization $M(H,T)$ of the $MgB_2$ samples was measured in a SQUID-based magnetometer, equipped with a 7-T high-homogeneity superconducting magnet. Thin polycrystalline $MgB_2$ films on $Al_2O_3$ $R$-plane substrates were measured with the magnetic field applied perpendicular to the plane of the film. For comparison, we will also present results obtained from an array of $MgB_2$ particles embeddeded in epoxy. For a superconductor, the Bean critical state model provides that the persistent current density $J$ is proportional to the hysteresis in the magnetization $\Delta M = [M(\downarrow) - M(\uparrow)]$, where $M(\uparrow)$ refers to the magnetization measured in increasing field history and $M(\downarrow)$ refers to decreasing field history. More completely, we have $J_c = 15\Delta M/r$, where $r$ is an appropriate transverse dimension of the conductor (one-half of the edge length of a square film or the volume-weighted average radius of powder particles).

### 1.12.3 Results and Discussion

Typical θ-2θ scans for 5700-Å-thick $MgB_2$ films on $Al_2O_3$ single-crystal substrates are compared with polycrystalline $MgB_2$ powders in Fig. 1.94. The strong $MgB_2$ (001) and (002) signals revealed the presence of a $c$-axis-aligned film. The FWHM value for $MgB_2$ (002) omega scans was 4.45°. However, the $MgB_2$ (101) pole figure indicated that the film has a random in-plane texture. The random in-plane texture in $MgB_2$ films could be caused by the initial reaction of Mg vapors with B films at the top surface of the film. This causes bulk crystallization of $MgB_2$ rather than epitaxial nucleation of $MgB_2$ at the substrate-film interface.

Figure 1.95(a) shows the microstructure of $MgB_2$ films determined by SEM. The films have a dense microstructure with large grains present. The SEM cross section for the same

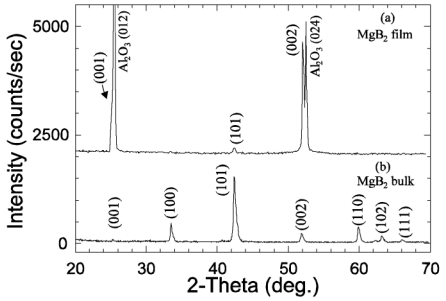


**Fig. 1.94. Typical θ-2θ scans for (a) $MgB_2$ film on $Al_2O_3$ (102) substrate and (b) powdered $MgB_2$ material.** The $MgB_2$ film has a preferred $c$-axis orientation.

film is shown in Fig. 1.95(b). A very thin layer containing Mg-Al-O is present at the substrate-film interface. To grow epitaxial $MgB_2$ films, the formation of this interfacial layer has to be prevented. The temperature-dependent resistivity for a 5700-Å-thick $MgB_2$ film is shown in Fig. 1.96. The room-temperature resistivity is around 12 μΩ-cm. The $MgB_2$ films had a sharp $T_c$ (zero resistance) of 39.06 K with a $\Delta T_c$ of 0.11 K and a ratio of the room-temperature resistivity to the residual resistivity above $T_c$ of about 3. The resistivity decreased linearly with temperature, indicating that the $MgB_2$ film is metallic.

It is interesting to compare measurements of the current density in thin films obtained magnetically, using the Bean model, with those measured directly by transport methods. Such a comparison is shown in Fig. 1.97, which plots values for $J_c$ vs applied field $H$ for two films at a temperature $T = 25$ K. The resulting values are remarkably similar, particularly since they refer to two separate films deposited in subsequent depositions. To obtain such similar results, several conditions are necessary. First, the film synthesis must have good reproducibility. Second, the film should be relatively homogeneous so that the current paths (along the sample for transport studies, circulating for magnetization studies) are simple and well defined, as assumed in the underlying analysis. A third, more subtle consideration is that the current density $J$ should be (nearly) the same for the two different measurement criteria: (1) an electric field of 1 μV/cm in the transport studies and (2) a much lower effective criterion of ~1 nV/cm or less in magnetic studies. This means that the $E$-$J$ curves are very steep or, conversely, that the current decay rate due to vortex movement is low. Indeed, we have shown that the normalized decay rate $S = -d\ln(J)/d\ln(t)$ is quite low in $MgB_2$ powder, away from its irreversibility line. For comparison, values for the current density from magnetic studies on the powder array are also shown in Fig. 1.97. Once again, the levels of current density are high and remarkably similar, showing that naturally occurring defects in $MgB_2$ are relatively effective in pinning vortices over a substantial range of magnetic field.

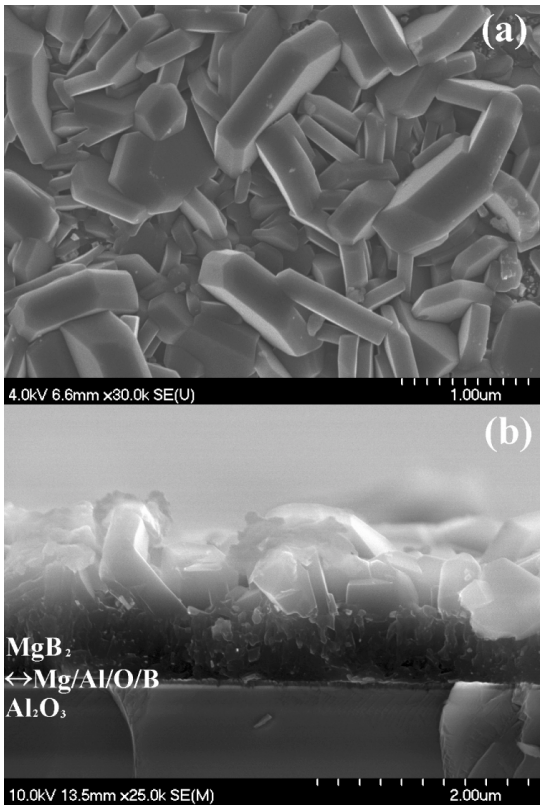


**Fig. 1.95. SEM micrograph for 6300-Å-thick $MgB_2$ film on $Al_2O_3$ substrate, (a) indicating the presence of a granular microstructure. The SEM cross section for the same film is shown in (b).**

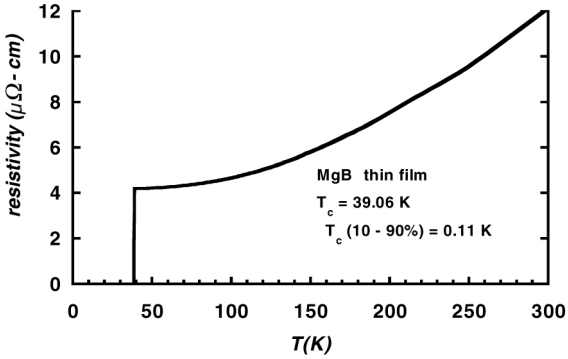


**Fig. 1.96. The temperature-dependent resistivity for a 6300-Å-thick $MgB_2$ film on $Al_2O_3$ substrate.**

In Fig. 1.97, more differences are apparent in high magnetic fields. For $H \geq 15$ kOe, the magnetic and transport measurements progressively separate. Several features can contribute to this separation. In addition to possible sample-to-sample variations in defect density (which would be most apparent at high fields when the vortex pinning array is most heavily stressed), the aforementioned difference in measurement criteria also becomes important. As the superconductive system approaches its irreversibility line, the *E-J* relation becomes more curved and the current decay rate increases. Thus the transport values would be expected to lie higher because the electric field criterion is higher. This agrees qualitatively with the experimental results. Quantitatively, however, many factors can influence such a comparison. Further work is needed to fully understand these materials, particularly the features that limit the current conduction in high magnetic fields and the mechanisms that can expand the potential operating field of $MgB_2$ conductors.

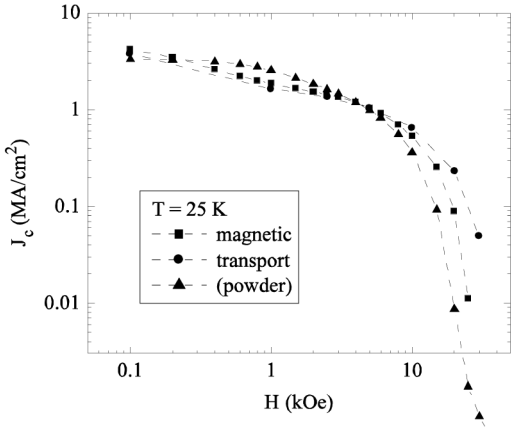


**Fig. 1.97. The field dependence of the transport and magnetic current density, $J_c$, for a 6300-Å-thick $MgB_2$ film on $Al_2O_3$ substrate at 25 K.** For comparison, the magnetic data obtained on an array of $MgB_2$ particles (powder) isolated in epoxy is also shown.

The temperature dependence of irreversibility field $B_{irr}$ obtained from transport measurements on $MgB_2$ films, is shown in Fig. 1.98. These data are compared with those obtained from magnetization measurements on polycrystalline sintered $MgB_2$ pellets. These data are quite comparable down to 26 K. At low temperatures, there is some enhancement in the film's $B_{irr}$, indicating that there is an improvement in flux-pinning properties in these $MgB_2$ films. The temperature dependence is well described by $B_{irr} \alpha (1 - T/T_c)^{3/2}$, which is depicted by the line fitted to the experimental data. For comparison, the $H_{c2}$ data for $MgB_2$ are also plotted (solid line). Further improvements in $B_{irr}$ may be possible for epitaxial films, and efforts are under way to fabricate epitaxial films on lattice-matched substrates using either in situ or ex situ methods.

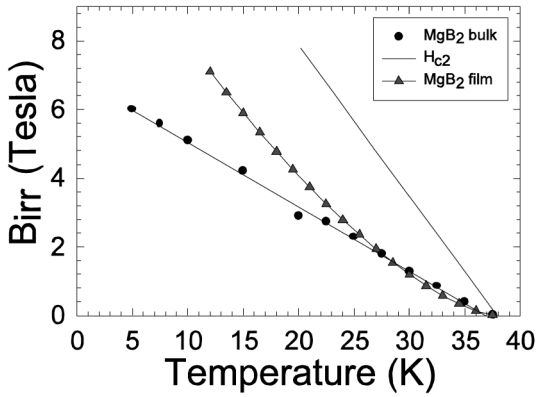


**Fig. 1.98. The temperature dependence of the irreversibility field, $B_{irr}$, obtained from a transport measurement for $MgB_2$ film on $Al_2O_3$ substrate (closed triangles) compared with those obtained from the polycrystalline 61% dense $MgB_2$ pellets (closed circles) and $H_{c2}$ data for bulk $Mg^{10}B_2$ sample (solid line).**

We have investigated the temperature and magnetic-field dependence of the Hall coefficient of two well-characterized superconducting $MgB_2$ films ($T_c = 38$ K) in both the normal and superconducting states. The temperature dependence of Hall coefficient, $R_H$, and longitudinal resistivity, ρ, at $H = 2$, 4, 6, and 8 T are shown in Fig. 1.99. Figure 1.99 clearly indicates that the sign change of $R_H$ occurs before ρ reaches zero. This strongly suggests that the Hall anomaly is a consequence of vortex dynamics. Quantitative analysis of our data indicates that the Hall response of $MgB_2$ behaves very similarly to that

of high-$T_c$ cuprates: $R_H \alpha T$ and $\cot\theta_H \alpha T^2$ in the normal state and a sign reversal of $R_H$ in the mixed state. This suggests that the B-B layers in $MgB_2$, like the Cu-O planes in high-$T_c$ cuprates, play an important role in the electrical transport properties.

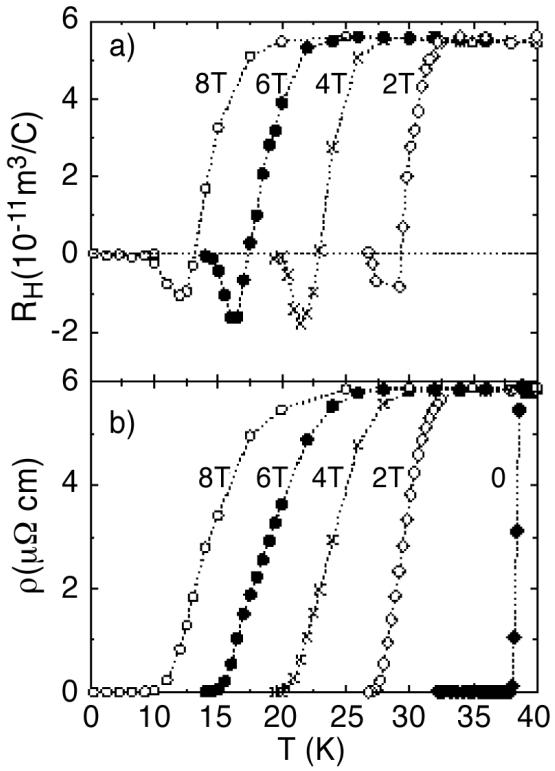


**Fig. 1.99. Temperature dependence of (a) $R_H$ and (b) longitudinal resistivity $\rho$ at $H$ = 2, 4, 6, and 8 T.**

# 2. Technical Progress in Applications Development

## 2.1 SUPERCONDUCTING POWER TRANSMISSION CABLE

*J. W. Lue, J. A. Demko, R. Grabovickic, M. J. Gouge, P. W. Fisher, D. R. James, I. Sauers, and C. A. Foster, Fusion Energy Division; J. P. Stovall, Engineering Science and Technology Division; and P. M. Martin, Metals and Ceramics Division*

Southwire Company and Oak Ridge National Laboratory (ORNL) have jointly developed and installed a 30-m-long (100-ft-long) high-temperature superconducting (HTS) power cable and are presently operating it to demonstrate the feasibility of this promising electric utility application.[1–17] Superconducting power transmission and distribution cables offer the opportunity to dramatically reduce power loss caused by resistance in cables; provide an alternative to copper and aluminum cables in crowded underground ducts, allowing utilities to deliver more power in dense urban areas; and transmit power using an environmentally friendly coolant, liquid nitrogen.

Southwire Company is operating an HTS cable system at its corporate headquarters. The 30-m-long, three-phase cable system—rated at 12.4 kV, 1250 A, and 60 Hz—is powering three Southwire manufacturing plants. Cooling is provided by a pressurized liquid nitrogen system operating at 70–80 K. The cables were energized on January 5, 2000, for on-line testing and operation and in April 2000 were placed into extended service. As of August 1, 2001, the HTS cables have provided 100% of the customer load for 8500 h. The cryogenic system, built by PHPK Technologies, Inc., in Columbus, Ohio, has been in continuous operation since November 1999. The HTS cable system has not been the cause of any power outages to the average 20-MW industrial load served by the cable. The cable has been exposed to short-circuit currents caused by load-side faults without damage. Based upon field measurements described in Sect. 2.1.1, the cable critical current—a key performance parameter—remains the same and has not been affected by the hours of real-world operation, further proving the viability of this promising technology.

The present HTS cables were built with cold dielectric and have a coaxial neutral HTS conductor that shields the phase conductor. The three phases are housed in separate cryostats for this demonstration. For some retrofit applications, the three phases must be placed inside a single pipe. The cold dielectric approach makes it possible to house all three phases equilaterally inside a single cryostat without causing large degradation and ac losses due to the fields generated by the neighboring phases. This would also lower the thermal loss through separate cryostats. A further optimization can be realized by making the three phases concentric to each other. Such a triaxial configuration requires no shielding layer, is more compact, and requires only about half of the HTS tapes that three separately shielded phases would require. In addition, the cold dielectric stays cold and thus would not suffer from degradation due to temperature rise from the heat loss, as would be the case for a conventional copper triaxial cable. A 1.5-m-long triaxial HTS cable prototype was fabricated by the Southwire Company. Electrical tests including dc V-I curve and ac loss measurements have been performed at ORNL and are described in Sect. 2.1.2.

Practical applications of HTS transmission cables require that cable sections be periodically spliced together. An HTS transmission cable splice with a cold dielectric construction rated at 1250-A phase current and 7.5-kV phase to-ground voltage has been fabricated by Southwire Company and tested at ORNL. The splice joins the HTS phase and the neutral conductors as well as the Cryoflex™ dielectric tapes between the HTS conductors. Testing that consisted of direct-current characterization and alternating-current high-voltage withstand testing at 18 kV has demonstrated the nominal operating capability of the HTS cable splice. In addition, overcurrents up to 14 kA for 2 s were applied to the cable

splice repeatedly without impacting the performance. The splice generates less than 1 W of heat into the cable at rated current. The results of these tests are described in Sect. 2.1.3 and demonstrate the feasibility of splicing HTS power transmission cables.

The HTS power transmission demonstration project has been successfully operating for more almost 2 years since the initial installation of the HTS cable and liquid nitrogen cryogenic system. The initial acceptance testing of the cryogenic system, described in Sect. 2.1.4, was accomplished using an internal circulation loop and an electrical heater to simulate the HTS power transmission cable and interconnecting piping thermal load to verify that the design requirements were met. This acceptance testing verified the refrigeration capacity of the subcooler and provided a measurement of the skid heat load.

The cryogenic dielectric aging experiments conducted at ORNL to determine the expected life of the dielectric material used in the 30-m cables are described in Sect. 2.3. Four technical papers were presented at the Cryogenic Engineering Conference and the International Cryogenic Materials Conference, held in Madison, Wisconsin, on July 16–20, 2001.[1–4] This technical progress report is drawn from the information reported in those papers.

### 2.1.1 Operating Experience with the Southwire 30-m HTS Power Cable

The key component of an HTS cable is the superconductor, which in this installation is bismuth, strontium, calcium, and copper oxide (Bi-2223) and is usually referred to as BSCCO. The most common fabrication process uses a powder-in-tube method, where the BSCCO ceramic material is packed in silver or silver-alloy tubes that then undergo a series of thermal-mechanical steps resulting in an HTS tape. The HTS tapes used in this project are 3.5 mm (137 mils) wide and a 0.2 mm (8 mils) thick.

Based upon cable efficiency goals, Southwire has chosen to use the cryogenic dielectric design of HTS cable construction.[5] In this coaxial conductor design, HTS tapes are used to construct both the core conductor and the shield conductor. The HTS cable consists of three phases, referred to as phase 1, phase 2, and phase 3, with each phase being a coaxial conductor contained in a separate vacuum-insulated cryogenic pipe.

#### 2.1.1.1 60-Hz AC Operation

As of June 1, 2001, the HTS cables had provided 100% of the customer load for 8000 h. The 100% customer load means that all of the current required by the customer was flowing through the HTS cable. The HTS cable has operated for additional hours in parallel with the existing overhead distribution line, but in this mode, less than 100% of the load is served by the HTS cable. The electrical operation of the HTS cable is controlled from an electrical panel in the control room, which is located at the cable site. A programmable logic controller system located in the same control room is used to operate the cryogenic system during normal operation. Key electrical and cryogenic system parameters are monitored and recorded every 1 min for further analysis and trending. For the month of January 2001, the average current was 778 $A_{rms}$ and the peak was 1054 $A_{rms}$, as shown in Fig. 2.1. The January 1 holiday corresponds to the lowest current level during the month, and the weekends show lower currents levels as well.

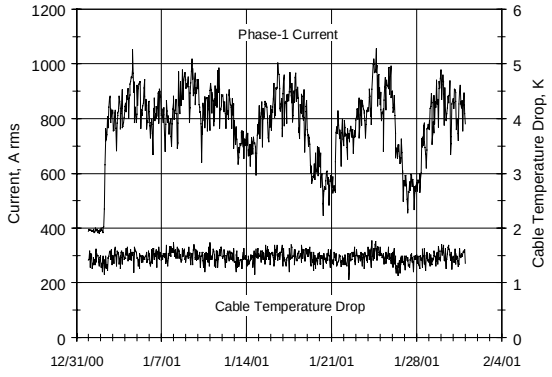


**Fig. 2.1. The phase 1 current and temperature drop across the HTS cable for January 2001, based on 1-h data sampling.**

The temperature drop along the HTS cable averaged 1.47 K during the month of January, as shown in Fig. 2.1. The temperature drop is calculated as the difference between the measured inlet and outlet temperatures to the cable. These temperatures are measured in the liquid nitrogen flow of all three phases before the flows are separated into individual flows for the phases. The design for the cryogenic system is based on an open-loop boiling bath subcooler and heater exchanger.[4,6,11] The subcooler heat exchanger uses saturated liquid nitrogen boiling on the shell side to subcool the circulating high-pressure liquid nitrogen loop that cools the HTS cables. The gas boiled off in the subcooler can be directly vented to the atmosphere or discharged through a vacuum pump system. By controlling the vacuum pump system, the sub-atmospheric pressures on the shell side of the subcooler heat exchanger can be controlled to obtain specified temperatures below 77 K. As can be seen in Fig. 2.1, this cryogenic system design and control system is providing excellent temperature control.

The HTS cable system has not caused any power outages to the average 20-MW industrial load served by the cable. The cable has been exposed to short-circuit currents caused by load-side faults without damage. Standard switch-gear and protective relay equipment have been used for the HTS cable system. Each phase of the cable is protected by a differential relaying scheme that has been coordinated with the protection system for the entire distribution circuit. In addition to the traditional electrical protection for the HTS cable, the cryogenic system's programmable logic controller can provide a trip signal to the protective relaying system. The signal will initiate a sequence to switch the overhead distribution line in parallel with the HTS cable and then disconnect the HTS cable from the distribution circuit. The customer load is not affected by the switching in this sequence. Because the time scale of events occurring on the cryogenic system is longer than those on the electrical system, the make-before-break sequence of switching is used. The tripping events monitored by the cryogenic system's programmable logic controller are low and high liquid-nitrogen system pressure, high liquid-nitrogen system temperature, and low cable termination temperature.

During a series of field measurement tests, the cable neutral current in each phase was measured, and the connection of the shield or neutral HTS conductors has been modified to increase the coupling to the core or phase HTS conductor. The theoretical value of induced current is 100% of the phase current for a very long cable. In the initial installation, each phase neutral was brought to a common point over a long overhead bus. In this arrangement, the neutral current was about 70% of the phase current. The 30-m cable is short enough that end effects influence the induced current magnitude, and different neutral connections and grounding schemes were evaluated to see the impact on induced neutral currents. It was found that the most effective arrangement was a close coupling of the three neutral phases at each end of the cable. This was achieved by connecting an aluminum bus on the neutral of each phase at the termination, to bring the neutral current to about 95% of the phase current.

#### 2.1.1.2 DC Tests

To date, three dc tests have been performed on the 30-m HTS cable as installed at Southwire. The purpose of the tests was to determine, through measurements of the critical currents of the core and shield conductors, if there has been a degradation of the HTS tapes due to the long-term field operation. The first test was conducted in November 1999. This test established a baseline for subsequent field measurements because it was conducted as part of the installation testing before the cables were energized. The second test was conducted in June 2000, after approximately 1000 hours of operation; the third test was conducted in March 2001, after approximately 7200 hours of operation. The field measurements were conducted while the cable was operating at normal design conditions for liquid nitrogen temperature, pressure, and flow rate. The exception was the November 1999 test, when the liquid nitrogen temperature was higher because there was no subcooling.

In addition to the field tests, the critical current was measured on the first two phases in a factory floor test immediately after they were manufactured. The tests were conducted on both the phase 1 and 2 core and shield conductors in April 1999 and May 1999, respectively. The factory floor measurements were conducted with each coaxial cable installed in a cryogenic pipe with temporary terminals that allowed voltage taps to be placed directly across the HTS conductors. During the test, the cables were cooled with liquid nitrogen at a small pressure above atmospheric and a very low liquid nitrogen flow rate. Both the factory floor and field tests were limited to the 3000-A rating of the power supply.

### *Critical Current of the Core Conductors*

Because of high-voltage considerations, voltage taps were not installed inside the cable across the superconductor to allow direct measurement of the voltage drop. Instead, temporary voltage taps were placed on the termination-to-overhead bus connection during all of the dc field tests. Thus, the voltages measured included sections of the copper bus inside the terminations and several copper connections, in addition to the HTS conductor. Figure 2.2 shows the V-I curves of the phase 2 core conductor from all three field tests and shows a linear relationship in V-I curves. Since all three phases are similar in their response, only phase 2 is shown for illustration.

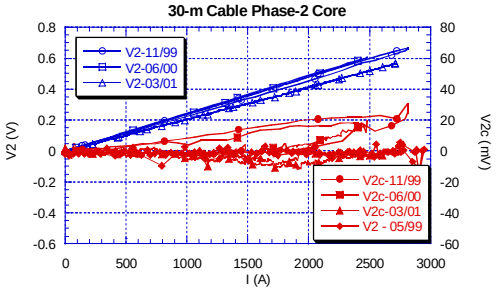


**Fig. 2.2. The V-I curves of the phase 2 core conductor with the calculated HTS core conductor voltage drop shown on the right-side scale.**

To find the voltage drop of the HTS core conductor itself, a linear equation was fitted to the lower currents. This linear behavior of the V-I curve at low currents is assumed to be due to the resistance of the copper bus and contacts and remains constant for all currents. This linear term was subtracted from the total voltage drop to obtain the HTS core conductor voltage drop. This calculated core conductor voltage drop is shown on the right-side scale of Fig. 2.2. Also shown in Fig. 2.2 is the voltage drop, V2–05/99, which was directly measured across the HTS core conductor during the factory floor test and shows the critical current of the phase 2 core conductor to be above 3000 A. Since the calculated core conductor voltage drop, V2c, remains near zero across the current range, and the magnitude is about 1% of the total voltage drop (which is within the range of measurement accuracy), the critical current of phase 2 core conductor has remained above 3000 A after 14 months of field operation. Also, the most recent data of March 2001 is indistinguishable from the factory floor data of May 1999. Similarly, the critical currents of phase 1 and 3 core conductors remained above 3000 A after 14 months of field operation.

In finding the calculated cable voltage drop, we assumed that the copper bus and contact resistances remained constant over the entire current range. This assumption may not be valid because the bus and contacts may heat up at higher currents and have increasing resistances. To verify this assumption, we changed the current ramp rates to determine if the heating effect would be smaller at faster ramp rates. During the March 2001 field test, the total ramp time (both up and down) was varied from 100 s to 50 s and then to 25 s. No appreciable copper bus heating effect was observed. However, in the November 1999 field test, the total ramp time was set at 500 s, and in the June 2000 field test, it was about 350–450 s. In both tests, small loops were observed in the voltage drops. Thus, the down-ramp curves of the conductor voltage drop in these two test sets included the extra voltage drop of the heated bus.

### *Critical Current of the Shield Conductors*

Similar tests were performed on the shield conductors of the three separate phases of the 30-m HTS cable; the response for phase 3 is show in Fig. 2.3. Both the total voltage drop and the calculated shield conductor voltage drop are similar for the three shield conductors. The calculated shield conductor voltage drop at higher currents showed curvatures characteristic of a superconductive-to-resistive transition. These curvatures were also lower than the measurements made during the factory floor tests for phases 1 and 2. The critical currents at 3 mV (1 µV/cm criterion) remained at about 2000–2300 A for the three shield conductors after 14 months of field operation.

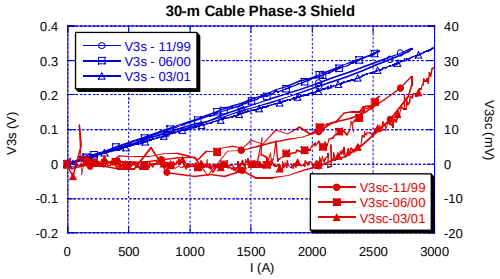


**Fig. 2.3. The V-I curves of the phase 3 shield conductor with the calculated HTS shield conductor voltage drop shown on the right-side scale.**

The difference in the shield conductor critical current between the factory floor testing and field testing is a consequence of the different conductor temperatures during the two tests. The critical currents of phase 1 and 2 shield conductors were measured to be about 1600 A during the factory floor test. During the factory floor test, the conductor temperatures were about 5 K higher than during the field tests. According to the temperature dependence measured on the 5-m cables,[14] the critical current should increase by about 25% when the conductor temperature is lowered 5 K. Thus, the shield conductor critical currents for phase 1 and 2 should be about 2000 A, a value consistent with the field test measurements. Hence, no degradation in the HTS shield conductors has been observed.

The slopes of the total voltage drop curves in Fig. 2.2 indicated that the resistance of the copper bus and contacts is about 0.24 mΩ for the core conductor. Fig. 2.3 indicates that the resistance of the bus and contacts is about 0.11 mΩ for the shield conductor. The resistance is more than double in the core conductor because the bus is longer in the core conductors.

### *Current Transition*

To determine the effect of operating a superconducting cable above its critical current, we allowed the shields of phase 2 and 3 in series to operate above their critical current for a short time during the March 2001 field tests. Figure 2.4 shows the dc current ramping from zero to the power supply limit of 3030 A in 40 s and then holding for 60 s. The 3030-A current was flowing through the shield of phase 2 and 3 for more than a minute, after which time the current was returned to zero. Note that the critical currents of the shield were previously measured to be no more than 2300 A. The length of time that the HTS BSCCO tapes could safely be held above critical current was based on previous fault current testing of 5-m cables.[9]

Figure 2.4 shows the voltage drop, V2s and V3s, for the two shield conductors. The voltage drop, increased linearly with time until the current reached 3030 A. During this time, the voltage drop was primarily due to the bus and contact resistances. After 10 s of steady current at 3030 A, the voltage drop increased sharply,

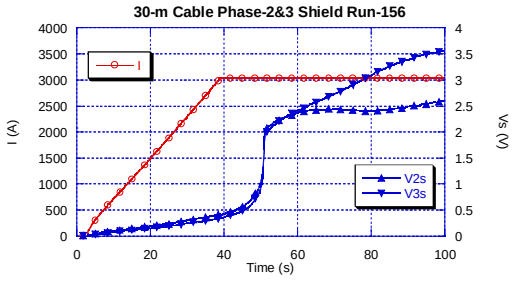


**Fig. 2.4. Current and voltage drop on phase 2 and 3 shield conductors during current transition.**

from about 0.7 to 2 V. This corresponds to the time at which the shield conductors were heated to the transition temperature of the HTS BSCCO tapes. Thereafter, the shield conductors were completely normal, and the current was flowing in the silver-matrix of the HTS BSCCO tapes. The phase 2 shield conductor was apparently cooled better than the phase 3 conductor so that the former voltage drop stayed around 2.5 V while the latter reached 3.5 V by the end of the test.

Assuming the bus and contact resistances did not change appreciably during the overcurrent time, their portion of voltage drop would stay at about 0.5 V. Thus, the voltage drop across the shield conductors was 2–3 V during this time. Under these conditions, a heat of more than 13 kW was generated by the phase 2 and 3 shield conductors, which is more than three times the cryogenic system capacity of 4 kW. However, because the length of the test was less than 2 min, the cryogenic system was able to respond adequately. A review of the cryogenic system performance data, which is continuously recorded at 1-min intervals, indicates that the liquid nitrogen flow rate and pressure remained constant. The liquid nitrogen temperature measured at the outlet of all three cables increased by 1 K for 15 min and then dropped to a 0.5 K increase that decayed linearly over the next 1.75 h. The 13 kW of heat produced by the two shield conductors corresponds to about 0.4 W/cm$^2$ of surface heat flux. This flux is much lower than the boiling heat flux of liquid nitrogen, which is about 20 W/cm$^2$, although the HTS tapes are not in open bath.

After this test, the V-I curves of the two shield conductors were again measured and found to be the same as before the test. As expected, the short time of overheating did not harm the HTS tapes. In normal 60-Hz ac operation, the HTS cables would not be exposed to currents of this magnitude or duration, as the protective relaying system would operate and disconnect the distribution circuit and HTS cable from the power system.

#### 2.1.1.3 Summary

Southwire Company is operating the first real-world application of an HTS cable system at its corporate headquarters, marking the first time a company has successfully made the difficult transition from laboratory to practical field application of an HTS cable. In April 2000, the HTS cable system was placed into extended service and has logged over 8000 h of flawless operation in the 14 months ending June 1, 2001. The cryogenic system has been in continuous operation since November 1999. The cable has not been the cause of any power outages to the average 20-MW industrial load served by the cable and has been exposed to short-circuit currents caused by load-side faults. A third measurement of the performance of the superconductor in March 2001 indicated no measurable change in the critical current of the superconductor—a key performance parameter—providing further credence to the viability of this promising technology.

Based upon field measurements, the critical current of all three HTS core conductors is more than 3000 A and that of the HTS shield conductors is between 2000 to 2300 A. The field measurements were conducted while the cable was operating at normal design conditions for liquid nitrogen temperature, pressure, and flow rate. Both the core and shield conductors of the first two phases were measured during a factory floor test immediately after manufacturing in a separate setup, and those critical current measurements are consistent with those measured in the field. The difference in the critical current between the core and shield conductors is due to the different specification of the BSCCO tapes.

A transition current test was conducted on the phase 2 and 3 shield conductors to determine the effect of operating a superconducting cable above its critical current. The shield conductors were briefly heated above the HTS transition temperature. Although the extra ohmic heating power was much higher than the capacity of the cryogenic system, the system was able to maintain adequate cooling because of the short duration of the test (less than 2 min). As expected, the BSCCO tapes were able to withstand the

overcurrent, as no difference was observed on the V-I curves of these two shield conductors when measured before and after the current transition test.

### 2.1.2 Electrical Tests of a Triaxial HTS Cable Prototype

The HTS transmission cable based on the cold dielectric concept with an HTS shield makes it possible to house all three phases inside a single cryostat without causing large degradation and loss due to magnetic fields generated by the neighboring phases. A further optimization can be realized by making the three phases concentric to each other. No shielding layer is required in such a triaxial configuration. It would be more compact and require only about half of the HTS tapes that three separately shielded phases would require. A 1.5-m-long triaxial HTS cable prototype has been fabricated and tested. Each phase consists of two layers of BSCCO-2223 HTS tapes. Electrical tests of the cable included the dc V-I curve and ac loss measurements. The ac losses were measured both electrically and calorimetrically. Finite-element thermal modeling was performed to check the calorimetric calibration. Individual-phase ac losses indicate good agreements with the monoblock theory. Three-phase ac loss is close to that of the sum of the three individual phases. There is no measurable excess ac loss due to the presence of the other concentric phases. A total three-phase ac loss of about 1 W/m was measured at the design operating current of 1250 A.

#### 2.1.2.1 Triaxial Cable Prototype

A 1.5-m-long triaxial HTS cable prototype was fabricated by Southwire Company for evaluation of its superconducting properties with dc and ac currents. Figure 2.5 shows a sketch of the end of the triaxial cable. The cable was wound on a stainless steel former. Each phase consists of two layers of BSCCO-2223 HTS tapes. The layers are separated by Cryoflex™ cold dielectric tapes. A layer of copper tape was also added at the outside diameter of the triaxial cable as a shielding ground. The cable is rated for 1250 $A_{rms}$ per phase—the same as the 30-m demonstration cables.

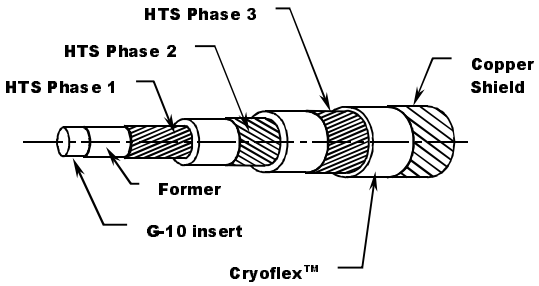


**Fig. 2.5. End-view of the triaxial cable prototype.**

For the electrical testing of the cable, voltage taps were added on each of the three phases. One of the voltage leads was pulled to the other end of the cable to join with the other lead before the dielectric and the next HTS phase were wound on. The actual voltage lead lengths are 1.54, 1.24, and 0.91 m for phases 1, 2, and 3, respectively. The G-10 insert shown in Fig. 2.5 was added to enable a calorimetric measurement of the ac losses of the cable. Two type-E thermocouples were attached on the G-10 rod. When the rod was inserted inside the former, the thermocouples touched the former at the midpoint and a quarter of the way from an end. The G-10 insert was sealed with silicon grease so that no liquid nitrogen can get inside the former.

#### 2.1.2.2 Characteristics of the DC V-I

The dc test of the triaxial cable was performed with a 25-kA, 15-V dc power supply. Figure 2.6 shows the measured V-I curves of each of the three HTS phases. At the standard 1-μV/cm criterion, phases 1 through 3 had critical current values of 3.6, 3.1, and 2.8 kA, respectively. These values are comparable to the 30-m demonstration cables installed at Southwire. Those cables used four layers of HTS tapes for each phase conductor.

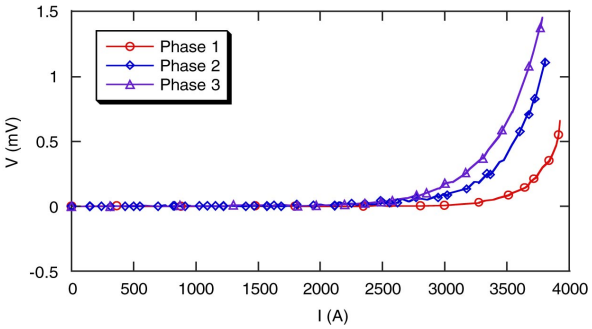


**Fig. 2.6. V-I curves of each of the three HTS phases.**

The electrical tests of this cable, performed for a 5-month period, required numerous cooldown and warmup cycles with liquid nitrogen and changing of bulky power lead connections. The latter caused clearly visible damage to a lead connector of phase 1. Similar damage may also have occurred in phase 2. These two phases showed some degradation in the V-I curves. In contrast, the V-I curve of phase 3 remained the same throughout the test period. There was no degradation in this phase.

### 2.1.2.3 Calorimetrics

We developed a calorimetric technique to measure the ac loss of prototype HTS cables.[7] Previously, single-phase prototype cables were made without a dielectric layer. To measure ac loss, we inserted the cable inside a G-10 tube filled with wax to create a radial thermal barrier between the HTS conductor and the liquid nitrogen bath. The temperature rise of the HTS cable due to the ac loss was measured with thermocouples attached to the conductor and referenced to the bath. The present triaxial cable prototype was built with three dielectric layers, which should thus provide some thermal barrier. We decided to measure the ac-loss-induced temperature rise on the former with thermocouples attached on a G-10 rod and inserted inside the former as shown in Fig. 2.5.

#### *Heat Load Calibration*

To calibrate the temperature rise for a known heating power, we again used the dc characteristics of the HTS phase conductors. A dc current close to and higher than the critical current of the HTS conductor was applied to the phase conductor. The voltage drop and current of the cable were measured to calculate the power input. The temperature rise on the former at this input power was measured by the thermocouples. Fig. 2.7 shows voltage across the phase.

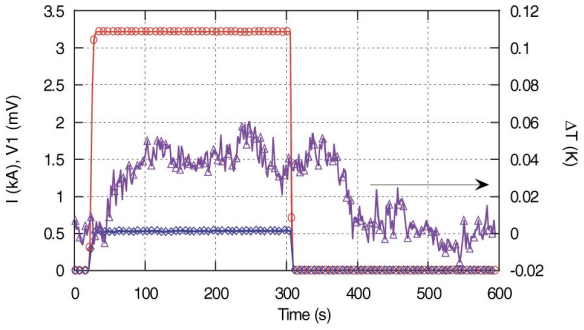


**Fig. 2.7. Heat load calibration on phase 1 conductor with a dc current of 3.2 kA that developed 0.54 mV.**

A dc current of 3.2 kA was applied to the phase 1 HTS conductor, and a constant voltage of 0.54 mV developed across the cable. The thermocouple showed a gradual temperature rise and reached a flat top of about 0.05 K in 100 s. After the current was turned off, it also took about 100 s for the former to cool back down to the bath temperature. By varying the current, we obtained a set of $\Delta T$ vs the heating power per unit length, $p$. The oscillation in the temperature rise curve indicated a sensitivity of about 0.01 K for the instrumentation used in the present test. This sensitivity limits the present calibration and the calorimetric data of the outer two phases of the triaxial cable. To clarify the situation, we performed a finite-element thermal model calculation.

### *Finite-Element Thermal Modeling*

A finite-element thermal model of a small section of the HTS triaxial cable, comprised mainly of eight-node solid elements, was built using SINDA Thermal Desktop™.[18] A fixed $LN_2$-temperature boundary condition was applied to the nodes on the outermost surface of the copper shield layer. All other external surfaces were considered adiabatic. We modeled the HTS phase conductor layers as being a single element thick and applied heat generation to them as appropriate to simulate the calibration or ac loss heat load.

The thermal properties of many of the materials used in the test article—e.g., G-10, stainless steel, and copper—are well characterized in the literature. The HTS tapes were assumed to behave thermally as silver. Low-temperature thermal conductivity data were not found for the Cryoflex™ tape dielectric material. The effective thermal conductivity used to model the Cryoflex™ layers was adjusted by using the temperature rise data obtained from the dc calibration tests of phase 1. The calibration data for this innermost phase had the highest temperature rise and would be the most accurate measurement to use to estimate the thermal conductivity. Once this value was determined, calculations were made to determine the temperature rise for heating in the other two HTS phases. Figure 2.8 shows the temperature profile across the radial section of the triaxial cable for a heat load of 1 W/m applied to phase 1. A constant temperature rise of $\Delta T_1 = 0.052$ K was found inside the former of the cable.

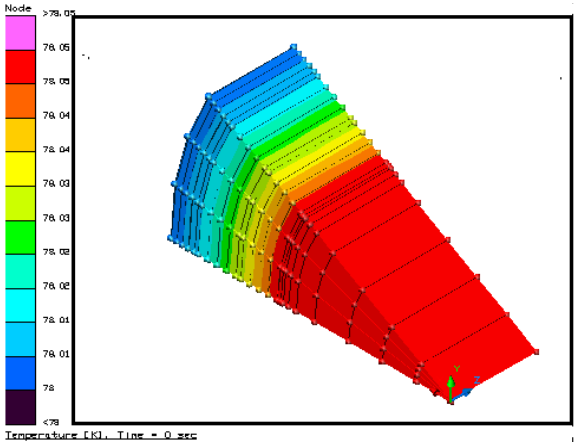


**Fig. 2.8. Temperature profile across the triaxial cable with a heat load of 1 W/m on the phase 1 conductor.**

Similar results were obtained for heat load on the other two phases. The calculations show that there is less temperature rise as the heating is applied to layers farther from the center of the HTS cable. This is because there is less thermal resistance to the liquid nitrogen as the distance from the heat source to the liquid nitrogen decreases. For the heat load of 1 W/m, the temperature rise in phase 2, $\Delta T_2$ was found to be 0.029 K; in phase 3, $\Delta T_3$ was 0.010 K. The temperature rise was also found to be linear with respect to the heat load. This is shown in Fig. 2.9, together with the calibration data of phase 1. Also shown in Fig. 2.9 are the temperature rises when the same heat load is applied simultaneously in all three phases, $\Delta T_{tri}$. These temperature rise vs heat load curves are used to calculate the calorimetric ac losses.

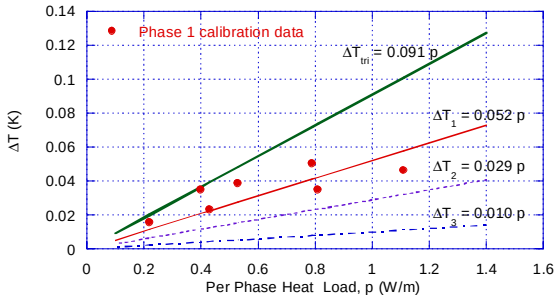


**Fig. 2.9. Temperature rise inside the former as a function of heat load applied separately on each phase and simultaneously on all three phases.**

These results also indicate that the temperature rise on the HTS phases would be minimal if one chooses to cool the triaxial cable on the perimeter alone—that is, with no coolant flow through the former. For an ac loss of 3 W/m (1 W/m per phase), the highest temperature rise in the cable is still less than 0.1 K. No degradation in the HTS phase conductors would be expected.

### 2.1.2.4 AC Loss Measurements

The ac loss of the triaxial HTS cable prototype was first measured with the existing single-phase ac power supply. Both electrical and calorimetric techniques were used in the measurement. The power supply was then upgraded to three phases, which were powered by a single 480-V source. Thus, the phase angles were fixed at 120° apart. Separate Variacs permitted individual control of the phase currents.

#### *Single-Phase Measurements*

The ac loss was measured up to 1350 A on each of the three phases separately. For the electrical measurement, the voltage and the phase angle, θ, relative to the current were measured with a lock-in amplifier. The ac loss per unit length was then calculated by $p = VI \cos \theta / L$, where $L$ is the voltage taps length of each of the phases. For the calorimetric measurement, the equations shown in Fig. 2.9 were used to determine the individual-phase ac losses. Figure 2.10 shows the results on phase 1 of both of the measurements. Because of the sensitivity limit mentioned before, the calorimetric data range was limited. But the two sets of data agree with each other surprisingly well, providing further confidence to the calibration procedure discussed earlier.

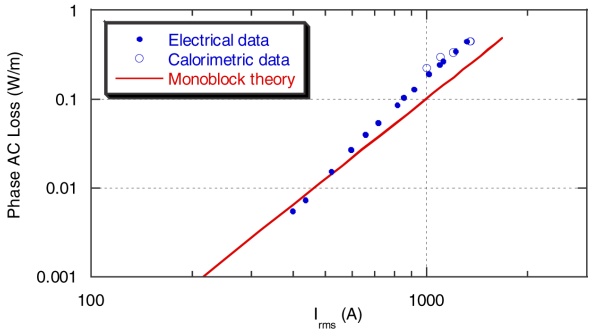


**Fig. 2.10. The ac loss with single-phase current on phase 1.**

Also shown in Fig. 2.10 is a curve calculated with the monoblock theory.[19] The experimental ac loss data are in fair agreement with this simple theory. Similar results were observed for the ac losses measured electrically for phases 2 and 3. Note that at the design current of 1250 $A_{rms}$, the ac loss on phase 1 was measured as 0.35 W/m. For the same loss on phases 2 and 3, Fig. 2.9 indicated that the temperature rise on phase 2 would be 0.01 K and on phase 3, 0.004 K. Both are at or below the sensitivity of the temperature instrumentation. No measurable calorimetric ac loss data were obtained on these two outer phases.

#### *Three-Phase Measurements*

When current is applied to more than one phase of the triaxial cable, the mutual inductance among the phases affects the phase angle between the current and the voltage of each individual phase. This interaction precluded a definitive measurement of voltage loss on each phase from the lock-in amplifier measurement. This problem was anticipated from the outset, and the calorimetric technique alone was used, although its useful range was limited.

The ac loss of the triaxial cable was measured calorimetrically with equal currents of up to 1350 A on all three phases. To double-check the effect of neighboring phases, we also ran a series of adding current to successive phases. First, the current was brought up on phase 1 only. After the temperature rise was stabilized, the same amount of current was brought up on phase 2 to measure the additional temperature rise. Then the phase 3 current was brought on to measure further temperature rise. Fig. 2.11 shows an example of such a sequential multiphase ac loss measurement. With a current of 1300 A on phase 1 alone, a temperature rise of about 0.024 K was observed. When the same amount of current was also brought on phase 2, there was only a small additional temperature rise. After the current was also brought on phase 3,

the total temperature rise was about 0.030 K. The temperature rise on the cable appears to be even more dominated by phase 1 than is indicated in Fig. 2.9 from the model calculation.

If the currents on phases 2 and 3 introduced significant additional ac loss on phase 1, we should see more temperature rise above 0.024 K. If the ac losses on phases 2 and 3 were more than the loss of its own current, the additional temperature rise should be much more than that shown in Fig. 2.11. Neither of these effects was seen. Thus, this and all other multiphase ac loss measurements showed no measurable excess ac loss. The ac loss of the triaxial cable can be approximated by using the $\Delta T_{tri}$ calibration equation in Fig. 2.9, which assumed equal loss in each of the three phases. The result is shown in Fig. 2.12. The calorimetrically measured ac loss of the triaxial cable is also in fair agreement with the sum of the three individual phase losses calculated by the monoblock theory. This is a further indication that there is no excess ac loss in triaxial configuration where the three phases are concentric to each other. At the design current of 1250 A, the measured total ac loss of the present triaxial cable is only about 1 W/m.

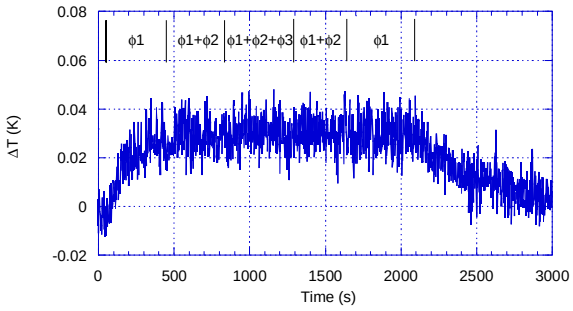


**Fig. 2.11. Temperature rise on the triaxial cable former with a current of 1300 $A_{rms}$ on phase 1, phase 1 + phase 2, and phase 1 + phase 2 + phase 3 in sequence.**

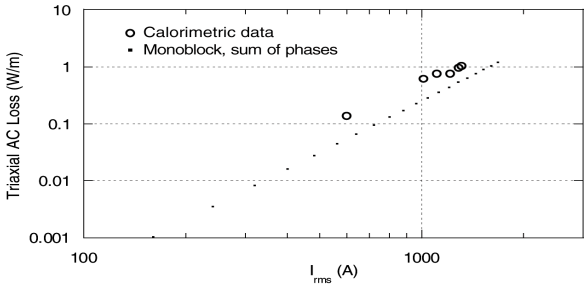


**Fig. 2.12. Total triaxial cable ac loss as compared to the monoblock theory calculation that sums the three individual phase losses with no additional terms.**

### 2.1.2.5 Summary

A 1.5-m-long triaxial HTS cable prototype was fabricated by Southwire Company and tested at ORNL. Electrical tests including dc V-I curve and ac loss measurements were performed. The ac losses were measured both electrically and calorimetrically. Finite-element thermal modeling was performed to get a self-consistent calorimetric calibration. Individual phase ac losses show good agreement with the monoblock theory. The three-phase calorimetric ac loss data are close to those of the sum of three individual phases. There is no measurable excess ac loss due to the presence of the other concentric phases in triaxial cable configuration. At the design current of 1250 A, the measured total ac loss of the present triaxial cable prototype was only about 1 W/m.

## 2.1.3 Performance Tests of an HTS Power Transmission Cable Splice

HTS cables will be manufactured in finite-length sections. For installations longer than these sections, joining of HTS cables will require fabrication of splice joints between sections. The splice must provide for a continuous flow of liquid nitrogen through the former, a superconducting main conductor, sufficient dielectric for the high operating voltage, and, in the case of the cold dielectric cable, a continuous HTS shield. The technology that meets these requirements has been demonstrated for a cold dielectric HTS cable splice. This section discusses the results of the tests.

Initial test results of this HTS splice cable were reported in Ref. 7. The basic geometry of the HTS cable splice is shown in Fig. 2.13. Layers of silver-alloy-sheathed BSSCO-2223 HTS tapes are helically wound over a flexible, stainless steel former to construct a cold dielectric cable. The main conductor layers and shield conductor layers are separated with an appropriate amount of Cryoflex™ dielectric to provide the required electrical insulation level for operation at 7.5-kV phase to-ground voltage. The splice section is about 1.1 m long and is about 10% larger in diameter than the HTS cable as seen in Fig. 2.13. The features in Fig. 2.13 are exaggerated for clarity. The former, the main conductor, the dielectric layers, and the shield conductor are joined together in the center section. On either side of the splice is an electrical stress cone to relax the electrical field gradients between the main conductor at high voltage and the shield conductor at ground potential. The HTS cable splice performed successfully in several test procedures, including dc critical current measurements, high-voltage operation at 7.5-kV, high-voltage ac withstand testing at 18 kV for 30 min, and basic impulse level (BIL) testing to 110 kV. All the tests were conducted at the ORNL HTS cable test facility.

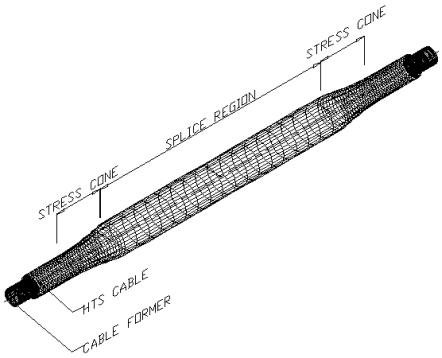


**Fig. 2.13. Generic HTS cable splice geometry.**

### 2.1.3.1 The DC V-I Curves and Overcurrent Tests

Overcurrent pulses that were higher than the operating current or the critical current of the HTS cable splice were applied to the cable splice to simulate fault currents such as those from short-circuit faults. Measurements of the cable voltage, the coolant temperature, and the pressure during the pulse and for some time after the pulse were recorded. Tests were performed at the ORNL 5-m test facility with maximum pulse currents up to 14 kA and pulse lengths up to 2 s. Some degradation was observed in the V-I curve of the cable after the first test series. A second series of tests was conducted to determine further degradation with repeated overcurrents.

A dc power supply that is capable of providing 25,000 A at 12 V was used for the dc testing. The power supply can be manually operated, or the current can be controlled with a 0- to 15-V signal to the power supply. The dc tests were conducted using National Instruments LabView software both to control the power supply operation and to obtain computer data. The power supply provides a small residual current of a few hundred amperes although the control voltage is zero.

The first three shots were initial dc critical current measurements. The next ten shots were the first series of pulse tests. In this series of tests, the pulse length was first fixed at 2 s, and the control signal voltage was increased from 2 to 9 V, corresponding to currents from 3.3 to 15 kA. The pulse length was later shortened to 1 s for the 13.3-kA (8-V control signal) and 15-kA (9-V control signal) shots. Figures 2.14 and 2.15 show the current and voltage traces of 4- and 10-kA shots. The current trace was noisy because of instrumentation problems. Along with the data, connected by dashed lines, a four-point weighted average of the current is shown in the two current curves. The instrumentation problem was corrected for later sets of data.

In the 4.5-kA shot, the cable voltage rises to around 0.45 V and holds steady with the current until the end of the pulse. At the end of the shot, the cable begins to heat up, and the splice cable voltage rises. The dc critical current measured prior to application of these overcurrent pulses was more than 2200 A for the splice cable using the 1-μV/cm criterion. About 2 V was developed across the cable for the 10-kA overcurrent pulse. This, combined with voltage drop along the power cables, had apparently exceeded the

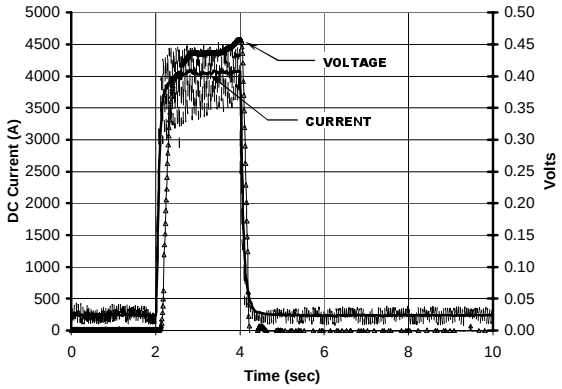


**Fig. 2.14. HTS splice cable voltage and current for a 2-s, 4.5-kA pulse.**

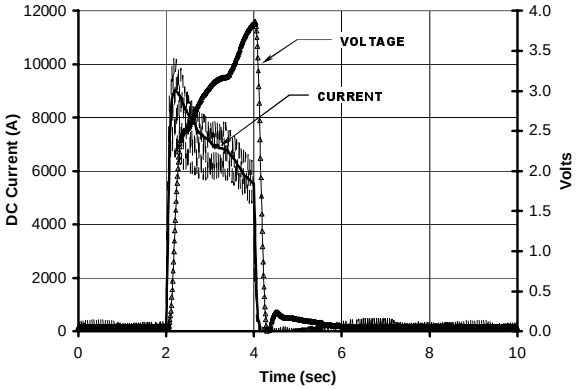


**Fig. 2.15. HTS splice cable voltage and current for a 2-s, 10-kA pulse (shot 9).**

power supply compliance and caused the applied dc current to drop. By the end of the 2-s, 10-kA pulse, the current dropped to about 6 kA. The cable voltage continued to rise during the pulse to about 3.8 V, indicating that the conductor resistance was increasing because its temperature was rising.

The splice cable resistance was determined simply by dividing the measured voltage by the corresponding current. At the beginning of the 10-kA pulse, the cable resistance went to 0.27 mΩ (as compared with 0.23 μΩ at $I_c$) and increased to 0.67 mΩ by the end of the 2-s pulse. For comparison, the room-temperature resistance of the cable was measured to be 1.9 mΩ. Previous tests on a different 5-m cable using a nonalloyed silver BSSCO-2223 tape without a splice showed that for an overcurrent of 10 kA the cable resistance went to 0.16 mΩ and did not increase much during the pulse.[9] The alloy sheath of the HTS tapes in the splice cable has higher resistance and produces more heat in overcurrents.

For shot 10, the control voltage was set at 7 V, which provided a peak current of 11 kA that decreased to 6.7 kA by the end of the 2-s pulse. The cable resistance increased from about 0.3 to 0.8 mΩ during the pulse. At about 2.5 s after the pulse, the cable resistance was decreasing from above the room-temperature resistance of 1.9 mΩ. Thus, the conductor was heated above room temperature in this shot. The temperature data log indicated that this shot was taken before the coolant temperature was fully recovered. The next three shots were taken with pulse length of 1 s. The highest peak current during these three shots was 14 kA. The cable resistance, however, stayed below 1 mΩ. Thus, no additional overheating of the HTS splice cable occurred.

Figure 2.16 shows the temperature rise of the liquid for the HTS cable splice during the first series of overcurrent shots. The data were scanned every 30 s, so this temperature rise was observed after the shot was completed. It took from 5 to 10 min between overcurrent shots for the liquid nitrogen temperatures to cool back down. The energy input to the liquid nitrogen stream was determined by integration of the temperature rise of the liquid nitrogen in time from the start of a pulse to the end of the pulse according to Eq. (2.1):

$$\Delta E = \int_{t_{start}}^{t_{end}} \dot{m} C_p (T_{out} - T_{in}) dt - Q_{back} (t_{end} - t_{start}) \quad (2.1)$$

This represents the total energy input to the entire HTS cable system, including the cable splice and terminations during an overcurrent shot. The equation also shows that the temperature rise for a given energy input can be limited by using higher flow rates. The background heat load, $Q_{back}$, was around

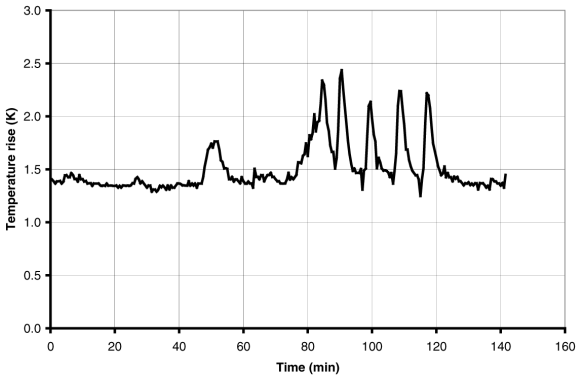


**Fig. 2.16. Temperature rise in liquid nitrogen cooling circuit during first series of pulse shots.**

530 W with no current applied to the splice cable. The temperature rise for overcurrent shot 10 occurs at around 80 min on the time scale, and the shot had an energy input of 135 kJ. The energy input to the subsequent pulses varied between 64 and 78 kJ.

The critical current of the HTS splice cable degraded 20% after the first series of overcurrent tests. The critical current was measured only before the first series of overcurrent shots and after completing the entire series. For this reason, a second series of overcurrent tests was conducted to determine if additional overcurrent pulses would introduce further degradation of the critical current. In the second series of tests (shots 14–43), the control voltage was fixed at 7 V, which provided a maximum current around 12 kA. One shot each was taken with pulse lengths of 0.5 and 0.75 s. Five shots each were taken with pulse lengths of 1 and 1.5 s. Finally, three shots were taken with a pulse length of 2 s. The critical current was measured after conducting each overcurrent shot. Figures 2.17 and 2.18 show the HTS splice cable voltage response to the 12-kA pulse for 1- and 2-s pulse times.

The energy input to the HTS cable splice from the conductor during an overcurrent shot or a dc voltage current characteristic measurement can be determined by integrating the product of the measured voltage and current in time according to Eq. (2.2):

$$\Delta E = \int_0^t VIdt \cdot \tag{2.2}$$

The results of the calculation for the overcurrent pulses are provided in Fig. 2.19, along with the maximum current applied during each shot. The energy is input to the whole HTS cable and splice, but the fraction taken up by the splice itself could not be separated from the measured data. It has been observed that pulses of up to 72 kJ had been applied to the HTS cable splice.

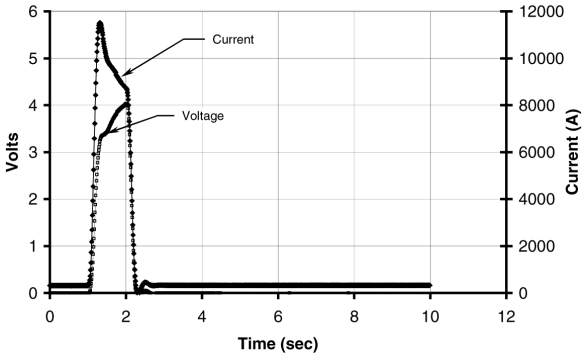


**Fig. 2.17. HTS splice cable voltage and current for a 1-s, 12-kA overcurrent pulse.**

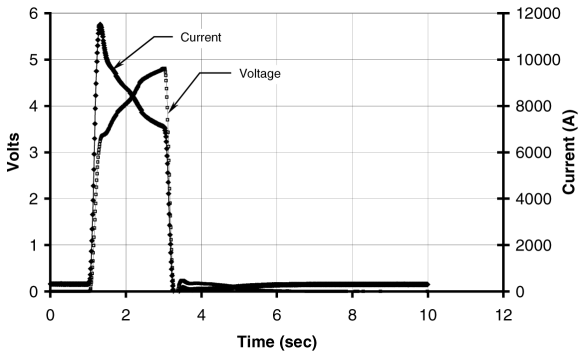


**Fig. 2.18. HTS splice cable voltage and current for a 2-s, 12-kA overcurrent pulse.**

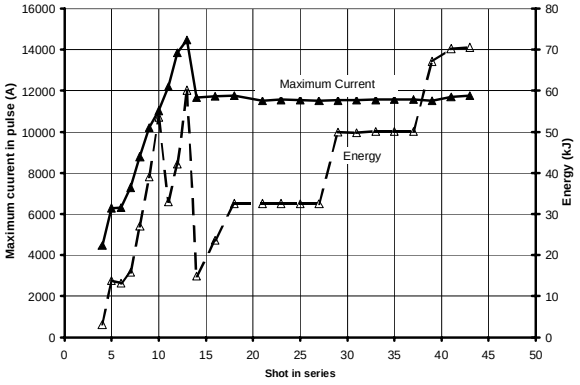


**Fig. 2.19. Maximum current and energy input to HTS cable splice during overcurrent pulse testing.**

As stated previously, the dc V-I curves of the first splice cable were measured during the first cooldown; after the first series of overcurrent test shots; and before, during, and after the second series of overcurrent test shots. At the 1-μV/cm criterion, the critical current was 2200 A at the start of the testing. As was discussed earlier, the first degradation happened in shot 10 because it was taken before the cable had cooled back down from the previous shot. Shot 10 input 135 kJ of energy to the splice cable, which is almost twice the maximum energy input from an overcurrent pulse shot. The second degradation was caused by an accidental current ramp that was held at high current too long during a V-I curve measurement. No degradation was seen in any subsequent V-I curve after each overcurrent pulse shot in that final series. As was shown previously, running the HTS splice cable at a higher flow rate would have diminished the temperature rise in the HTS splice cable, and it most likely would not have experienced any degradation in the critical current because of these shots.

### 2.1.3.2 High-Voltage Tests

To test the HTS cable splice at rated voltage, it was run successfully for 8 h at 7.5-kV ac with no indication of insulation performance deterioration. After the 7.5-kV ac run, the splice was held at 18-kV ac for 30 min. The final high-voltage test was an impulse test to demonstrate the BIL of 110 kV. A typical trace for a 117-kV impulse shot is presented in Fig. 2.20.

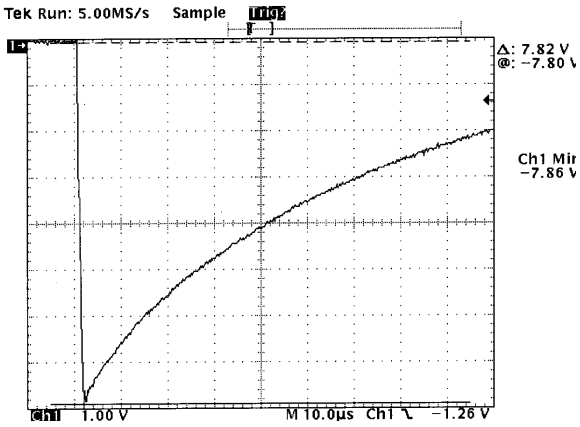


**Fig. 2.20. Negative impulse trace for a 117-kV impulse voltage applied to the HTS splice cable.**

### 2.1.3.3 Summary

In summary, two series of overcurrent short-circuit fault simulation tests were performed on the first 5-m spliced HTS cable built by Southwire Company. In the first series, pulse currents of up to 11 kA were applied to the cable for 2 s, and currents up to 14 kA were applied for 1 s. In the second series, repeated shots with a pulse current of 11.7 kA were applied to the cable for 0.5 to 2 s. Because of the alloy sheath used for the present HTS tape, higher voltage and temperature rises were observed in these tests as compared to previous tests on a 5-m cable. This was also evidenced by the coolant temperature rise after the shots.

Some degradation in the critical current of the cable was observed during the overcurrent pulse tests. However, careful examination of the shots indicated that the degradations were caused by two incidences of operator and instrumentation errors that resulted in the application of extremely high amounts of energy to the HTS splice cable. Without these incidences, the splice cable would not degrade under

repeated shots of overcurrents of up to 11.7 kA for 2 s and up to 14 kA for 1 s. Running the HTS splice cable at higher flow rates, as in all longer cables, would most likely increase its ability to withstand even more severe overcurrent pulses.

The HTS cable splice successfully passed all of the high-voltage tests and could be implemented into a utility power transmission system.

### 2.1.4 Acceptance Test and Operation of the Southwire Company 30-m HTS Cable Cryogenic System

Southwire's HTS power transmission demonstration project has been successfully operating for more than 1½ years since the initial installation of the HTS cable and liquid nitrogen cryogenic system. The cryogenic system was built by PHPK Technologies, Inc., in Columbus, Ohio. The initial acceptance testing of the cryogenic system was accomplished using an internal circulation loop and an electrical heater to simulate the HTS power transmission cable and interconnecting piping thermal load to verify that the design requirements were met. This acceptance testing verified the refrigeration capacity of the subcooler and provided a measurement of the skid heat load.

#### 2.1.4.1 Cryogenic System Description

The configuration of the cryogenic system is similar in many ways to the system described in Ref. 11. A photograph of the system is shown in Fig. 2.21. The main components are a circulation pump, a phase separator, a subcooler, and a buffer volume or ballast tank. The buffer volume serves to maintain the circulating loop pressure level. A bayonet connection to a storage dewar is used to fill the HTS cable system and to supply makeup liquid to the subcooler. The liquid nitrogen supply and return lines for the three-phase HTS power transmission cable are also connected with bayonets. The internal circulation loop consists of the circulation pump and then the subcooler, the electrical load, and the phase separator. The cryogenic system can be isolated from the HTS cable supply and return lines by closing the valves to the supply and return bayonets. This loop is used to start circulating flow with the pump when bringing the cables on-line without using the heater. During acceptance testing, the heater was turned on to demonstrate that the subcooler could remove the specified heat load. The system pressure is maintained with a ballast tank that uses a heater to boil-off liquid to maintain a set system pressure.


**Fig. 2.21. HTS power cable cryogenic system.**

The subcooler heat exchanger uses saturated liquid nitrogen boiling on the shell side to subcool the circulating high-pressure liquid nitrogen stream that cools the HTS cables. The gas boiled off in the subcooler can be directly vented to the atmosphere or can be discharged through a vacuum pump system. The vacuum pump system is used to produce subatmospheric pressures on the shell side of the subcooler heat exchanger to obtain temperatures below 77 K.

A storage dewar is used to replenish the liquid nitrogen boiled off in the subcooler and ballast tank. A second ballast tank can be filled while the other is on-line pressurizing the HTS cable cryogenic system. The filling operations of the ballast tank and subcooler are performed automatically by the control system.

The heat loads were determined from measurements of the temperature drop across the subcooler and measured flow rates of the liquid nitrogen. The temperature was measured with two Scientific Instruments silicon diode thermometers, using a model 9300 temperature indicator. The diodes were read manually during acceptance testing from the three-digit display on the temperature indicator unit. The temperature indicator was a standard unit intended for use in a laboratory, but it was used in an outdoor field installation not far from some large electrical motors. This contributed to the level of scatter obtained in the temperature measurements. The background thermal load was measured without any electrical heating. The background thermal load includes all thermal losses from background heating as well as the pumping power required to circulate the liquid nitrogen through the cryogenic system.

### 2.1.4.2 Acceptance Test Results

The heat load, $Q$, is determined from measurements of the liquid nitrogen flow rate, $\partial V/\partial t$, and the inlet and outlet temperatures from the subcooler according to Eq. (2.3). The density, ρ, and the specific heat $C_p$, are determined from the measured system temperature and pressure using GASPAK version 2.2.[20]

$$Q = \rho \frac{\partial V}{\partial t} C_p (T_{in} - T_{out}) \cdot \tag{2.3}$$

Measured temperature data from the acceptance test are shown in Fig. 2.22 along with a smoothed fit to the data shown as a solid line. The first part of the data (0 to 2 h) corresponds to the baseline tests, when no simulated heat load was applied. The background heat load for the system was determined from these data.

The system temperatures responded quickly after application of more than 3 kW of heat to the circulating loop. The applied electrical load and the calculated instantaneous thermal load are provided in Fig. 2.23. The average heat loads are represented by the lines shown in the figure. The flow rate of liquid nitrogen and the averaged thermal loads before and after application of the electrical heating are listed in Table 2.1. There is good agreement between the calorimetric measurement and the electrical heat load, with the calorimetric measurement only 8% less than the measured electrical power input. The full load of the electrical heater was applied for about 6 h. Because the cryogenic system components were colder before applying the electrical heat load, the thermal capacitance of the system may be providing some refrigeration and may be responsible for the lower calorimetric measurement result.

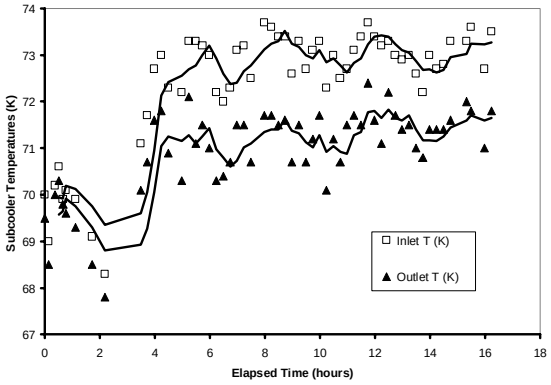


**Fig. 2.22. Sample of the measured temperature data from cryogenic system acceptance test.**

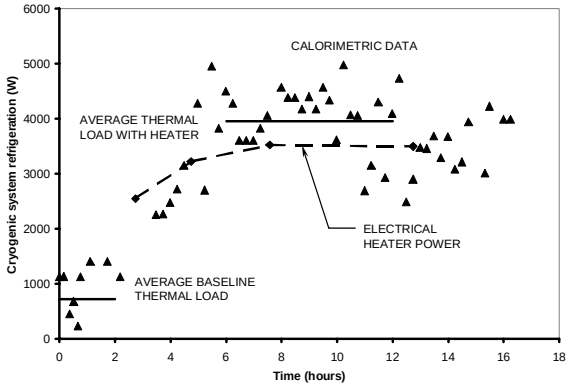


**Fig. 2.23. Refrigeration and applied heat load on the cryogenic system during the acceptance tests.**

**Table 2.1. Results of acceptance test**

| Measurement | Value |
|---|---|
| Average flow rate, L/s | 1.34 |
| Average electrical load, W | 3510 |
| Background thermal load, W | 722 |
| Thermal load with electrical heater, W | 3950 |
| Calorimetrically determined heater load, W | 3228 |

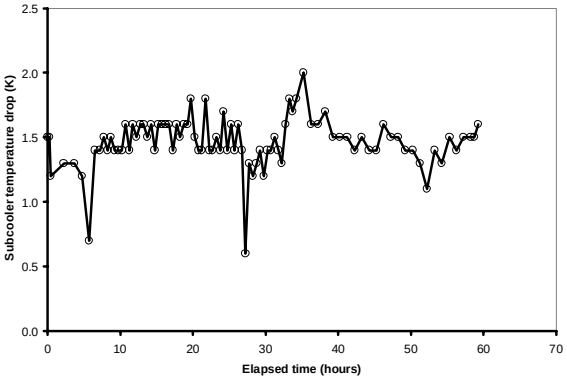


**Fig. 2.24. Subcooler temperature drop for calorimetric heat load of HTS cable phases 1, 2, and 3.**

**Table 2.2. Summary of the temperature rise heat load measurement data**

| Parameter | Value |
|---|---|
| Average subcooler temperature drop, K | 1.4 |
| Flow, L/min | 77 |
| Heat load, W | 3324 |

### 2.1.4.3 System Heat Loads with HTS Cables

After the acceptance tests of the cryogenic system were completed, the final cryogenic connections to the HTS power transmission cables were made. The heat loads with all three HTS power transmission cables connected could then be made. Figure 2.24 shows the subcooler temperatures for a 60-h period. During this time, all three HTS cable phases were being cooled by liquid nitrogen, and the system flow rate was constant.

The HTS cables were not energized at this time. Because the temperature rise is across the subcooler, the heat load includes the three HTS cables, the cryogenic system cold box, the pump work, and the heat load of all interconnecting piping. The system temperatures remained stable during this period. A summary of the average temperature rise, flow rate, and the heat load from this measurement is provided in Table 2.2.

### 2.1.4.4 Heat Loads from Boil-Off Measurements

A second series of heat load measurements were made using a boil-off approach. This second series was conducted at a time when one phase of the HTS power transmission cables was isolated from the cryogenic system. The boil-off measurement was conducted by closing the subcooler fill valve with the subcooler level high (the subcooler was full). The level was then recorded at 10-min intervals along with the subcooler pressure. The level can be related to the volume in the subcooler, and the heat load of the system is calculated based on Eq. (2.4),

$$Q = \rho h_{fg} \frac{\Delta V}{\Delta t} \quad , \tag{2.4}$$

where ρ is the density of the liquid nitrogen, $h_{fg}$ is the latent heat of vaporization at a given pressure, and $\Delta V$ is the change in liquid volume over a time interval $\Delta t$. The values for density and latent heat of vaporization were evaluated as an average for each pressure of each time interval. The subcooler pressure and the volume of liquid boiled off during the two boil-off runs are shown in Figs. 2.25 and 2.26. In the first run, the liquid level initially rose in the subcooler, giving a negative boil-off volume, because a fill valve had not completely closed at the start of the run due to a time delay in the response of the PID loop that controls the valve's operation. After 20 min, the level began to fall, as expected. The heat loads for the last three times were averaged and are shown in Table 2.3.

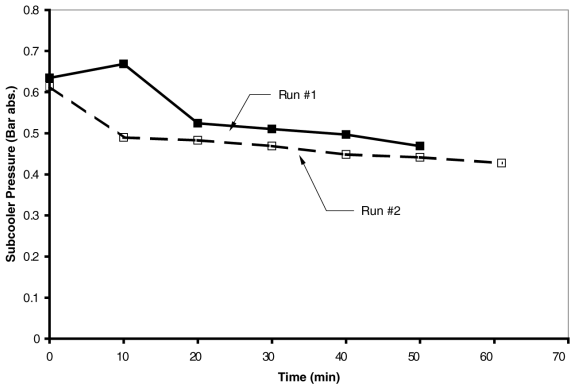


**Fig. 2.25. Subcooler pressures during boil-off heat load measurements.**

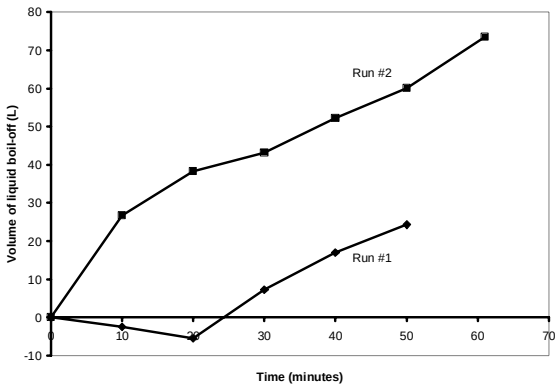


**Fig. 2.26. Volume of liquid boiled off for volumetric heat load measurement.**

**Table 2.3. Summary of the boil-off heat load results**

| | Thermal load (W) |
|---|---|
| Run 1 | 2837 |
| Run 2 | 2625 |
| Average | 2731 |

For the second run, the boil-off volume continuously increased over the run. At first, the process exhibits a transient, but the slope of the volume line remains fairly constant after 10 min into the run. The averages of the last five points are reported in Table 2.3 for this run. The two runs are within 212 W of each other, and they show reasonable agreement for the two heat load measurements. For both of these cases, only two phases of the HTS cable (phases 1 and 2) were cooled with liquid nitrogen. The heat load for the third phase of the HTS cable can be roughly estimated from the two previous sets of measurements by subtracting the measurements for phases 1 and 2 from the measurements for all three phases. This calculation results in a thermal load for the third phase of 593 W.

### 2.1.4.5 Recent Operating Data

After more than a year of operation, the system is performing well and is currently running in the designed automated mode without a system operator. A sample of operating data for 1 month is provided in Fig. 2.27. The HTS cable cryogenic system was continuously running during this period, and the HTS power transmission cables were supplying all of the power to run three Southwire Company manufacturing facilities. The temperature drop across the subcooler and the variation in the currents are presented at 1-h sample intervals in Fig. 2.27. The deviations in the subcooler temperature drop over this time period are small. Therefore, deviations in the cooling load are also relatively small although the current carried by the HTS cables varies by a factor of 2. The average heat load for this time period was 2510 W.

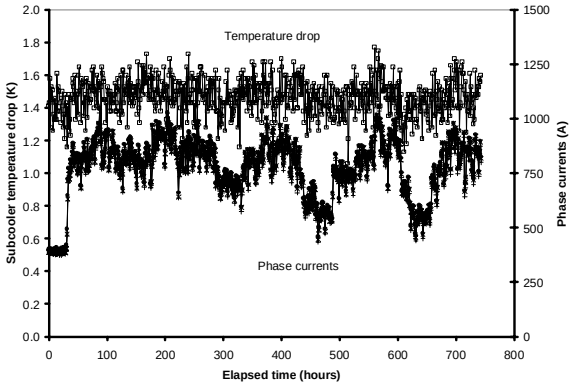


**Fig. 2.27. Subcooler heat exchanger temperature drops of cryogenic system and phase currents of HTS cable system.**

### 2.1.4.6 Summary

The cryogenic system for the Southwire Company HTS cable demonstration project was built by PHPK Technologies, Inc., and it was demonstrated to have met the design goals during acceptance testing. It has provided continuous, stable performance during the entire time that the HTS cables have been operating. After more than a year of operation, the system is performing well and is currently running in the designed automated mode without a system operator.

The background heat load was measured to be 722 W. The heat load measured with the cables just after completing the acceptance tests was 3324 W. During operation with the three 30-m HTS power transmission cables carrying the full load of Southwire Company's three manufacturing plants, there was practically no variation in the cryogenic system load. During this period the heat loads were measured at 2510 W. The system is currently running in the designed automated mode without a system operator.

## 2.1.5 References

1. J. P. Stovall et al., "Operating Experience with the Southwire 30-Meter High-Temperature Superconducting Power Cable," paper C-12A-01 presented at the Cryogenic Engineering Conference and the International Cryogenic Materials Conference, Madison, Wisconsin, July 16–20, 2001.

2. J. W. Lue et al., "Electrical Tests of a Triaxial HTS Cable Prototype," paper C-12A-03 presented at the Cryogenic Engineering Conference and the International Cryogenic Materials Conference, Madison, Wisconsin, July 16–20, 2001.

3. J. A. Demko et al., "Performance Tests of an HTS Power Transmission Cable Splice," Paper C-12A-02 presented at the Cryogenic Engineering Conference and the International Cryogenic Materials Conference, Madison, Wisconsin, July 16–20, 2001.

4. J. A. Demko et al., "Acceptance Test and Operation of the Southwire Co. 30-Meter HTS Cable Cryogenic System," paper C-15C-07 presented at the Cryogenic Engineering Conference and the International Cryogenic Materials Conference, Madison, Wisconsin, July 16–20, 2001.

5. U. K. Sinha et al., "Development and Test of World's First Industrial High Temperature Superconducting (HTS) Power Cable," paper presented at the IEEE Power Engineering Society Winter Meeting 2001, Columbus, Ohio, January 28– February 1, 2001.

6. J. P. Stovall et al., "Installation and Operation of the Southwire 30-Meter High-Temperature Superconducting Power Cable," *IEEE Trans. Applied Superconductivity* **11**, 2467–2472 (2001).

7. M. J. Gouge et al., "Development and Testing of HTS Cables and Terminations at ORNL," *IEEE Trans. Applied Superconductivity* **11**, 2351–2354 (2001).

8. J. A. Demko et al., "Practical AC Loss and Thermal Considerations of HTS Power Transmission Cable Systems," *IEEE Trans. Applied Superconductivity* **11**, 1789–1792 (2001).

9. J. W. Lue et al., "Fault Current Tests of a 5-m HTS Cable," *IEEE Trans. Applied Superconductivity* **11**, 1785–1788 (2001).

10. J. W. Lue et al., "5-m Single-Phase HTS Transmission Cable Tests," *Adv. Cryo. Engr*. **45** (2000).

11. J. A. Demko et al., "Cryogenic System for a High Temperature Superconducting Power Transmission Cable," *Adv. Cryo. Engr*. **45** (2000).

12. J. W. Lue et al., "AC Losses of HTS Tapes and Bundles with De-Coupling Barriers," *IEEE Trans. Applied Superconductivity* **9**, 793–796 (1999).

13. J. W. Lue et al., "AC Losses of Prototype HTS Transmission Cables," *IEEE Trans. Applied Superconductivity* **9**, 416–419 (June 1999).

14. M. J. Gouge et al., "HTS Cable Test Facility: Design and Initial Results," *IEEE Trans. Applied Superconductivity* **9**(2), 134–137 (1999).

15. J. A. Demko et al., "Testing of the Dependence of the Number of Layers on the Performance of a One-Meter HTS Transmission Cable Section," *IEEE Trans. Applied Superconductivity* **9**(2), 126–129 (1999).

16. U. K. Sinha et al., "Design and Construction of LN2-Cooled Prototype Superconducting Transmission Cable," *IEEE Trans. Applied Superconductivity* **7**, 351–354 (1997).

17. J. W. Lue et al., "Test of Two Prototype High-Temperature Superconducting Transmission Cables," *IEEE Trans. Applied Superconductivity* **7**, 302–305 (1997).

18. SINDA Thermal Desktop Users Manual, version 3.3.8, Cullimore and Ring Technologies, Littleton, Colo., 2001.

19. G. Vellego and P. Metra, "An Analysis of the Transport Losses Measured on HTSC Single-Phase Conductor Prototype," *Supercond. Sci. Tech.* **8**, 476–483 (1995).

20. GASPAK, version 2.2, Cryodata, Niwot, Colo., 1989.

## 2.2 SUPERCONDUCTING TRANSFORMER PROJECT

*S. W. Schwenterly, J. A. Demko, I. Sauers, D. R. James, and A. Ellis*

As part of a U.S. Department of Energy (DOE) Superconductivity Partnership Initiative (SPI), ORNL is working on a project to develop HTS utility power transformers. The SPI team is led by Waukesha Electric Systems (WES), with team partners IGC-SuperPower (IGC), Rochester Gas and Electric Company, and ORNL.

Major project activities in the fiscal year 2001 included ac loss testing of model HTS coils, design and procurement of a cryogenic cooling module for the 5/10-MVA HTS transformer and development of dielectric materials for HTS transformers. During the fiscal year, conceptual and detailed engineering design as well as detailed analysis were completed for the cryogenic cooling module for the 5/10-MVA HTS transformer, working closely with WES and IGC. Procurement of equipment was initiated, major components were received from outside vendors, and proof tests were carried out for several components in the cryogenic cooling module. Contracts were awarded to local shops for the final assembly including provision of a dummy load to test the module. High-voltage dielectric tests were conducted including parallel-electrode breakdown tests on composite epoxy samples, breakdown tests on high-voltage sensors and components, and measurements of permittivity and partial discharge on solid materials.

### 2.2.1 AC Loss Testing

Calorimetric ac loss tests continued on sample coils received from IGC. The sample coils were suspended in a vacuum and thermally coupled to a Cryomech GB-37 cryocooler by their current leads and by large copper sheet straps clamped to the G-10 coil structure. Individual turn temperatures were monitored by Allen-Bradley carbon resistors, and a calibrated Scientific Instruments RuO resistor was used to measure the temperature at the winding center. Heating rates observed on the carbon resistors during 10-s ac current pulses were converted to ac loss power by comparing them to the heating rates measured with known heat inputs from a heater tape in the winding. A Behlman 100-A, 45- to 500-Hz ac power supply was connected to the system to add variable-frequency testing capability. Variable-frequency tests, ranging from 45 to 120 Hz, were completed at 24 K on the third IGC sample coil. A fourth coil was received and tested during the quarter. This coil used the actual conductor selected by IGC for the 5/10-MVA prototype transformer and also incorporated fault-handling features. Losses in this coil were measured at 24 K and 36 K with variable current and 60-Hz constant frequency, and with 45- to 240-Hz variable frequency at several different constant current settings.

### 2.2.2 5/10-MVA Transformer Cooling Module

ORNL is responsible for analysis, design, and procurement of the innovative cooling system for the 5/10-MVA transformer. The cooling system components were analyzed to determine the proper size for the required cooling capacity. All design analysis and engineering efforts were completed for the 5/10-MVA transformer cooling module. Designs for the thermal radiation shield and MLI insulation blankets were completed, and an assembly procedure for the complete system was developed. Pressure relief devices were specified, assuming a worst-case loss-of-vacuum incident. An unexpectedly difficult problem was the design of a low-heat-leak suspension system for certain heavy components, capable of withstanding 3-*g* impact loads. After extensive stress and heat transfer calculations on several concepts, this problem was solved successfully, and the complete Pro-E™ drawing package was documented. WES will also incorporate this package into their own Pro-E™ model for the complete transformer.

Figures 2.28 and 2.29 show an elevation schematic and a 3-D cutaway view of the 5/10-MVA transformer. The design analysis results were incorporated into detailed design drawings of the cooling system components. These drawings were sent to qualified vendors for bidding purposes. Detailed cost estimates were also generated in-house for comparison with the received bids.

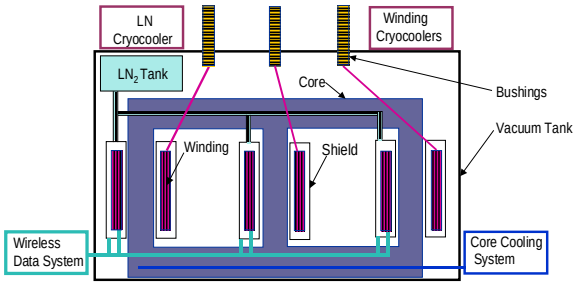


**Fig. 2.28. Schematic of HTS transformer conceptual design.**

Upon receipt of an acceptable bid, the contract to fabricate the components was awarded. The cryocoolers and the top plate that supports the cooling components were received from WES, and several other major components were delivered. Preliminary samples of certain parts were ordered from the vendors and proof-tested to verify that they would perform properly in the transformer application. To further prove the adequacy of the cooling system, we designed a test arrangement that simulates the performance of the transformer cooling system using a realistic dummy load configuration to simulate the transformer coils. A package describing the fabrication and assembly was awarded to a local shop to fabricate the test loop.

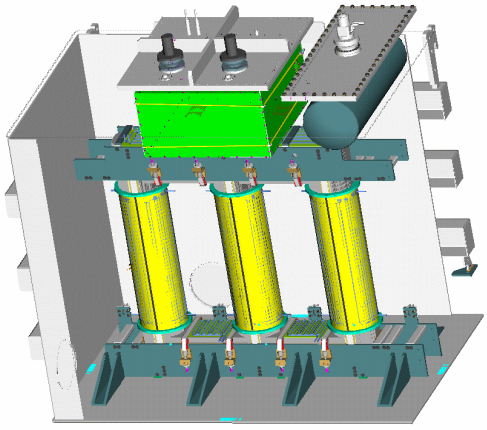

**Fig. 2.29. Cutaway sketch of 5/10-MVA transformer (coils not shown).**

Prior to installation in the 5/10-MVA transformer, the cooling system and dummy load will be tested in the large vacuum test tank at WES. A draft procedure was written for these tests, which will simulate both normal and 2× load transformer operation and will investigate performance with one or both cryocoolers operating. Figure 2.30 is a rendering of the cooling module generated by the Pro-E™ model. The module is designed so that it can be removed from the test tank and plugged directly into the transformer after the dummy load is disconnected.

Shown in Fig. 2.31 is the 5/10-MVA HTS transformer as it will look in the small substation adjacent to the WES manufacturing plant.

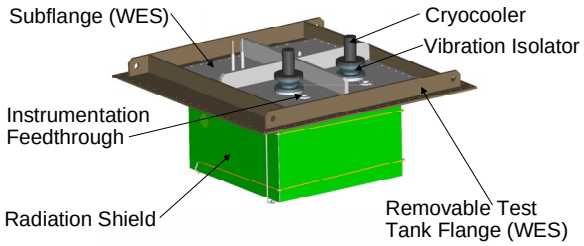


**Fig. 2.30. Pro-E™ rendering of 5/10-MVA cooling module.**

**Fig. 2.31. The 5/10-MVA transformer in planned location at WES factory.**

### 2.2.3 Dielectrics Testing

In support of the development of the HTS transformer, ORNL's High Voltage and Dielectrics Group has provided high-voltage testing in the form of ac, impulse, partial discharge and tan δ measurements for the various dielectric components expected to be used. Various electrode configurations are employed to simulate the electric field strength and direction that the dielectric components will encounter.

AC withstand tests were performed on a sample with cylindrical electrodes embedded in epoxy, at 1.5 times the transformer design operating voltage (1.5×) for 4 h, 1.1× for two days, and 2× for 2 min. The sample also withstood a negative-polarity lightning impulse (1.2 × 50-μs waveform) of 150 kV. Following these tests, an aging test was also performed. A schematic of the aging test is shown in Fig. 2.32. The aging test was conducted at 2.5× for 444 h without failure. This performance compares to a previous test on a similar sample with 2×-field enhancement at the ends of the electrodes that failed after only 4 h. Uniform-field breakdown strength tests were performed on similar dielectric materials with embedded parallel plane electrodes having gaps of 0.5 and 1.0 mm. These tests yielded values of about 54 kV/mm in liquid nitrogen at 1 atm.

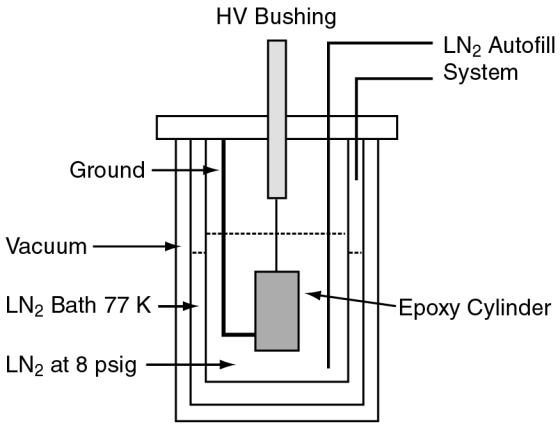


**Fig. 2.32. Liquid nitrogen cryostat used for aging tests.**

Tan δ measurements were made for the same dielectric materials at room temperature and in liquid nitrogen temperatures. Tan δ dropped by approximately an order of magnitude as the temperature was reduced.

### 2.2.4 Impulse Breakdown of Cast Epoxy Cylinder

Additional impulse withstands were performed on the second cast epoxy sample with cylindrical electrodes immersed in liquid nitrogen. Withstands were recorded up to about 300 kV, and the first breakdown was recorded at 304 kV. Figure 2.33 shows the epoxy cylinder prior to mounting in the cryostat.

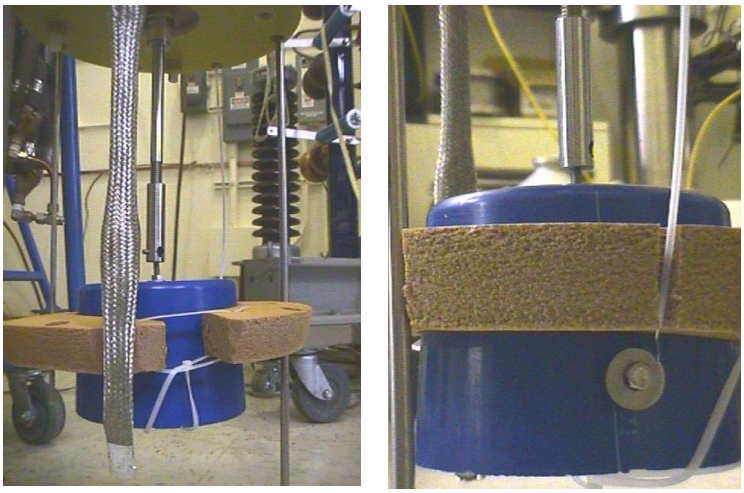

**Fig. 2.33. Epoxy cylinder before mounting in cryostat for impulse tests.**

### 2.2.5 Breakdown Tests of Epoxy Composite Materials

Uniform field breakdown measurements were made on epoxy composites. Of the 12 samples that were made, 6 samples were tested at room temperature and 5 at liquid nitrogen temperatures; one sample was considered unsuitable for testing because of bubbles in the sample. AC breakdown strengths measured at liquid nitrogen temperatures were higher by about 50% than those at room temperature. Contrary to what has been observed for pure materials, this composite material exhibited a lower breakdown field strength (in kV/mm) at the 0.5-mm gap than measured previously at the 1.0-mm gap. One possible explanation is that the filler occupies a greater volume of the gap at the smaller gap lengths than it does at larger gap lengths. Other considerations include the parallelism of the electrodes and the presence of bubbles in the gap. Further study is needed to determine whether there is a trend toward lower breakdown field strengths with smaller gaps.

### 2.2.6 Effect of Sensors on Breakdown Strength

A test sample was prepared consisting of a fiber optic sensor embedded in epoxy plus filler, as shown in Fig. 2.34. The electrode gap was 2.54 cm. AC voltage was applied to the sample immersed in liquid nitrogen and ramped until failure. While the intention was to measure a puncture strength, surface flashover occurred before puncture could be achieved. Three flashovers were observed on three successive voltage applications, yielding a lower limit for the puncture strength of about 100 kV. This is considered acceptable for the transformer application.

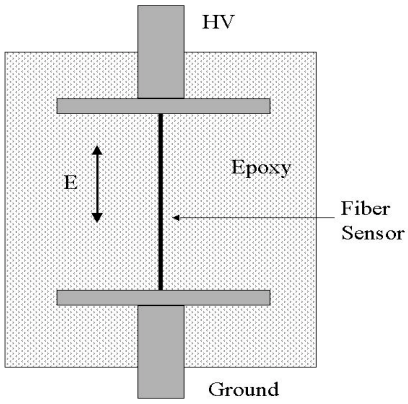


**Fig. 2.34. Test of epoxy-encapsulated fiber optic sensor.**

### 2.2.7 Epoxy Permittivity at Liquid Nitrogen Temperatures

Permittivity measurements were made on an IGC proprietary epoxy at room and liquid nitrogen temperatures since the permittivity at low temperature is not well established. To avoid corona, the room temperature measurements were made with the epoxy sample immersed in an oil bath. The results show a decrease in permittivity from 5.3 at room temperature to 3.0 at 77 K.

### 2.2.8 High-Voltage Tests of Commercial Ceramic Stand-Off

Impulse voltages were applied to a commercial ceramic stand-off to determine the BIL in a vacuum at liquid nitrogen temperatures. For the tests, the part was welded to a standard conflat flange. A high-voltage bushing was placed on the bottom of the vacuum chamber so that the upper part of the stand-off could be at ground potential. Liquid nitrogen was poured into the top of the ceramic stand-off while the stand-off was under vacuum (typically below $10^{-7}$ torr). Because of sharp edges at the ceramic-to-metal joints, the highest impulse withstand was below 50 kV. With the addition of shielding to smooth out the fields, impulse withstands up to 73 kV were achieved, improving the withstand capability by about 50%. The impulses were of the lightning standard type (1.2-μs rise × 50-μs fall) at negative polarity and were applied in steps of 4 to 7 kV. A withstand was deemed to be three applications of the same voltage without breakdown. These are the first BIL tests we are aware of that include both vacuum and liquid nitrogen simultaneously. The ceramic stand-off also passed an ac withstand at 3× operating voltage for 30 min (also at liquid nitrogen temperatures).

### 2.2.9 Partial Discharge in Voids at Liquid Nitrogen Temperatures

An important aging and failure mechanism in epoxy insulation at cryogenic temperatures is believed to be due to partial discharge occurring in a void caused by the presence of a bubble. Very little work has been reported in the literature on the partial discharge patterns produced by this type of defect at low temperatures. We have made epoxy samples with deliberately placed voids to study the difference in partial discharge observed at room and liquid nitrogen temperatures. Initial studies indicated that there are differences and that there is the potential for detecting partial discharge signatures indicating the presence of voids. Partial discharge patterns were observed to change with time of voltage stress. A summer student (Don Burdette, Indiana University of Pennsylvania) worked on this problem during his internship. Dr. Horatio Rodrigo, visiting scientist from Royal Melbourne Institute of Technology, also participated in these studies.

### 2.2.10 New Cryogenic Dielectrics Testing Equipment

A Cryomech AL-330 cryocooler was purchased for tests on large-scale superconducting utility equipment subassemblies. Three new acquisitions have been made that will enhance the diagnostic and measurement capabilities in high-voltage and dielectrics studies: (1) A 200-kV, 15-KVA continuous-duty ac power supply, (2) a high-speed CCD imaging system for flashover and breakdown diagnostics, and (3) a two-stage Cryomech ST-15 cryocooler modified for loss tangent and permittivity measurements.

## 2.3 YBCO QUENCH AND STABILITY STUDIES

*J. W. Lue, M. J. Gouge, R. C. Duckworth, and D. F. Lee*

High-temperature superconductors (HTSs) possess higher stability margins than low temperature superconductors (LTSs). This is mainly due to their higher critical temperatures and thus higher material-specific heats at the higher operating temperatures. Stability margins on the order of 100 J/cm$^3$—2 to 3 orders of magnitude higher than LTSs—were measured on BSCCO-2223 HTSs. Normal zone propagation velocity on the order of only millimeters per second was predicted theoretically. With this first-generation conductor, we observed delayed quenching without a distinctive normal-front propagation of an HTS coil. The development of second-generation YBCO coated conductor promises much higher

critical current density while operating at higher magnetic fields. Before YBCO tape can be used in superconducting magnets and power applications it is essential to ascertain whether the tape has similar stability margins and quench behavior. Studies were conducted in 2001 on ~20-cm-long sections of YBCO tape. The following discussion is based on results presented at the 2001 Cryogenic Engineering Conference held in July 2001 at Madison, Wisconsin.

The RABiTS™ YBCO sample tested is 20 cm long by 1.25 cm wide. It has a nickel substrate of 50 µm, a CeO2-YSZ barrier of 0.2 µm, a YBCO film thickness of 0.3 µm, and a silver coating of 1.5 µm, for a total thickness of about 52 µm. The sample was mounted between Kapton-tape-insulated copper block and a G-10 block with nine bronze strips to monitor the sample in eight zones of 2-cm length. The sample holder was affixed to the first-stage cold head of a Cryomech GB-37 cryocooler for conduction cooling to about 54 K. The critical current density over the YBCO film ranged from 0.64 to 1.7 × 106 A/cm$^2$. Quench testing of the sample was performed with a short overcurrent pulse followed by a longer operating current. Because of the non-uniformity of the $I_c$ of the sample, an initial normal zone created at the weak spot was expected to propagate to other zones of the sample. Overcurrent pulses of up to 72 A for up to 2 s were used to create the initial normal zone. This was followed by an operating current of up to 45 A for pulse lengths up to 30 s to monitor the recovery or quenching of the sample.

### 2.3.1 Stability Margin

With the operating current set near the critical current of the weakest zone, the initial pulse energy was varied by changing the magnitude or the duration of the overcurrent pulse. Full recovery or quenching of the sample was observed with different initial pulses. As indicated in Fig. 2.35, at an operating current of 30 A the sample recovered from an initial pulse of 68 A for 1.75 s but had a propagating quench for a slightly longer 2-s pulse. By integrating the V-I product over the pulse time, one can find the initial heat input to each zone of the sample. In the shots shown in Fig. 2.35, we found that the heat pulse to the weakest zone, zone 5, was about 1 J for the 1.75-s pulse and 1.8 J for the 2-s pulse.

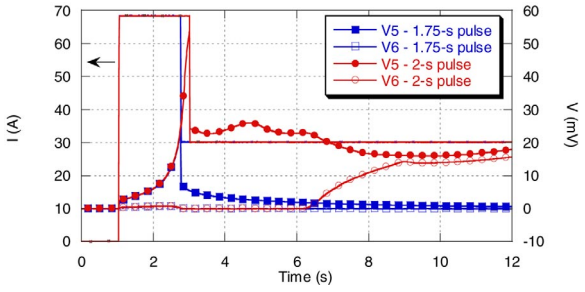


**Fig. 2.35. Full recovery observed at a 68-A overcurrent pulse for 1.75 s and a quench propagation to adjacent zones for a 2-s pulse.**

The voltage, and thus the heat input, increase rapidly after the zone voltage reaches a certain level. Thus, a small increase in overcurrent or pulse duration can add significantly more input energy. The highest initial energy input that still led to full recovery of the sample was about 1 J in the present experiment. This is equivalent to 80 J/cm$^3$ over the whole conductor (including the nickel substrate). This energy would raise the conductor temperature to about 105 K adiabatically. Thus, like BSCCO, the YBCO conductor has a stability margin on the order of 100 J/cm$^3$. It is stable against local heating that does not drive it above its critical temperature of about 80 K.

### 2.3.2 Normal Zone Propagation and Minimum Propagation Current

Distinctive normal zone propagation from the weak spot of zone 5 to adjacent zones was measured at different operating currents. With an initial pulse higher than the stability margin, normal zone propagation was measured at different operating currents. We found a threshold operating current below which no normal zone propagation was observed, even if the initial pulse was increased substantially

above than the stability margin. With an operating current of 15 A, even the weakest zone recovered within 10 s after an overcurrent pulse of 72 A (Fig. 2.36). The initial heat input to zone 5 in this shot was about 240 J/cm$^3$—more than twice the stability margin. This minimum propagation current of about 15 A corresponds to a current density of about 79 kA/cm$^2$ over the Ag coating cross section and about 2.3 kA/cm$^2$ over the cross section of the entire sample. The existence of a minimum propagation current implies that no distinctive normal zone propagation would be observed if the $I_c$ of the sample were lower than this current.

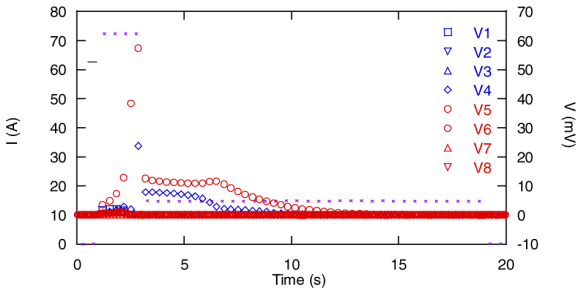


**Fig. 2.36. Full recovery observed when the operating current was set at 15 A or lower.**

### 2.3.3 Propagation Velocity

Figure 2.37 shows two examples of distinctive normal zone propagation of the sample at operating currents of 20.5 A (a) and 30 A [Fig. 2.37(b)]. The initial overcurrent was 72 A for 2 s in Fig. 2.37(a) and 68 A for 2s in Fig. 2.37(b). It can be seen that for the 20.5-A shot, zones 5 and 4 stayed normal after the initial pulse and propagated through zones 6 and 7 on one side and zones 3 and 2 on the other side. For the 30-A shot, which used a smaller initial overcurrent pulse, only zone 5 stayed normal after the pulse but propagated throughout all the zones on either side of this hot spot. Apparently the operating current dominates the dynamics of the normal zone propagation process. It was also noted that away from the hot spot the propagation velocity is insensitive to the initial heat pulse.

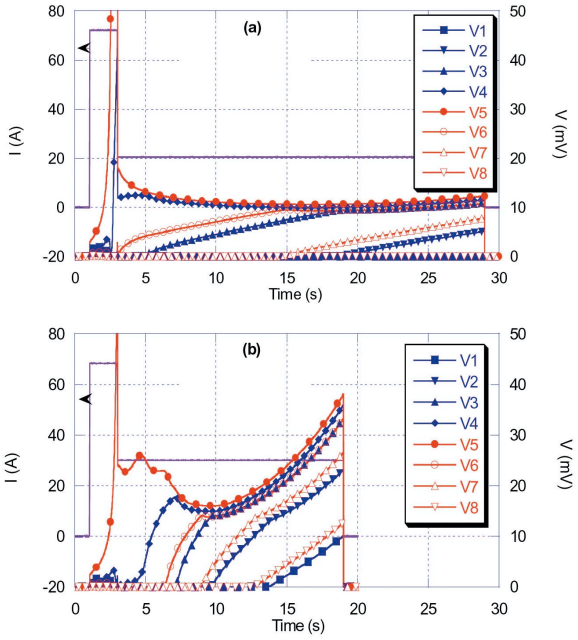


**Fig. 2.37. Normal zone propagation at operating currents of 20.5 A (a) and 30 A (b).**

The propagation velocity, $v$, from one zone to the next was calculated by dividing the zone length of 20 mm by the time of flight of the normal front through that zone—the time between the start of rapid voltage rise of that zone and the next zone. Propagation velocities of 1.4 to 8.3 mm/s were measured for currents of up to 30 A. The results are shown in Fig. 2.38. The velocities through the interior zones—$v$6, $v$4, and $v$3—follow one line, while those through the outer zones, $v$2 and $v$7, follow another line.

### 2.3.4 Comparison with the Adiabatic Theory

The YBCO sample rested on Kapton-tape-insulated copper block and was pressed by the bronze voltage strips from the top. The cooling condition approximates conduction cooling through the end lead connections only. The normal zone propagation velocity can be compared with that calculated by

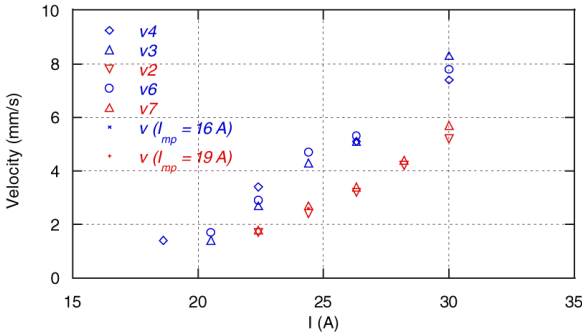


**Fig. 2.38. Measured normal zone propagation velocities as a function of current and adiabatic theory calculations.**

adiabatic theory. Since a minimum propagation current, $I_{mp}$, existed in the experiment, the following equation for the propagation velocity is proposed:

$$v = \frac{\left(I - I_{mp}\right)}{A \cdot C_p} \cdot \left( \frac{k\rho}{\left(T_c - T_0\right)} \right)^{1/2} \tag{2.5}$$

where $A$ is the cross-sectional area, $C_p$ is the specific heat, $k$ is the thermal conductivity, ρ is the resistivity, $T_c$ is the critical temperature (80 K), and $T_o$ is the initial temperature of the sample.

In the present experiment, the initial overcurrent pulse produced large heating in the weak zone and small but non-zero heating in other parts of the sample. An average $T_o$ of 65 K was chosen for the calculation. At this temperature the weighted values of the sample material properties were estimated to be $C_p = 1.0 \times 10^6$ J/m$^3$-K, $k = 370$ W/m-K, and $\rho = 3.5 \times 10^{-9}$ Ω-m. With an $I_{mp}$ of 16 A, very good agreement was found between the data of the interior zones and the modified adiabatic theory as shown in Fig. 2.38. A slightly higher $I_{mp}$ of 19 A also generates excellent agreement with the data of the outer zones. It is conceivable that the end conduction affected the outer zones and raised its minimum propagation current.

### 2.3.5 Finite Element Modeling

The experimental results presented above were modeled by a commercial finite element (FE) code, FlexPDE, developed for the solution of partial differential equations (PDEs). It uses a Galerkin FE model with quadratic or cubic basis functions involving nodal values of the system variables.

The following time-dependent, nonlinear, one-dimensional PDE was solved:

$$C_p(T) \cdot \frac{dT}{dt} = \frac{d}{dx} \cdot k(T) \cdot \frac{dT}{dx} + \rho(T) \cdot J^2 \tag{2.6}$$

In this equation, the thermal conductivity, $k$, volumetric specific heat, $C_p$, and resistivity, ρ, are functions of the local temperature. A weighted average over the YBCO silver coating and nickel substrate were used for the thermal conductivity and specific heat. Additionally, a section of the tape has an enhanced resistivity of about 12–13 cm (in zone 5 closer to zone 4) to simulate the lower critical current in this section. All the stability and quench phenomena-such as stability margin, minimum propagation current, normal zone propagation, and thermal runaway-can be predicted qualitatively by such FE modeling. Two sample calculations are shown here.

The 20-cm-long YBCO tape was initially at ~50 K before the current pulse. The applied current waveform was 72 A for 2 s, followed by an operating current of 15 A for 16 s corresponding to the shot shown in Fig. 2.36. Figure 2.39(a) shows the resulting voltage evolution at 1-cm intervals in response to this current waveform. It shows a full recovery, in good qualitative agreement with the data shown in Fig. 2.36.

Figure 2.39(b) shows the calculated voltage evolution for conditions of Fig. 2.37(a): a current waveform of 72 A for 2 s, followed by an operating current of 20.5 A for 16 s. Normal zone propagation is evident. It is again in good qualitative agreement with the data. In general, when normal zone propagation was observed in the experiment, the code also predicted normal zone propagation under the same test conditions.

Additional testing is planned in the future as longer and more uniform YBCO tapes become available with variable silver coating thickness and in background magnetic fields of up to 6 T.

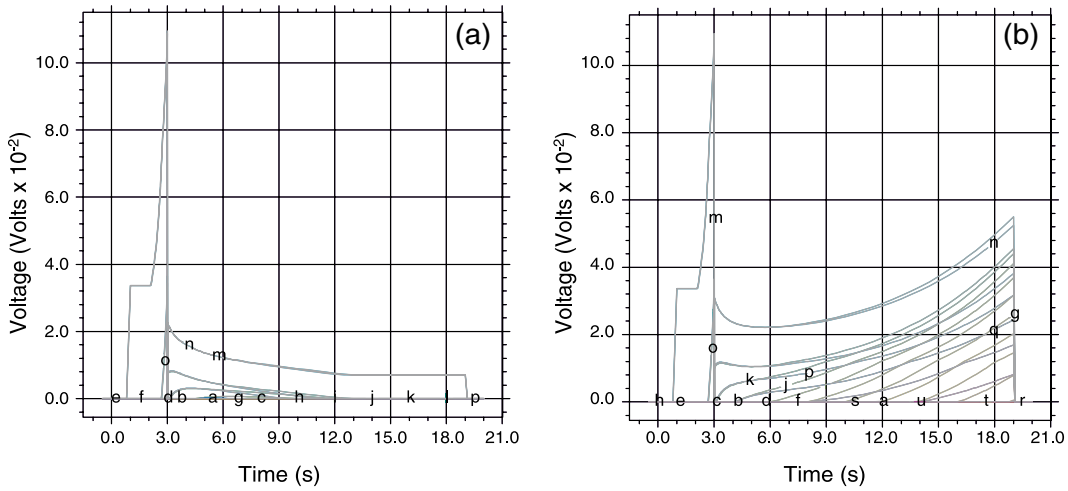


**Fig. 2.39. (a) Full recovery when operating current was set at 15 A (see Fig. 2.36) or lower. (b) Normal zone propagation at an operating current of 20.5 A [see Fig. 2.37 (a)].** The labels on the curves refer to locations 1 cm apart on the 20-cm tape; thus “a” refers to one end of the tape, and “u” refers to the other end.

# 3. Summary of Technology Partnership Activities

## 3.1 BACKGROUND

Oak Ridge National Laboratory (ORNL) is a key participant in the U.S. Department of Energy's (DOE's) national effort on electric power applications of high temperature superconductivity (HTS). ORNL has formed effective teams that combine the resources of the Laboratory with the entrepreneurial drive of private companies. New technology partnership mechanisms, a feature of the ORNL Superconducting Technology Program for Electric Power Systems since its inception in 1988, have resulted in 42 superconductivity "pilot center" cooperative agreements and 8 cooperative R&D agreements (CRADAs). Seven cooperative agreements and three interagency agreements were active during FY 2001. In addition, licensing agreements, joint inventions, and joint publications with the private industry partners have ensured that there *is* technology transfer throughout the program.

Technology partnering on Laboratory-industry teams can occur in several ways. In the ORNL program, the cooperative development level of technology partnering is emphasized: joint Laboratory-industry teams work on problems that (1) requires combined resources and expertise and (2) have a clear objective of precompetitive research and technology development. For the project to succeed, each partner depends on the success of the other. Most of the cooperative projects with private industry and the Laboratory precompetitive research and development (R&D) projects involve developing key technology in which commercialization of the results is expected to occur after a minimum of 3 to 5 years.

## 3.2 RELATIONSHIP TO THE DOE MISSION

The ORNL program mission is that of its program sponsor, DOE's Office of Power Technologies, Superconductivity Program: to develop the technology base necessary for industry to proceed to commercialization of electric energy applications of HTS. HTS will enable new energy-efficient motors, transformers, and transmission lines and will also provide electric power equipment manufacturers with strategic technology for global competitiveness. Electric utilities can defer acquisition of new transmission rights-of-way with successful introduction of superconducting cables. System stability and protection will be enhanced with the introduction of fault-current limiters. Distributed utility systems in the future, which will include distributed generation systems, will benefit from the small size and weight of the next generation of electric power equipment. In addition, oil-free power transformers and cables will provide a cost-effective, more environmentally friendly option for the utility sector.

## 3.3 FUNDING

DOE funding for the ORNL program, a summary of funds-out cooperative agreements and subcontracting activities in 2001, are shown in Tables 3.1, 3.2, and 3.3.

A significant increase in ORNL internal funding in FY 2001 is attributed to the Accelerated Coated Conductor Initiative (ACCI). For this, ORNL (1) purchased $1.4 million in new capital equipment, (2) renovated 2,200 $ft^2$ of laboratories in Building 4508, and (3) hired two new permanent staff members and three postdoctoral fellows to help with the additional research in coated-conductor R&D. Funds-out to industry, universities, and other federal agencies (the National Institute of Standards and Technology and the National Science Foundation) increased in FY 2001 to more than $5.6 million.

**Table 3.1. Superconducting Technology Program funding: authorization and outlay by fiscal year**

| | New budget authorization/outlay ($ × 1000) | | | | |
|---|---|---|---|---|---|
| | 1997 | 1998 | 1999 | 2000 | 2001 |
| Direct scientific and technical[a] | 3,046 | 5,356 | 5,416 | 5,616 | 8,989 |
| Management and outreach | 310 | 400 | 400 | 400 | 400 |
| **Subtotal—ORNL** | **3,356** | **5,756** | **5,816** | **6,016** | **9,389** |
| Subcontracts[b] | 1,021 | 2,437 | 3,244 | 4,099 | 4,680 |
| Funds-out cooperative agreements[c] | 789 | 589 | 795 | 585 | 945 |
| Total program | 5,166 | 8,782 | 9,855 | 10,700 | 15,014 |

[a]Includes ORNL capital equipment ($1.4 M in FY 2001 for ACCI facility).
[b]Details are provided in separate table.
[c]Includes interagency agreements (National Institute of Standards and Technology, National Aeronautics and Space Administration, and the National Science Foundation).

## 3.4 TECHNOLOGY PARTNERSHIP APPROACH

Our interdisciplinary approach uses many of the resources available at ORNL to meet the program goals for joint Laboratory-industry development of HTS technology for electric power applications. Our superconductivity agreement mechanism interlinks R&D projects with industry and universities that optimize utilization of facilities, expertise, and program resources for the benefit of all participants. This program also coordinates the ORNL activities with the other national laboratories, government agencies, university centers, and industry groups.

Cooperative agreements ensure that technology development is industry-driven. The Office of Technology Transfer and Economic Development and patent counsel work together to place these agreements. Where appropriate, these efforts are coordinated with projects within ORNL that are funded by the DOE Office of Science, as well as Work for Others and ORNL Laboratory Director's R&D Fund projects.

Effective funds-out to industry is used to supplement industry cost share. In FY 2001, $5.625 million in funds-out to industry and universities was provided through cooperative agreements and subcontracts. To keep industry involved from the start of the program and to ensure commercialization potential, all of these technology-partnering mechanisms are augmented by CRADAs, user agreements, and licensing activities.

Responsiveness to American industry has high priority in this program. An ORNL ad hoc technical review committee, consisting of a project manager, a scientific coordinator, a manager for conductor development, and a manager for applications development, reviews all inquiries from industry and recommends projects for possible funding. This review ensures that (1) the proposed work fits the program mission, (2) the work is collaborative, (3) there is legitimate commercial interest, and (4) the work is feasible. Substantial private-sector cost share is required on cooperative agreements.

ORNL provides support to the DOE Headquarters (DOE-HQ) Superconductivity Program for Electric Power Systems by identifying, guiding, and monitoring R&D at ORNL and ORNL subcontractor sites and by performing coordination, analysis, and planning of activities related to the national program.

Some of the various activities performed as part of this task include the following:

- technical, project, and budget guidance;
- project identification and development;

**Table 3.2. Superconductivity Program Summary of cooperative agreements as of September 30, 2001**

| Participant | Approved term | Type[a] | Total agreement cost share ($K) | | | Technology area |
|---|---|---|---|---|---|---|
| | | | By DOE | | By industry | |
| | | | To ORNL | To industry | | |
| American Superconductor | 4/5/01–4/4/05 | C | 2,400 | 0 | 2,400 | HTS conductors for electric power applications; BSCCO-2223 Wire Development Group; and YBCO wires |
| MicroCoating Technologies | 9/15/97–3/31/02 | FI | 150 | 0 | 1,100 | Develop coated-conductor technology |
| NIST—Gaithersburg | 12/1/00–11/30/01 | IAG | 0 | 150 | 150 | BSCCO and TBCCO phase diagram support |
| NIST—Boulder | 3/98–2/28/02 | IAG | 0 | 757 | 757 | Electromechanical properties for superconductor applications |
| NSF Science & Tech. Policy Institute (RAND) | 4/15/00–4/30/02 | IAG | 0 | 300 | 0 | HTS critical issues study |
| Neocera | 8/1/01–7/31/02 | FO | 70 | 80 | 80 | Pulsed e-beam deposition as a viable method for HTS coated-conductor development |
| Oxford Instruments | 1/94–1/31/02 | C | 1,050 | 0 | 1,275 | Develop technology for dip-coated BSCCO-2212 wire and RABiTS™ |
| Southwire Company | 2/1/97–9/30/05 | FO | 12,066 | 500 | 12,631 | Develop HTS cable technology |
| 3M-Southwire-LANL-ORNL | 4/3/97–12/31/01 | C | | | | Development of HTS wire using coated conductor technologies |
| 3M | | | | | 2,458 | |
| Southwire | | | | | 480 | |
| LANL | | | | 1,680[b] | 2,938 | |
| ORNL | | | 1,800 | | | |
| Waukesha Electric Systems | 6/15/97–9/30/02 | FO | 2,925 | 250 | 2,284.4 | HTS transformer |
| **Total Active Agreements** | | | 20,461 | 2,037 | 23,615.4 | |
| **Total Completed Agreements** | | | 14,374 | 6,030.6 | 17,798.7 | |
| **TOTALS** | | | 34,835 | 8,067.6 | 41,414.1 | |

[a]NFE = No-Funds-Exchange; FO = Funds-Out; FI = Funds-In; IAG = Interagency Agreement; and C = CRADA.

[b]DOE to LANL.

**Table 3.3. FY 2000–2001 active subcontracts ($K)**

| Subcontractor | Term | Obligated amount | Subject |
|---|---|---|---|
| Imtech | 10/3/94–2/29/00 | 358 | Assist research on HTS materials |
| | 3/1/00–2/28/01 | 66 | |
| | 3/2/01–2/28/02 | 81 | |
| Massachusetts Institute of Technology (competed) | 6/1/00–5/31/02 | 190 | Stability and quench protection |
| Florida State University (competed) | 6/1/00–5/31/02 | 125 | Stability and quench protection |
| Oak Ridge Inst. for Sci. and Edu. (competed) | Ongoing | 880 | Postdoctoral research fellowships |
| Energetics, Inc. (competed) | 4/18/00–3/31/01 | 432 | Technical and analytical support to ORNL |
| | 4/1/01–3/31/02 | 460 | |
| Bob Lawrence & Associates (completed) | 3/15/99–1/14/02 | 685 | Technological and economic benefits assessment and market study; HTS outreach |
| University of South Carolina | 7/1/99–9/30/02 | 20 | High-temperature conductor development and characterization |
| Stanford University (competed) | 10/1/98–3/31/02 | 1465 | Ion-beam-assisted deposition of buffer layers and in situ deposition of YBCO by electron beam evaporation |
| University of Wisconsin (competed) | 10/1/98–12/31/01 | 1596 | BSCCO critical currents and microstructure, YBCO coated conductor microstructure, and pulse tube cryocooler |
| University of Houston (competed) | 10/1/98–9/30/01 | 407 | Research into high-rate photon-assisted MOCVD for YBCO onto buffered, textured metallic substrates |
| Marshall O. Pace | 12/00–12/01 | 15 | High-voltage breakdown studies on cryogenic insulation |
| Boston College | 6/28/99–2/18/01 | 99 | Development of epitaxial film growth and properties |
| | 2/19/01–2/18/02 | 50 | |
| MicroCoating Technologies (competed) | 11/1/99–6/01/02 | 1675 | Coated conductor research |
| 3M (competed) | 2/1/00–9/30/02 | 1877 | Coated conductor research |
| IGC (competed) | 6/7/00–3/9/02 | 950 | Coated conductor research |
| Hobe Corp. | 3/3/00–9/30/01 | 142 | Analysis of cryogenic R&D |
| SAIC | 7/15–12/31/00 | 45 | Prep. of cryogenics implementation plan |
| | 3/26–9/30/01 | 40 | Analysis of market penetration model |
| University of Florida | 10/1/00–9/30/02 | 111 | HTS films and buffers on biaxially textured copper |
| University of Kansas | 5/00–7/15/02 | 98 | Hg-based HTS coated conductors |
| University of Cincinnati | 9/15/01–9/16/02 | 28 | Nonfluorine sol-gel synthesis of YBCO thin films on flexible substrates for developing coated conductors |

- exploratory R&D;
- support of consultants and subcontracts providing technical, program, or technology partnering support;
- identification, placement, and technical monitoring of subcontractors, review committee members, and workshop guests;
- guidance and support on technology partnering;
- publication of reports and proceedings from workshops;
- identification and initiation of cooperative agreements, interagency agreements (i.e., National Institute of Standards and Technology), and memoranda of understanding;
- distribution of reports to program managers;
- preparation of assessments to address technical, economic, regulatory, and institutional issues in the DOE program;
- coordination of interlaboratory technical team meetings;
- assistance to the DOE-HQ program manager in preparation of the Superconducting Technology Program Annual Operating Plan;
- collection and dissemination of programmatic information and program-wide assessments;
- assistance in organizing the HTS Wire Development Workshop [in partnership with Argonne National Laboratory (ANL) and Los Alamos National laboratory (LANL)]; and
- review of industrial collaboration opportunities through multilaboratory meetings and conference calls.

ORNL works with the other program laboratories to address such issues as communication among program participants, workshop and meeting implementation, planned competitive solicitations and superconductivity agreements, and coordination of technical and economic assessments.

An Industrial Overview Committee is charged with reviewing program activities and advising Laboratory management as to program progress, policy, and direction. The committee consists of representatives of electric utilities, original equipment manufacturers, and HTS wire manufacturers. This committee meets occasionally at ORNL, ANL, or LANL.

## 3.5 PROGRAM INVENTIONS AND PATENT LICENSE AGREEMENTS

A summary of the new invention disclosures for FY 2001 is shown in Table 3.4. All patent license agreements since 1988, and issued patents in FY 2001, are shown in Tables 3.5 and 3.6, respectively.

**Table 3.4. Invention disclosures in FY 2001**

| ID No. | Subject | Submitted by |
|---|---|---|
| 963 | A textured, single-cyrstal-like buffered substrate and devices thereof | A. Goyal |
| 964 | A textured, single-cyrstal-like buffered substrate and devices thereof | A. Goyal |
| 1001 | Method and depositing crystalline, epitaxial coatings of oxides on substrates | A. Goyal |
| 1002 | Method to fabricate biaxially textured articles | A. Goyal |

**Table 3.5. Superconducting Technology Program patent license agreements**

| 1640-X (RABiTS™) |
|---|
| Oxford Superconducting Technology |
| CCVD, Inc., dba MicroCoating Technologies |
| 3M |
| American Superconductor Corporation |

**Table 3.6. Patents (cumulative listing)**

| Patent No./ID No. | Date Issued | Title |
|---|---|---|
| 5,357,756 (1185-X) | Oct. 25, 1994 | Bipolar Pulse Field for Magnetic Refrigeration |
| 5,395,821 (1039-X) | March 7, 1995 | Method of Producing Pb-Stabilized Superconductor Precursors and Superconductor Articles Therefrom |
| 5,525,583 (1471-X) | June 11, 1996 | Superconducting Magnetic Coil (issued to American Superconductor) |
| 5,532,532 | July 2, 1996 | Hermetically Sealed Superconducting Magnet Motor |
| 5,739,086 (1640-X) | April 14, 1998 | Structures Having Enhanced Biaxial Texture and Method of Fabricating Same |
| 5,741,377 (1640-X) | April 21, 1998 | Structures Having Enhanced Biaxial Texture and Method of Fabricating Same |
| 5,830,828 (1193-X) | November 3, 1998 | Process for Fabricating Continuous Lengths of Superconductor |
| 5,846,912 (1512-X) | December 8, 1998 | Method for Preparation of Textured $YBa_2Cu_3O_x$ Superconductor |
| 5,898,020 (1640-X) | April 27, 1999 | Structures having Enhanced Biaxial Texture and Method of Fabricating Same |
| 5,958,599 (1640-X) | September 28, 1999 | Structures Having Enhanced Biaxial Texture |
| 5,964,966 | October 12, 1999 | Method of Forming Biaxially Textured Alloy Substrates and Devices Thereon |
| 5,968,877 (18-19) | October 19, 1999 | High Tc YBCO Superconductor Deposited on Biaxially Textured Ni Substrate |
| 5,972,847 (458) | October 26, 1999 | Method for Making High-Critical-Current-Density $YBa_2Cu_3O_7$ Superconducting Layers on Metallic Substrates |
| 6,055,446 (1193) | April 25, 2000 | Continuous Lengths of Oxide Superconductors |
| 6,077,344 (223) | June 20, 2000 | Sol-Gel Deposition of Buffer Layers on Biaxially Textured Metal Substances |
| 6,106,615 (368) | August 22, 2000 | Method of Forming Biaxially Textured Alloy Substrates and Devices Thereon |
| 6,114,287 (1784, new 148) | September 5, 2000 | Method of Deforming a Biaxially Textured Buffer Layer on a Textured Metallic Substrate and Articles Therefrom |

**Table 3.6 continued**

| Patent No./ID No. | Date Issued | Title |
|---|---|---|
| 6,150,034 (467) | Nov. 21, 2000 | Buffer Layers on Rolled Nickel, or Copper as Superconductor Substrates |
| 6,156,376 (467) | Dec. 5, 2000 | Buffer Layers on Metal Surfaces having Biaxial Texture as Superconductor Substrates |
| 6,159,610 (467) | December 12, 2000 | Buffer Layers on Metal Surfaces having Biaxial Texture as Superconductor Substrates |
| 6,180,570 B1 (312) | January 30, 2001 | Biaxially Textured Articles Formed by Plastic Deformation |
| 6,256,521 B1 (1784, new 148) | July 3, 2001 | Preferentially Oriented, High Temperature Superconductors by Seeding and a Method for Their Preparation |
| 6,261,704 B1 (218) | July 17, 2001 | MgO Buffer Layers on Rolled Nickel or Copper as Superconductor Substrates |
| 6,70,908 B1 (734) | August 7, 2001 | Rare Earth Zirconium Oxide Buffer Layers on Metal Substrates |
| 6,286,194 B1 (1193) | September 11, 2001 | Apparatus for Fabricating Continuous Lengths of Superconductor |
| 6,296,701 B1 (296) | October 2, 2001 | Method of Depositing An Electrically Conductive Oxide Film on a Textured Metallic Substrate and Articles Formed Therefrom |

# 4. Events, Honors, and Awards

## 4.1 DOE LABORATORY TECHNOLOGY RESEARCH PROGRAM

The DOE Laboratory Technology Research (LTR) program has funded a multiyear ORNL cooperative research and development agreement (CRADA) with American Superconductor Corporation (ASC). The project, entitled "Low-Cost, High-Performance YBCO Conductors," was awarded funding of $750,000 over a 3-year period (FY 2002–2004). As part of this CRADA, ASC will provide additional funding of $625,000. The project's principal investigators are M. Parans Paranthaman and A. Goyal of ORNL and M. W. Rupich of ASC. The objective of the project is to develop materials science and technology necessary for YBCO-coated conductors on biaxially textured, nonmagnetic, high-strength substrates.

## 4.2 SUMMER 2001 STUDENT INTERNS

Six undergraduate student interns worked with mentors in ORNL's Superconductivity Program during the summer of 2001 (see Table 4.1). They performed research related to development of high-temperature superconducting (HTS) wire as well as cryogenic materials and power systems (see Fig. 4.1).

**Table 4.1. Summer interns and their ORNL sponsors**

| Interns | | ORNL staff | |
|---|---|---|---|
| Name | College/University | ORNL Division | Mentor |
| Don Burdette | Indiana University of Pennsylvania | Life Sciences | I. Sauers |
| Michael Shanks | Indiana University of Pennsylvania | Chemical and Analytical Sciences | M. Paranthaman |
| Frank Partica | Juniata College (Penn.) | Metals and Ceramics | P. Martin |
| Jennifer Tobin | Albion College (Mich.) | Solid State | R. Kerchner |
| Marcus Young | University of Tennessee | Fusion Energy | M. Gouge |
| Tom Thersleff | University of Wisconsin—Madison | Chemical and Analytical Sciences | M. Paranthaman |

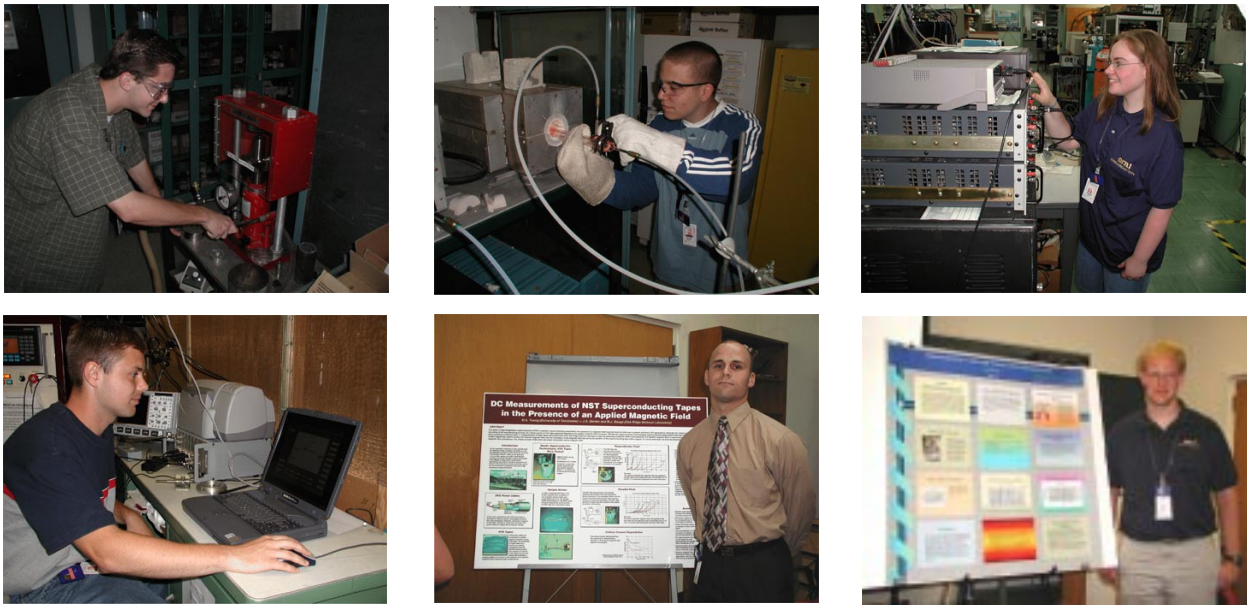


**Fig. 4.1. Superconductivity Program interns, summer 2001. Top row, left to right: Tom Thersleff, Michael Shanks, and Jennifer Tobin; bottom row, left to right: Don Burdette, Marcus Young, and Frank Partica.**

## 4.3 NEW ACCI SUPERCONDUCTOR RESEARCH LABORATORY DEDICATED

ORNL's new HTS research laboratory was dedicated on April 19, 2001 (see Fig. 4.2). The new laboratory is part of the Accelerated Coated Conductor Initiative (ACCI), a collaborative effort between ORNL and Los Alamos National Laboratory. The initiative will help accelerate the development of power cables, motors, generators and transformers using new "second-generation" wire technology through joint efforts among DOE laboratories, universities, and industry.

Among ORNL's CRADA partners participating in the dedication were American Superconductor Corporation, MicroCoating Technologies (see Fig. 4.3), Oxford Superconducting Technology, and the Southwire Company.

Charles Cook of the U.S. House of Representatives Science Committee staff as well as Marshall Reed, Debbie Haught, and Roger Meyer of the DOE's Office of Power Technologies, participated in the dedication ceremony (see Fig. 4.4). Speaking at the dedication were ORNL director Bill Madia, LANL Superconducting Technology Center director Dean Peterson, Southwire program manager R. L. Hughey, and DOE-HQ Superconductivity program manager Marshall Reed.

A briefing for ORNL's RABiTS™ technology partners was also held on April 19.

**Fig. 4.2. Marshall Reed (DOE-HQ) and Bill Madia (Director, ORNL) cut the ribbon to ORNL's new HTS research laboratory.**

**Fig. 4.3. Representatives from ORNL's CRADA partners at the HTS laboratory dedication. Left photo, from left to right: Amit Goyal (ORNL), Martin Rupich (American Superconductor), and Parans Paranthaman (ORNL); right photo, left to right: Ken Marken (Oxford Superconducting Technology) and Shara Shoup (MicroCoating Technologies).**

**Fig. 4.4. From left to right, Charles Cook (staff member of the U.S. House of Representatives Science Committee) and Debbie Haught and Roger Meyer (both of DOE's Office of Power Technologies) examined equipment during the dedication of the new HTS laboratory.**

## 4.4 RABiTS™ WINS A FEDERAL LABORATORY CONSORTIUM EXCELLENCE IN TECHNOLOGY TRANSFER AWARD

The ORNL RABiTS™ team received a 2001 Federal Laboratory Consortium (FLC) award for Excellence in Technology Transfer for its work on second-generation HTS wires. Second-generation HTS wires may be less expensive than BSCCO because they are made of nickel or nickel alloys rather than silver alloys, and they exhibit unprecedented electrical performance in strong magnetic fields. Five U.S. companies teamed with ORNL to transfer the technology: Oxford Superconducting Technology, MicroCoating Technologies, EURUS Technologies, 3M Company; and ASC. According to the FLC award citation, "The collaboration among ORNL and its commercial partners led to the creation of a significant number of jobs, privately sponsored research tied to commercial licensing, and the accelerated development of the next generation of HTS wire."

The FLC Awards in Technology Transfer, established in 1984, recognize individuals within federal laboratories who have done outstanding work in transferring technology. Award criteria include demonstration of "uncommon creativity and initiative" in the transfer of technology; and significant benefits to industry, state and local government, and/or the general public.

## 4.5 RABiTS™ RECEIVES AN ENERGY 100 AWARD

In the past year, ORNL's RABiTS™ technology was selected receive one of DOE's Energy 100 Awards (see Fig. 4.5). These awards honor what a panel of judges regarded as the 100 best scientific and technological accomplishments of the Department of Energy during the period 1977–2000. The emphasis was on developments that save consumers money and improve quality of life.


**Fig. 4.5. RABiTS™ won an Energy 100 award in 2000.**

The award nomination noted that the RABiTS™ technology enables the fabrication of long lengths of flexible, single-crystal-like, high-temperature ceramic superconducting wires with very high current-carrying capabilities. As the manager of DOE's Superconductivity Program said, "We now have a new path to the goal we've pursued since the 1986 Nobel Prize-winning discovery [of high-temperature superconductors]—a superconducting wire that can be used in motors, generators, and other energy systems while operating at liquid-nitrogen temperatures."

## 4.6 WIRE DEVELOPMENT GROUP EARNS COLLABORATION SUCCESS AWARD

The Wire Development Group, in which ORNL's Superconducting Materials Group participates, has earned a Collaboration Success Award from the Council for Chemical Research. The Wire Development Group, a 9-year-old collaboration, also includes research teams from ASC, Argonne and Los Alamos National Laboratories, and the University of Wisconsin. ORNL's Superconducting Materials Group was part of the effort focusing attention on the effect of deformation processing on the density and texture of a precursor powder prior to heat treatment. ORNL scientists Don Kroeger, Dominic Lee, and Bob Williams

concentrated on development of novel mechanical deformation procedures, analysis and interpretation of the wire's microstructures and exploration of alternative fabrication concepts of a bismuth compound. The council determined that the research played a key role in ASC's establishment of a leadership position in reliable HTS wire manufacturing. ASC recently decided to scale up production of this technology to yield millions of meters of bismuth compound superconducting wire per year by 2002, according to the award release. The composite wire produced by ASC is being used in numerous first-generation HTS electric power systems, including transmission lines, motors, transformers, and fault current limiters.

## 4.7 OUTREACH TO MIDDLE SCHOOLS AT ENVIRONMENTAL SYMPOSIUM FOR EIGHTH-GRADE STUDENTS

On March 13 and 14, 2001, several members or the ORNL Superconductivity Program participated in the Roane State Community College "Real Science for the Real World: An Environmental Symposium for Eighth-Grade Students." (See Fig. 4.6.) The event, sponsored by DOE and Roane State, provides students the opportunity to learn more about the environment and applications of science and technology in the real world. Each day the symposium was divided into concurrent skill sessions that combine lecture, demonstration, and hands-on activities for the students.

**Fig. 4.6. Parans Paranthaman (left) assists students with accessing the Superconductivity Web site. David K. Christen (right) demonstrates the Meissner effect to a group of students.**

## 4.8 SOUTHWIRE TEAM CELEBRATES SUCCESS

A year after activating its HTS power delivery system, Southwire Company celebrated the anniversary and the system's recent milestone of operating for 5000 h at a 100% load. Activated on January 5, 2000, Southwire's power delivery system provides full power to three manufacturing plants at the company's Carrollton, Georgia, headquarters. Nearly immune to resistance, Southwire's HTS cables lose only ~0.5% of power during transmission, compared to 5–8% lost by traditional cables. The cables also deliver about three to five times more power density than traditional underground cables. Attending the celebration in Carrollton with Southwire's team were ORNL's Bob Hawsey, Stan Milora, John Stovall, and Mike Gouge. By the end of 2001, the cable system exceeded 11,000 h of operation, including unattended operation beginning June 2001.

# 5. Presentations/Publications

## PUBLISHED


Annavarapu, S., L. Fritzemeier, Q. Li, A. Malozemoff, V. Prunier, M. W. Rupich, C. Thieme, W. Zhang, M. Gopal, J. Seleznev, M. J. Cima, M. Paranthaman, A. Goyal, and D. F. Lee, "Progress Toward a Low-Cost Coated Conductor Technology," *Physica C* **341–48,** 2319–22 (2000).

Aytug, T., B. W. Kang, C. Cantoni, E. Specht, M. Paranthaman, A. Goyal, D. K. Christen, D. T. Verebelyi, J. Z. Wu, R. E. Ericson, C. J. Thomas, C. Y. Yang, and S. E. Babcock, "Growth and Characterization of Conductive $SrRuO_3$ and $LaNiO_3$ Multilayers on Textured Ni tapes for High-$J_c$ $YBa_2Cu_3O_{7-\delta}$ Coated Conductors," *J. Mater. Res.* **16**(9), 2661–69 (2001).

Aytug, T., M. Paranthaman, B. W. Kang, S. Sathyamurthy, A. Goyal, and D. K. Christen, "$La_{0.7}Sr_{0.3}MnO_3$: A Single, Conductive-Oxide Buffer Layer for the Development of $YBa_2Cu_3O_{7-\delta}$ Coated Conductors," *Appl. Phys. Lett*. **79**(14), 2205–7 (2001).

Aytug, T., J. Z. Wu, B. W. Kang, D. T. Verebelyi, C. Cantoni, E. D. Specht, A. Goyal, M. Paranthaman, and D. K. Christen, "An All-Sputtered Buffer Layer Architecture for High-$J_c$ $YBa_2Cu_3O_{7-\delta}$ Coated Conductors," *Physica C* **340,** 33–40 (2000).

Callcott, T. A., L. Lin, G. T. Woods, G. P. Zhang, J. R. Thompson, M. Paranthaman, and D. L. Ederer, "Soft X-Ray Spectroscopy Measurements of the p-like Density of States of B in $MgB_2$ and Evidence for Surface Boron Oxides on Exposed Surfaces," *Phys. Rev. B* **64**, 132504 (2001).

Cantoni, C., T. Aytug, D. T. Verebelyi, M. Paranthaman, E. D. Specht, D. P. Norton, and D. K. Christen, "Conductive Buffer Layers and Overlayers for the Electrical Stability of Coated Conductors," *IEEE Trans. Appl. Supercond.* **11**, 3309–12 (2001).

Christen, H. M., H. Y. Zhai, C. Cantoni, M. Paranthaman, B. C. Sales, C. Rouleau, D. P. Norton, D. K. Christen, and D. H. Lowndes, "Superconducting Magnesium Diboride Films with $T_c$ Approximately = 24 K Grown by Pulsed Laser Deposition with In Situ Anneal," *Physica C* **353**, 157–61 (2001).

Cox, Craig, and Bob Hawsey, "The Potential of Superconductivity," *Energy Magazine,* Winter 2000.

Cui, X., F. A. List, D. M. Kroeger, D. F. Lee, M. Paranthaman, A. Goyal, B. W. Kang, E. D. Specht, P. M. Martin, and W. B. Robbins, "Continuous Deposition of Ex Situ YBCO Precursor Films on Rolling-Assisted Biaxially Textured Substrates by Electron Beam Evaporation," *Physica C* **351,** 175–81 (2001).

Demko, J. A., J. W. Lue, M. J. Gouge, J. P. Stovall, Z. Butterworth, U. K. Sinha, R. L. Hughey, "Practical AC Loss and Thermal Considerations for HTS Power Transmission Cable Systems," *IEEE Trans. Appl. Supercond.* **11,** 1789 (2001).

Feldmann, D. M., J. L Reeves, A. A. Polyanskii, A. Goyal, R. Feenstra, D. F. Lee, M. Paranthaman, D. M.. Kroeger, D. K. Christen, S. E. Babcock, and D. C. Larbalestier, "Magneto-Optical Imaging of Transport Currents in $YBa_2Cu_3O_{7-x}$ on RABiTS™," *IEEE Trans. Appl. Supercond.* **11**, 3772–75 (2001).

Feldmann, D. M., J. L. Reeves, A. A. Polyanski, G. Kozlowski, R. R. Biggers, R. M. Nekkanti, I. Maartense, M. Tomsic, P. Barnes, C. E. Oberly, T. L. Peterson, S. E. Babcock, and D. C. Larbalestier, "Influence of Nickel Substrate Grain Structure on $YBa_2Cu_3O_{7-x}$ Supercurrent Connectivity in Deformation-textured Coated Conductors," *Appl. Phys. Lett.* **77**(18), 30 October 2000.

Gouge, M. J., J. A. Demko, P. W. Fisher, C. A. Foster, J. W. Lue, J. P. Stovall, U. K. Sinha, J. Armstrong, R. L. Hughey, D. Lindsay, J. C. Tolbert, "Development and Testing of HTS Cables and Terminations at ORNL," *IEEE Trans. Appl. Supercond*. **11**, 2351 (2001).

Goyal, A., D. F. Lee, F. A. List, E. D. Specht, R. Feenstra, M. Paranthaman, X. Cui, S. W. Lu, P. M. Martin, D. M. Kroeger, D. K. Christen, B. W. Kang, D. P. Norton, C. Park, D. T. Verebelyi, J. R. Thompson, R. K. Williams, T. Aytug, and C. Cantoni, "Recent Progress in the Fabrication of High-$J_c$ Tapes by Epitaxial Deposition of YBCO on RABiTS™," *Physica C* **357–60**, 903–13 (Part 2) (2001).

Holzapfel, B., D. Verebelyi, C. Cantoni, M. Paranthaman, B. Sales, R. Feenstra, D. K. Christen, and D. P. Norton, "Low-Angle Grain Boundary Transport Properties of Undoped and Doped Y123 Thin Film Bicrystals," *Physica C* **341–48,** 1431–34 (2000).

Kunchur, M. N., B. I. Ivlev, D. K. Christen, and J. M. Phillips, "Vortex Instability and the Normal State at Low Temperatures," *Physica C* **341–48,** 1003–6 (2000).

Li, Q., W. Zhang, U. Schoop, M. W. Rupich, S. Annavarapu, D. T. Verebelyi, C. L. H. Thieme, X. Cui, M. D. Teplitsky, L. G. Fritzemeier, G. N. Riley, M. Paranthaman, A. Goyal, D. F. Lee, and T. G. Holesinger, "Progress in Solution-Based YBCO Coated Conductors," *Physica C* **357–60,** 987–90 (2001).

Lu, S. W., F. A. List, D. F. Lee, X. Cui, M. Paranthaman, B. W. Kang, D. M. Kroeger, A. Goyal, P. M. Martin, and R. E. Ericson, "Electron Beam Co-evaporation of Y-$BaF_2$-Cu Precursor Films for $YBa_2Cu_3O_{7-y}$ Coated Conductors," *Supercond. Sci. Technol.* **14,** 218–23 (2001).

Lue, J. W., G. C. Barber, J. A. Demko, M. J. Gouge, J. P. Stovall, R. L. Hughey, and U. K. Sinha, "Fault Current Tests of a 5-m HTS Cable," *IEEE Trans. Appl. Supercond*. **11,** 1785 (2001).

Paranthaman, M., C. Cantoni, H. Y. Zhai, H. M. Christen, T. Aytug, S. Sathyamurthy, E. D. Specht, J. R. Thompson, D. H. Lowndes, H. R. Kerchner, and D. K. Christen, "Superconducting $MgB_2$ Films via Precursor Postprocessing Approach," *Appl. Phys. Lett.* **78**(23), 3669–71 (2001).

Paranthaman, M. P., T. G. Chirayil, F. A. List, X. Cui, A. Goyal, D. F. Lee, E. D. Specht, P. M. Martin, R. K. Williams, D. M. Kroeger, J. S. Morrell, D. B. Beach, R. Feenstra, and D. K. Christen, "Fabrication of Long Lengths of Epitaxial Buffer Layers on Biaxially Textured Nickel Substrates Using a Continuous Reel-to-Reel Dip-Coating Unit," *J. Am. Ceram. Soc.* **84**(2), 273–78 (2001).

Paranthaman, M., T. G. Chirayil, S. Sathyamurthy, D. B. Beach, A. Goyal, F. A. List, D. F. Lee, X. Cui, S. W. Lu, B. Kang, E. D. Specht, P. M. Martin, D. M. Kroeger, R. Feenstra, C. Cantoni, and D. K. Christen, "Fabrication of Long Lengths of YBCO Coated Conductors Using a Continuous Reel-to-Reel Dip-Coating Unit," *IEEE Trans. Appl. Supercond.* **11**, 3146–49 (2001).

Paranthaman, M., C. Park, X. Cui, A. Goyal, D. F. Lee, P. M. Martin, T. G. Chirayil, D. T. Verebelyi, D. P. Norton, D. K. Christen, and D. M. Kroeger, "$YBa_2Cu_3O_{7-y}$ Coated Conductors with High Engineering Current Density," *J. Mater. Res.* **15**(12), 2647 (2000).

Paranthaman, M., J. R. Thompson, and D. K. Christen, "Effect of Carbon-Doping in Bulk Superconducting $MgB_2$ Samples," *Physica C* **355,** 1–5 (2001).

Rikel, M. O., R. K. Williams, X. Y. Cai, A. A. Polyanski, J. Jiang, D. Wesolowsk, E. E. Hellstrom, D. C. Larbalestier, K. DeMoranville, and G. N. Riley, Jr., "Overpressure Processing Bi2223/Ag Tapes," *IEEE Trans. Appl. Supercond*. **11,** 3026 (2001).

Rupich, M. W., Q. Li, S. Annavarapu, C. Thieme, W. Zhang, V. Prunier, M. Paranthaman, A. Goyal, D. F. Lee, E. D. Specht, and F. A. List, "Low-Cost Y-Ba-Cu-O Coated Conductors," *IEEE Trans. Appl. Supercond.* **11**, 2927–30 (2001).

Schwenterly, S. W., J. A. Demko, J. W. Lue, M. S. Walker, C. T. Reis, D. W. Hazelton, X. Shi, and M. T. Gardner, "AC Loss Measurements with a Cryocooled Sample," *IEEE Trans. Appl. Supercond.* **11**, 4027 (2001).

Stovall, J. P., J. A. Demko, P. W. Fisher, M. J. Gouge, J. W. Lue, U. K. Sinha, J. W. Armstrong, R. L. Hughey, D. Lindsay, and J. C. Tolbert, "Installation and Operation of the Southwire 30-m High-Temperature Superconducting Power Cable," *IEEE Trans. Appl. Supercond*. **11**, 2467 (2001).

Thompson, J. R., M. Paranthaman, D. K. Christen, K. D. Sorge, H. J. Kim, and J. G. Ossandon, "High Temporal Stability of Supercurrents in $MgB_2$ Materials," *Supercond. Sci. Technol.* **14,** L16–L19 (2001).

Verebelyi, D. T., C. Cantoni, J. D. Budai, and D. K. Christen, "Critical Current Density of $YBa_2Cu_3O_{7-\delta}$ Low-Angle Grain Boundaries in Self-Field," *Appl. Phys. Lett.* **78**(14), 2031–33 (2001).

Xie, Y. Y., T. Aytug, J. Z. Wu, D. T. Verebelyi, and D. K. Christen, "Growth and Physical Properties of Hg-1212 HTSC Tapes on Buffered Metal Substrates," *Physica C* **341–48**, 2505–6 (2000).

Xie, Y. Y., T. Aytug, J. Z. Wu, D. T. Verebelyi, M. Paranthaman, A. Goyal, and D. K. Christen, "Epitaxy of $HgBa_2CaCu_2O_6$ Superconducting Films on Biaxially Textured Ni Substrates," *Appl. Phys. Lett.* **77**(25), 4193–95 (2000).

Zhai, H. Y., H. M. Christen, L. Zhang, M. Paranthaman, C. Cantoni, B. C. Sales, P. H. Fleming, D. K. Christen, and D. H. Lowndes, "Growth Mechanism of Superconducting $MgB_2$ Films Prepared by Various Methods," *J. Mater. Res.* **16**(10), 2759–62 (2001).

Zhai, H. Y., H. M. Christen, L. Zhang, C. Cantoni, M. Paranthaman, B. C. Sales, D. K. Christen, and D. H. Lowndes, "Superconducting Magnesium Diboride Films on Si with $T_{c0}$ ~24 K Grown via Vacuum Annealing from Stoichiometric Precursors," *Appl. Phys. Lett.* **79**(16), 2603–5 (2001).

Zhai, H. Y., H. M. Christen, L. Zhang, M. Paranthaman, P. H. Fleming, and D. H. Lowndes, "Degradation of Superconducting Properties in $Mgb_2$ Films by Exposure to Water," *Supercond. Sci. Technol.* **14,** 425–28 (2001).

## SUBMITTED FOR PUBLICATION

Aytug, T.. Y. Y. Xie, J. Z. Wu, and D. K. Christen, "Growth Characteristics of $HgBa_2CaCu_2O_6$ Superconducting Films on $CeO_2$-Buffered YSZ Single Crystals: An Assessment for Coated Conductors," submitted to *Physica C*.

Cantoni, C., D. K. Christen, R. Feenstra, A. Goyal, G. W. Ownby, D. M. Zehner, and D. P. Norton, "Reflection High-Energy Electron Diffraction Studies of Epitaxial Oxide Seed-layer Growth on Rolling-assisted Biaxially Textured Substrate Ni(001): The Role of Surface Structure and Chemistry," submitted to *Appl. Phys. Lett.*

Kang, B. W., A. Goyal, D. F. Lee, J. E. Mathis, E. D. Specht, P. M. Martin, and D. M. Kroeger, "Comparative Study of Thickness Dependence of Critical Current Density of $YBa_2Cu_3O_{7-\delta}$ on (100) $SrTiO_3$ and on Rolling-Assisted Biaxially Textured Substrates," submitted to *J. Mater. Res.*

Paranthaman, M., D. K. Christen, H. M. Christen, J. R. Thompson, C. Cantoni, H. Y. Zhai, and R. Jin, "Superconducting $MgB_2$ Films with Enhanced Critical Current Densities and Irreversibility Fields," chapter in *Studies of High Temperature Superconductors,* vol. 38, ed. Anant Narlikar, Nova Science Publishers, Commack, N.Y., 2001.

## PRESENTATIONS, ABSTRACTS, AND PAPERS SUBMITTED FOR PUBLICATION IN CONFERENCE AND WORKSHOP PROCEEDINGS

Demko, J. A., "Thermal Management of High-Temperature Superconducting Power Cables," paper submitted to the proceedings of the Space Technology Applications International Forum, Albuquerque, N.M., February 2002.

Hawsey, R. A., "Overview of U.S. Department of Energy Superconductivity Program for Electric Power," abstract submitted to 2001 Fall MRS Meeting, Dec. 2–6, Boston.

Hawsey, R. A., and D. E. Peterson, "National Accelerated Coated Conductor Initiative," paper submitted to the proceedings of the Space Technology Applications International Forum, Albuquerque, N.M., February 2002.

Kim, H. J., J. R. Thompson, D. T. Verebelyi, C. Cantoni, J. D. Budai, and D. K. Christen, "Critical Current Density of $YBa_2Cu_3O_{7-\delta}$ Low-Angle Grain Boundaries," abstract submitted to American Physical Society Meeting, Seattle, Wash., March 12–16, 2001.

Paranthaman, M., T. Aytug, B. W. Kang, S. Sathyamurthy, P. M. Martin, A. Goyal, D. M. Kroeger, R. Feenstra, and D. K. Christen, "Development of a High-Rate, Economically Viable Buffer Deposition Process for YBCO-Coated Conductors," abstract submitted to 2001 MRS Fall Meeting, Dec. 2–6, Boston.

Paranthaman, M., D. K. Christen, H. M. Christen, J. R. Thompson, H. R. Kerchner, C. Cantoni, and H. Y. Zhai, "Growth of High-Current-Density $MgB_2$ Films Using Ex Situ Precursor Approach," paper submitted to ISS 2001 Proceedings (to be published in *Physica C*).

Paranthaman, M., T. Aytug, S. Sathyamurthy, D. B. Beach, A. Goyal, D. F. Lee, B. W. Kang, L. Heatherly, E. D. Specht, K. J. Leonard, D. K. Christen, and D. M. Kroeger, "Bulk Solution Techniques to Fabricate High-$J_c$ YBCO-Coated Conductors," paper submitted to ISS 2001 Proceedings (to be published in *Physica C*).

Sauers, I., D. R. James, A. R. Ellis, and M. O. Pace, "High-Voltage Studies of Dielectric Materials for HTS Power Equipment," abstract accepted for publication as a paper in *Dielectrics and Insulation Phenomena at Low Temperatures,* a special issue of *IEEE DEI Transactions on Electrical Insulation*.

Thompson, J. R., A. Goyal, D. K. Christen, D. M. Kroeger, and H. J. Kim, "$Ni_{1-x}Cr_x$ Substrate Alloys with Reduced or Non-Ferromagnetic Properties for Coated Conductor Applications," American Physical Society Meeting, Seattle, Wash., March 12–16, 2001.

## PAPERS SUBMITTED TO CEC/ICMC 2001, MADISON, WISCONSIN, JULY 16–20, TO BE PUBLISHED IN *ADVANCES IN CRYOGENIC ENGINEERING*

Augustynowicz, S. D. (Dynacs Engineering at KSC), J. A. Demko (ORNL), and J. E. Fesmire (NASA-KSC), "Thermal Insulation Performance of Flexible Piping for Use in HTS Power Cables."

Cheggour, N., J. W. Ekin, C. C. Clickner, R. Feenstra, A. Goyal, and M. Paranthaman, "Transverse Stress Effect on the Critical-Current Density of Y-Ba-Cu-O coated RABIiTS™ Tapes."

Demko, J. A., J. W. Lue, M. J. Gouge, P. W. Fisher, J. P. Stovall, J. Tolbert, D. Lindsay, U. Sinha, and R. L. Hughey, "Performance Tests of an HTS Power Transmission Cable Splice."

Demko, J. A., J. W. Lue, M. J. Gouge, J. P. Stovall, Z. Butterworth, R. L. Hughey, D. Lindsay, M. Roden, and U. Sinha, "Acceptance Test and Operation of the Southwire Company 30-m-high Temperature Superconducting Cable Cryogenic System."

Fesmire, J. E. (NASA-KSC), S. D. Augustynowicz (Dynacs Engineering at KSC), and J. A. Demko (ORNL), "Overall Thermal Performance of Flexible Piping under Simulated Bending Conditions."

Fesmire, J. E. (NASA-KSC), S. D. Augustynowicz (Dynacs Inc.), and J. A. Demko (ORNL), "Thermal Insulation Performance of Flexible Piping for Use in HTS Power Cables."

Lue, J. W., M. J. Gouge, J. A. Demko, G. C. Barber, J. C. Tolbert, U. K. Sinha, D. Lindsay, and R. L. Hughey, "Electrical Tests of a Triaxial HTS Cable Prototype."

Lue, J. W., M. J. Gouge, D. F. Lee, D. M. Kroeger, R. C. Duckworth, and J. M. Pfotenhauer, "Quench Tests of a 20-cm-long RABiTS YBCO Tape."

Stovall, J. P., J. A. Demko, P. W. Fisher, M. J. Gouge, R. A. Hawsey, J. W. Lue, J. W. Armstrong, R. L. Hughey, D. Lindsay, M. Roden, U. Sinha, and J. C. Tolbert, "Operating Experience with the Southwire 30-meter High-Temperature Superconducting Power Cable."

## EXTENDED ABSTRACTS SUBMITTED TO THE 2001 INTERNATIONAL WORKSHOP ON SUPERCONDUCTIVITY, CO-SPONSORED BY ISTEC AND MRS, JUNE 24–27, HONOLULU, HAWAII

Aytug, T., B. W. Kang, D. T. Verebelyi, C. Cantoni, S. Sathyamurthy, A. Goyal, P. M. Martin, M. Paranthaman, and D. K. Christen, "Bilayer Conductive-Oxide Buffer Layer Structures for High-$J_c$ $YBa_2Cu_3O_{y-\delta}$ Coated Conductors."

Cantoni, C., D. K. Christen, D. P. Norton, R. Feenstra, A. Goyal, G. W. Ownby, and D. M. Zehner, "Effects of Surface Chemistry and Structure on Buffer Layer Epitaxy."

Feenstra, R., A. Goyal, M. Paranthaman, D. F. Lee, P. M. Martin, D. K. Christen, and D. M. Kroeger, "High-$J_c$ YBCO Coated Conductors Produced by an Ex Situ $BaF_2$ Process."

Feenstra, R., A. Goyal, M. Paranthaman, D. F. Lee, P. M. Martin, D. K. Christen, and D. M. Kroeger (ORNL); and P. N. Arendt, J. R. Groves, and R. F. DePaula (LANL), "High-$I_c$ YBCO Coated Conductors Produced by an Ex Situ $BaF_2$ process."

Feldmann, D. M., and D. C. Larbalestier (Univ. of Wisconsin—Madison); D. T. Verebelyi, W. Zhang, Q. Li, and G. N. Riley (American Superconductor); and R. Feenstra, A. Goyal, D. F. Lee, M. Paranthaman, D. M. Kroeger, and D. K. Christen (ORNL), "Inter and Intra-Grain Transport Measurements in $YBa_2Cu_3O_{7-x}$ Deformation Textured Coated Conductors."

Gray, K. E., H. Claus, L. Chen, B. W. Veal, A. P. Paulikas, D. J. Miller, and U. Welp (Argonne National Laboratory); and R. Feenstra and D. K. Christen (ORNL), "Role of Grain Boundary Dissipation and a New Measurement Technique."

Hawsey, R. A., "Overview of U.S. Developments in Coated Conductors."

Kang, B. W., A. Goyal, F. A. List, D. K. Christen, R. H. Kerchner, S. Sathyamurthy, D. F. Lee, P. M. Martin, and D. M. Kroeger, "The Effect of Calcium Doping in Low Angle Grain Boundaries of $YBa_2Cu_3O_{7-\delta}$ on Rolling Assisted Biaxially Textured Substrates."

Lee, D. F., F. A. List, D. M. Kroeger, and K. W. Childs (ORNL); and D. O'Neill and W. B. Robbins (3M Company), "Long-Length Conversion of Barium-Fluoride Precursor Films on RABiTS™."

Paranthaman, M., S. Sathyamurthy, T. Aytug, D. B. Beach, A. Goyal, B. W. Kang, R. Feenstra, D. K. Christen, D. F. Lee, P. M. Martin, L. Heatherly, and D. M. Kroeger, "High Current Density YBCO Coated Conductors on Strengthened Biaxially Textured Ni-W Substrates."

Reeves, J. L., D. M. Feldmann, D. C. Larbalestier, and S. E. Babcock (Univ. of Wisconsin—Madison); and R. Feenstra and A. Goyal (ORNL), "Effect of the Substrate Texture on the Microstructure and Alignment of the YBCO and Buffer Layers of RABiTS™-Type Coated Conductors."

Reis, C. T. (IGC), S. P. Mehta (Waukesha Electric Systems), B. W. McConnell (ORNL), and R. H. Jones (Rochester Gas and Electric), "Development of High Temperature Superconducting Power Transformers."

Robbins, W. B. (3M Company), and F. A. List (ORNL), "Reactively Sputtered Buffers on Pre-Textured Nickel."

Sathyamurthy, S., M. Paranthaman, B. W. Kang, D. B. Beach, T. Aytug, R. Feenstra, A. Goyal, and D. M. Kroeger, "Solution Deposition Approaches to Coated Conductor Fabrication on Biaxially Textured Ni-W alloy Substrates."

Thieme, C., E. Thompson, S. Annavarapu, Q. Li, W. Chang, and M. W. Rupich (American Superconductor); and M. Paranthaman, A. Goyal, D. F. Lee, E. D. Specht, and F. A. List (ORNL), "Progress in TFA Solution-Processed YBCO Coated Conductors."